High Rate and Ageing Studies for the Drift Tubes of the Atlas Muon Spectrometer

DISSERTATION
zur
Erlangung des Doktorgrades
der
Fakultät für Mathematik und Physik
der
Albert-Ludwigs-Universität Freiburg im Breisgau

vorgelegt von
Stephanie Zimmermann
März 2004

Dekan:	Prof. Dr. R. Schneider
Referent:	Prof. Dr. G. Herten
Korreferent:	Prof. Dr. A. Bamberger
Tag der mündlichen Prüfung:	18. Mai 2004

High Rate and Ageing Studies for the Drift Tubes of the Atlas Muon Spectrometer

by

Stephanie Zimmermann

March 2004

Universität Freiburg
im Breisgau

Fakultät für Physik
und Mathematik

Abstract

The muon spectrometer of Atlas, one of the 4 experiments currently under construction at the Large Hadron Collider LHC, relies on Monitored Drift Tubes (MDTs) for track reconstruction in most of its regions. The MDTs will have to sustain count rates up to 1500 Hz/cm and must be able to survive an accumulated charge of up to 0.6 C/cm during 10 years of operation. This thesis presents results of high rate and ageing studies conducted at the CERN Gamma Irradiation Facility GIF; a series production Atlas muon chamber and a prototype of the gas recirculation system planned at LHC were used for the first time.

Test beam muons were utilized to evaluate the MDT high rate behaviour; questions of resolution, efficiency and changes in the drift properties of the operating gas were addressed. The measurements were complemented by simulations with the program GARFIELD. For the ageing study the MDTs were irradiated over a period of several months, in which their performance was monitored weekly with cosmic muons. A loss in pulse height was observed for MDTs under gas recirculation after an accumulated charge equivalent to only 1 year of LHC operation, while tubes operated without gas recirculation did not show any evidence of ageing. Extensive material analyses were performed in order to determine the origin of the performance degradation.

Contents

Preface

"Dass ich erkenne, was die Welt im Innersten zusammenhält" ('so that I understand what keeps the world together') – these words, said by the character Dr. Faustus in J. W. Goethe's drama 'Faust', are a good description of the goal of fundamental physics research, namely to describe nature by a small number of universal laws and equations. The question as to what makes up matter in particular attracted the interest of philosophers and scientists from ancient Greece over the middle ages up to the present times.
It is remarkable that already the earliest models assume the existence of fundamental entities from which all matter is built. This idea is present both in the discussions of Aristotle, who postulated all things to be based on the elements water, air, fire and earth, and the work of Demokrit, to whom we owe the expression atom (from Greek *atomos* = indivisible). While we nowadays know that Aristotle's elements are not the basis of chemical compounds, nor are Demokrit's atoms really indivisible, the concept that there exists only a limited number of different basic building blocks is still the foundation of modern theories. This is in particular true for the Standard Model of particle physics, which represents our present understanding of nature's composition on a sub-atomic scale. Many of the experimental results leading to the development of the Standard Model would not have been possible without the use of dedicated accelerators with increasingly high beam energies. A new accelerator facility, the Large Hadron Collider LHC, is currently under construction at the European Organization for Nuclear Research CERN near Geneva, Switzerland. Designed for an unprecedented particle energy of 7 TeV when operating with protons, LHC aims at solving some of the still open questions of particle physics, in particular with respect to the origin of mass. Data will be taken by four different experiments, Atlas, CMS, LHCb and Alice.
The purpose of this thesis was to study the performance of Monitored Drift Tubes (MDTs) for the Atlas muon spectrometer. The Atlas drift tubes are ionization detectors which not only allow for particle detection, but in combination with a strong magnetic field also for a precise momentum determination. The focus of the studies presented here was on testing a final Atlas MDT chamber instead of using small, dedicated setups, as done previously. Measurements were conducted at the CERN Gamma Irradiation Facility GIF, where an intense radioactive source was utilized to simulate background conditions expected at the LHC. Data was acquired both over a short period of 10 days with monoenergetic muons from CERN's SPS accelerator complex and over several months with cosmic muons. The aim of the latter studies was to check for any evidence of a degradation in the chamber performance ('ageing') with accumulated charge or length of exposure to irradiation. Understanding ageing effects and eliminating their origin is of utmost importance at Atlas, since drift tubes can not be exchanged once they are installed on the detector.
This thesis is organized in 7 chapters; chapter 1 gives an overview over the Standard Model of particle physics and the motivation for constructing the LHC. Technical details of the

LHC project, its four experiments and in particular the Atlas detector are also discussed. Chapter 2 reviews the basic operating principles of drift tubes in general and summarizes the main parameters of the Atlas MDTs. The third chapter describes the experimental setup; particular emphasis is put on the prototype gas recirculation system, which was built as part of this thesis and evaluated for the first time. Chapters 4 and 5 are dedicated to the measurements performed with beam muons, and to simulations carried out in order to assess the experimental results.
Chapter 6 presents results pertaining to chamber ageing, distinguishing between tubes operated without gas recirculation and MDTs connected to the recirculation prototype. The two cases are discussed separately since no performance degradation was observed in the first case while a massive pulse height loss was found in the latter. The outcome of extensive material analyses, which confirmed a contaminant as the cause of the ageing phenomena, is also discussed. A summary of the main results is given in chapter 7, followed by several appendices containing more technical aspects of the work presented.

'Nature loves to hide'
Heraklit, 550 - 480 B.C.

Chapter 1

Introduction

This chapter aims at giving a short introduction to the present understanding of particle physics (1.1) and to ongoing experimental efforts. The Large Hadron Collider LHC, currently under construction at the 'Organisation Européenne pour la Recherche Nucléaire' CERN near Geneva, is reviewed (1.2) and the biggest of its detectors, Atlas, is described in more detail (1.3). The last section, 1.4, is dedicated to a discussion of important physics processes and open questions to the solution of which Atlas is expected to contribute.

1.1 The Standard Model of particle physics

According to our present knowledge all matter is formed from a total of 12 different elementary particles which can be grouped into 2×3 families,

$$\begin{pmatrix} e \\ \nu_e \end{pmatrix}, \begin{pmatrix} \mu \\ \nu_\mu \end{pmatrix}, \begin{pmatrix} \tau \\ \nu_\tau \end{pmatrix}$$

and

$$\begin{pmatrix} u \\ d \end{pmatrix}, \begin{pmatrix} c \\ s \end{pmatrix}, \begin{pmatrix} t \\ b \end{pmatrix}.$$

The three **leptons** electron (e), muon (μ) and tau (τ) are negatively charged. For each lepton l there exists a corresponding neutrino, ν_l. Neutrinos are electrically neutral and very light particles. The six **quarks** up (u), down (d), charm (c), strange (s), top (t) and bottom (b) have a charge of either +2/3 or -1/3; their masses increase from the u- to the t-quark. All particles listed are fermions with spin 1/2.
Quarks and leptons can interact with each other by means of four different forces: The **electromagnetic** interaction between charged particles, the **strong** interaction between quarks, the **weak** interaction in which all particles can participate, and finally the **gravitation** which couples to the mass of a particle. Gravitational forces are normally negligible in sub-atomic processes; they are therefore not included in the Standard Model of particle physics. The other three forces are all described by the exchange of mediator or **gauge bosons**, namely the **photon** in the case of the electromagnetic, $\boldsymbol{W}$- and $\boldsymbol{Z}$-bosons for the weak and **gluons** for the strong interaction. Photons and gluons are massless; the W- and Z-bosons have a mass of 80.2 GeV and 91.2 GeV respectively.
In the 1960's the electromagnetic and the weak interaction were combined into a single theory which is known as the GSW model, after its founders Glashow, Salam and Weinberg, or as **electroweak unification**. From a mathematical point of view it is a locally gauge-invariant theory with the symmetry group SU(2)×U(1). The GSW model predicts

the existence of four massless gauge bosons, which is in disagreement with the large Z- and W-boson mass found experimentally. The contradiction can be solved by a mechanism known as **spontaneous symmetry breaking**, if at least one additional massive particle, the **Higgs boson** H, is introduced into the theory.

Experimental confirmation of the Standard Model and open questions

Up to now there exists no evidence suggesting that the Standard Model is wrong. Its predictions have been subjected to a variety of tests whose outcome was in all cases in agreement with the theory. The one particle not detected so far is the Higgs boson; its discovery is therefore one of the foremost goals of experiments currently running or under construction.
A problem with the Standard Model is that it is essentially an empirical theory; it describes experimental results very well, but gives no answers to more theoretical questions like

- Why are there 3 generations of leptons and quarks? All stable matter in the universe consists of electrons, u- and d-quarks only;
- The Standard Model has 21 free parameters that need to be determined experimentally. Is there a deeper reason for their values?
- The hierarchy problem: In the quantum field theoretical formalism of the Standard Model the gauge boson masses depend on the energy scale. Loop corrections make the Higgs particle mass unstable. An extremely precise 'fine-tuning' of the parameters is needed to prevent the Higgs mass from exploding; this is considered as unnatural by many theoreticians.

Suggested extensions to the Standard Model, which would solve some of the open questions, include **Super Symmetry** (SUSY) and the addition of extra dimensions to the usual 4-dimensional space-time.
SUSY models associate a super symmetric partner with each particle in the Standard Model; super partners of fermions are bosons and vice versa. This effectively doubles the particle spectrum. Additional terms have to be included in the loop corrections to the Higgs mass; they are such that they cancel the large divergences in the Standard Model contributions, thus eliminating the hierarchy problem. The simplest of the super symmetric models, the so-called MSSM[1], predicts the existence of a total number of 5 Higgs bosons, three of which are neutral (h, H and A); the remaining two ($H^{\pm}$) are electrically charged.
The introduction of extra dimensions seems especially promising in an attempt to include gravity into a unified theory.

1.2 The Large Hadron Collider LHC

The progress in understanding the constituents of matter and their interactions over the past 30 years would not have been possible without the advances made in accelerator technology. Bringing particles of ever increasing energy into collision with each other, the forces between quarks and leptons could be probed to a deeper and deeper level; simultaneously a large number of short-lived particles was discovered.

[1] Minimal Super Symmetric Model

Experiments performed at an accelerator are usually scattering experiments in which one tries to gain insight into the laws of interaction by analysing the remnants of a particle collision. In this respect the methods applied in modern particle physics are not different from the one used by E. Rutherford and his collaborators in their famous experiment at the beginning of the 20th century; in this case the outcome of course was that the Thompson atomic model, which described atoms as a uniform, positively charged mass with the negative electrons embedded in it like plums in a plum-pudding, was replaced by the Rutherford model postulating a small, heavy nucleus surrounded by an electron cloud. While Rutherford arrived at his results using α-particles of a few MeV, far larger energies are needed to penetrate the structures inside a nucleon or to study interactions with a very short range, as a consequence of Heisenberg's uncertainty relation. High energy accelerators built nowadays to study particle interactions are mostly implemented as so called 'storage rings': In a storage ring particles are kept on a circular orbit by a magnetic field; since they pass the same section of the ring repeatedly, a relatively small electric field parallel to the direction of motion is sufficient for their acceleration to high energies. Typically two beams revolving in opposite directions are used; they are brought to a collision at one or more points of their trajectory. Assuming identical particles of energy E, the center of mass energy in this case is $E_{cm} = 2 \cdot E$, compared to $E_{cm} \sim \sqrt{E}$ for fixed target experiments in which a single beam of energy E impinges on a stationary block of matter.
Particles accelerated in a storage ring can be leptons (electrons, positrons), hadrons (protons, with a somewhat higher effort also anti-protons) or ions. One of the largest accelerators ever designed, the Large Hadron Collider LHC [20], is currently under construction

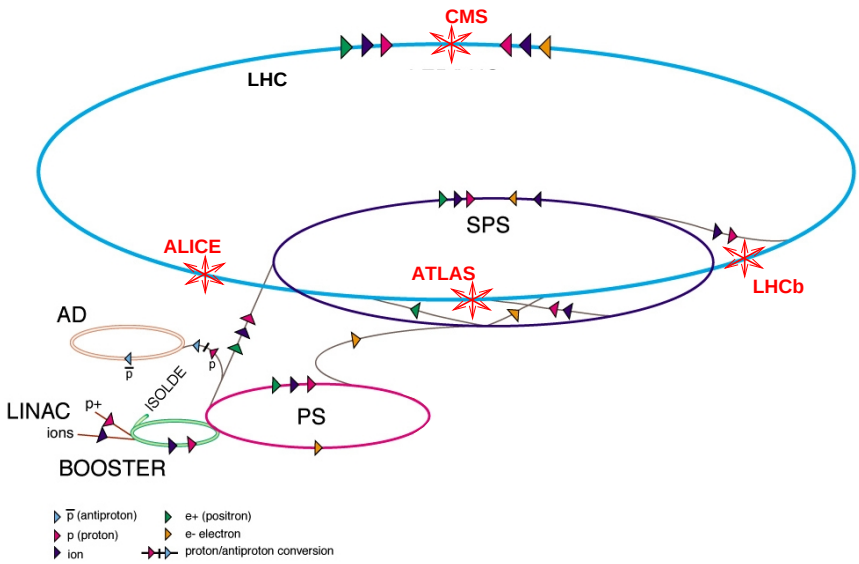

Figure 1.1: CERN accelerator complex [33]. Before being injected into the 27 km circumference LHC storage ring, protons pass a series of pre-acceleration stages. Once they reach their nominal energy, they are brought to collision in four interaction points, each assigned to one of the experiments Atlas, CMS, Alice and LHCb. (Arrows in the schematic denoting electrons and positrons show how the complex was used during the operation of LHC's predecessor, LEP.)

at the European Laboratory for Particle Physics CERN near Geneva. LHC is expected to commence operation in 2007; it is a proton-proton machine designed to reach a center of mass energy of 14 TeV. Colliding protons rather than leptons makes for a more complicated data analysis since in the latter case the interaction takes place between two truly elementary particles while in the former the quarks constituting a proton as well as the forces between them have to be taken into account. The big advantage in accelerating protons is that energy losses due to synchrotron radiation, which are proportional to the fourth power of E/m (E : particle energy, m : particle mass), are far smaller than for electrons.
The layout of the LHC and the various stages used for particle injection and pre-acceleration are shown in figure 1.1. In a first step free protons are produced by ionizing hydrogen atoms; they are accelerated to 50 MeV in a LINAC before being transferred to the booster and the proton synchrotron PS. The booster and the PS bring the energy up to 1.4 GeV and 25 GeV respectively. After leaving the PS the protons are fed into the super proton synchrotron SPS, itself a storage ring with a circumference of approximately 6 km, before being injected into the 27 km long LHC ring with an energy of 450 GeV. During the LHC acceleration cycle the magnetic field necessary to keep the particles on their circular orbit increases from initially 0.535 T to 8.33 T at the nominal beam energy of 7 TeV. More than 1000 separate super-conducting dipoles are used to produce the needed B-field; each dipole has a length of 14.3 m and a cross section as shown in figure 1.2. Each of the two LHC proton beams, moving in opposite directions, has its own beam pipe. The field producing coils draw a current of 11850 A at nominal operation.
The design luminosity of LHC is $10^{34}\,\mathrm{cm}^{-2}\mathrm{s}^{-1}$, with a start up phase at 10% of this value planned for the first two years of running. The protons in each beam are clustered into bunches of 7.7 cm rms length with a spacing of 25 ns between consecutive bunches; at each of the four interaction points bunches therefore collide with a frequency of 40 MHz.
Three experiments at LHC are dedicated to studying proton-proton collisions. Two of them, Atlas and CMS, are designed to cover a wide range of physics processes, from searches for Higgs or SUSY particles to the precision determination of the top quark properties; a third experiment, LHCb, is specifically aimed at investigating B-mesons.

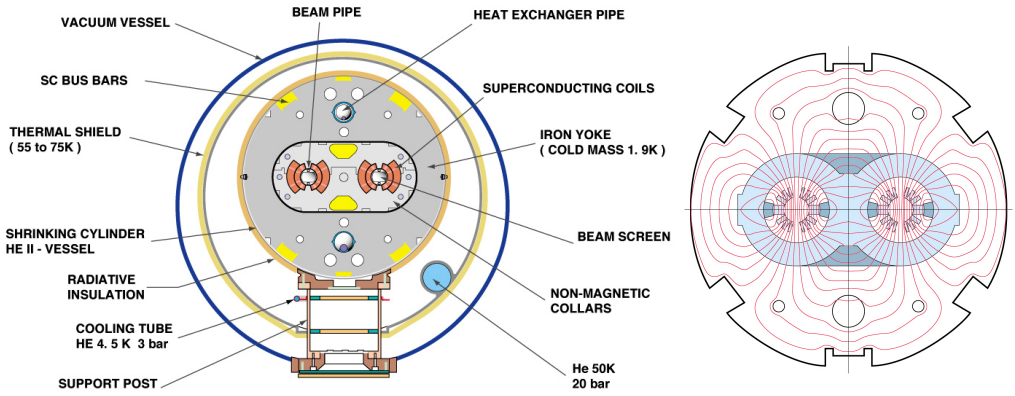

Figure 1.2: Left: Cross section of a LHC dipole magnet used to keep the protons on a circular orbit [34]. Right: Magnetic field configuration in a dipole [32]. A separate pair of super-conducting coils is used for each of the two beams.

In addition to the proton mode described so far, the LHC can also be operated with heavy ions. In this case the nominal energy is 2.76 GeV per atomic mass unit. Questions addressed by the detector Alice ('A Large Ion Collider Experiment') will include the search for a quark-gluon plasma as well as the physics of heavy nuclei.

1.3 The Atlas detector

Atlas is an acronym for A Toroidal LHC Apparatus; as most collision detectors, it is built in layers around the particle interaction point. The overall shape is that of a cylinder with a length of 46 m and a diameter of 22 m (fig. 1.3). The central part is commonly referred to as 'barrel', the two outer, circular sections as 'endcaps'. The main components of Atlas are the Inner Detector, the calorimeter section and the muon spectrometer, which will be described in the following.

Inner Detector: The Inner Detector is the part of Atlas located closest to the beam pipe; its main purposes are the reconstruction of very short-lived particles, the search for secondary vertices and the determination of the exact position of the proton-proton interaction. The Inner Detector combines three different technologies: In the direct vicinity of the interaction point silicon pixel detectors with a position resolution of better than 60 μm in beam direction and 12 μm perpendicular to it are used [11]. The total number of channels is $1.4 \cdot 10^8$. The pixel system is surrounded by the Semiconductor tracker SCT. The SCT is built out of silicon strip detectors which form 4 layers in the barrel and 9 layers in each of the two endcaps. A small rotation between the different layers makes it possible to reconstruct the position of a track in 3 dimensions. The third component of the Inner Detector is formed by the Transition Radiation Tracker TRT. Transition radiation photons created when particles cross stacked layers of polypropylene/-ethylene foil are converted into electrons in the Xenon based operating gas of so-called straw tubes. These

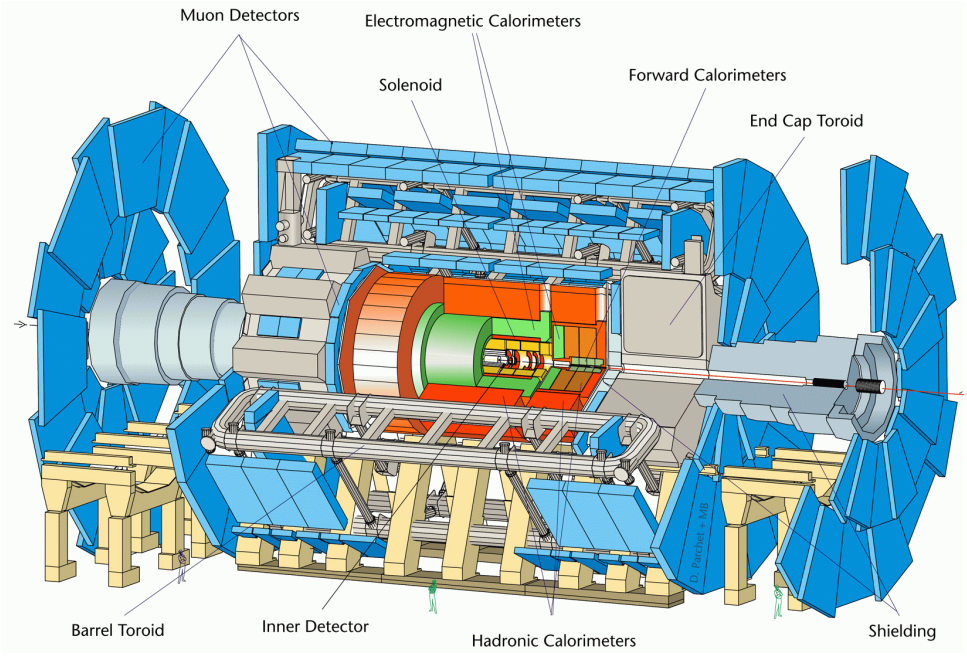

Figure 1.3: 3-dimensional schematic view of the Atlas detector.

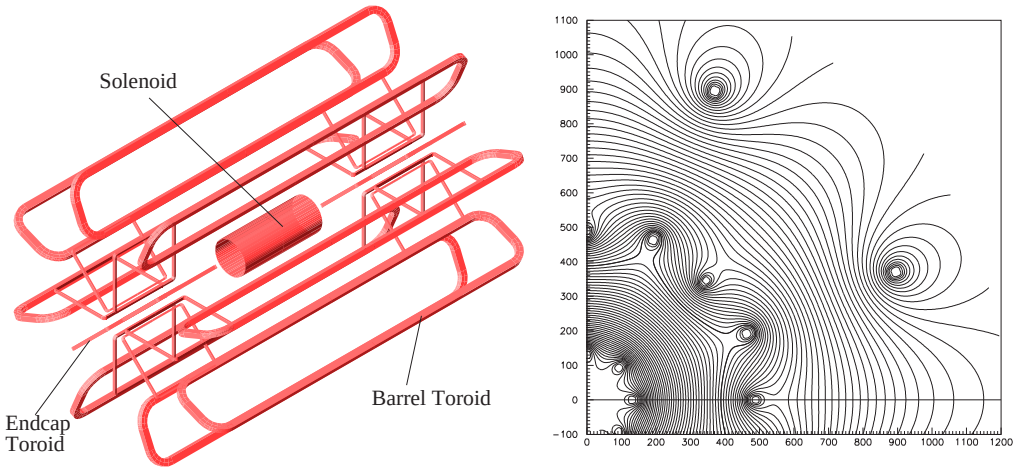

Figure 1.4: Left: Atlas magnet system [12]. At the center of the magnet configuration is a super-conducting solenoid producing a field of 2 Tesla in the Inner Detector region. In the muon spectrometer three separate toroid magnets, each consisting of 8 coils, create a field azimuthal to the detector axis. Right: Magnetic field map in a plane perpendicular to the beam axis in the region between the barrel and one endcap toroid.

are small diameter ionization detectors which use the classic principle of gas amplification near a thin anode wire to produce a visible signal from a small primary ionization. The TRT contributes significantly to the electron pion separation capability of Atlas at low energies[2], while at the same time providing additional track information for charged particles. The combination of silicon pixels, strips and straw tubes guarantees that for each charged particle trajectory more than 40 points in space are measured. Together with the strong magnetic field produced in the Inner Detector by a super-conducting solenoid surrounding it, this allows for a precise reconstruction of low-energetic particle momenta.

Calorimetry: Following the Inner Detector in distance to the interaction point is the Atlas calorimeter system; it occupies the region up to a radius of 4.23 m. Its inner part, the electromagnetic calorimeter, is dedicated to measuring the energy of electromagnetic showers while its outer part, the hadronic calorimeter, performs the same function for hadrons and nuclear fragments. The electromagnetic calorimeter consists of a set of lead absorber plates with liquid argon filling the space between them. Interleaved electrodes collect the charge deposited in the argon by a passing particle; the electrodes are finely segmented which makes it possible to precisely measure the shower shape. For hadron detection in the barrel region a system of iron absorbers, interspersed with plastic scintillators, is used. In the endcap a liquid argon technique similar to the one applied in the electromagnetic section is utilized. The expected energy resolution is $(10\%/\sqrt{E} \oplus 1\%)$ and $(50\%/\sqrt{E} \oplus 3\%)$ in the electromagnetic and the hadronic calorimeter respectively [10].

Magnet system: One of the prominent features of the Atlas detector is its large magnet system which consists of a central solenoid and three toroid magnets (fig. 1.4, left). The solenoid produces a field of 2 Tesla in the Inner Detector region and is needed for the

[2]The intensity of transition radiation produced when a particle crosses the boundary between two materials with different refractive indices depends on its velocity; it is thus different for particles of different rest masses.

momentum reconstruction of low-energetic particles, as explained above. Each of the three toroid magnets, one in the barrel and the other two in the endcap region, is made out of 8 coils. The result is a field configuration in which the field lines surround the detector axis azimuthally (fig. 1.4, right). The toroid system reaches a peak field strength of 3.9 T in the barrel and 4.1 T in the endcaps [12].

Muon Spectrometer

The Atlas subsystem covering by far the largest volume is the muon spectrometer, which forms the outer shell of the experiment. It consists of two fundamentally different types of detectors: Trigger chambers flag when a particle passed a certain region of the detector; with their fast readout they are used to reach a decision whether to store data for a particular event. Precision tracking chambers on the other hand allow for reconstructing muon trajectories. Such tracks are curved due to the presence of the toroidal magnetic field; this makes it possible to determine the muon momentum.
Figure 1.5 shows a cross section of the muon spectrometer in the barrel region. The muon chambers are arranged in three concentric cylinders, commonly referred to as stations, around the beam axis. The inner station (BI[3]) has a distance of approximately 5 m from the centre while the middle (BM) and outer (BO) stations are located at 7.5 m and 10.5 m respectively. Barrel chambers are rectangular in shape with a length of up to 630 cm. Endcap stations take the form of disks which implies a trapezoidal chamber geometry.

Precision chambers: Except for those endcap regions very close to the beam pipe where the background rate is highest[4] , Monitored Drift Tube (MDT) chambers are utilized for track reconstruction. Each MDT has the shape of a cylinder with a radius of 3 cm; a thin wire running along the cylinder axis serves as anode when high voltage is applied to

[3]Muon chambers are labelled as XYZ; X denotes whether a chamber is located in the barrel (X=B) or one of the endcaps (X=E); Y stands for the muon station with 'I' for 'inner', 'M' for 'middle' and 'O' for 'outer'. Z specifies whether a chamber spans the region between two toroid coils (Z=L for 'large') or whether it is found in line with one of them (Z=S for 'small').

[4]Cathode Strip Chambers (CSCs) are used in this region due to their higher rate capability. The position of a traversing particle in this case is obtained from the induced charge distribution in strips attached to the cathode.

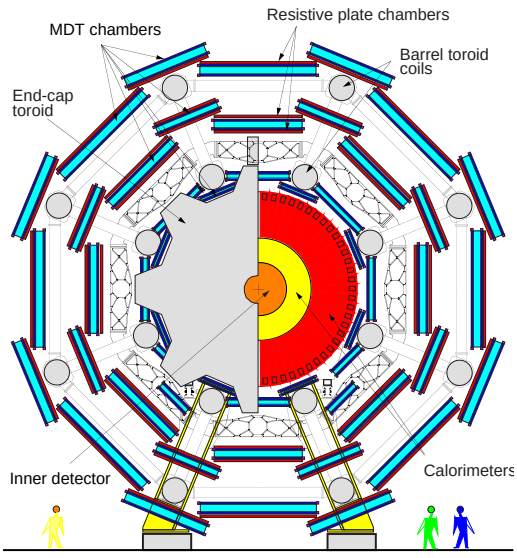

Figure 1.5: Barrel cross section of the Atlas muon spectrometer [13]. All muon chambers are grouped into three concentric stations around the beam axis.

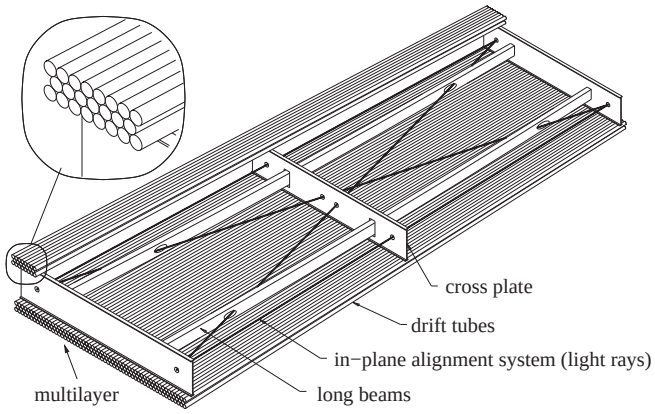

Figure 1.6: Schematic view of a standard MDT chamber [13]. Between 240 and 432 individual drift tubes form two multilayers which are connected by an aluminium support. In each multilayer the MDTs are stacked in either 4 (inner station) or 3 (middle and outer station) layers.

the tube. The resulting electric field causes electrons produced via ionization by a passing particle to drift towards the tube center. Close to the wire gas amplification sets in which greatly increases the number of free electrons. By measuring the time it takes for the electrons to reach the anode ('drift time'), the track position of the muon trajectory can be reconstructed. There are in total 380 000 MDTs in Atlas; they are assembled into 1194 chambers (fig. 1.6) with the individual tubes firmly attached to each other by glue joints. The integrated magnetic field of the toroid between the inner and the outer muon station is typically 3 Tm in the barrel and 6 Tm in the endcap region. This values translate into a sagitta[5] of only 500 μm for muon tracks of 1 TeV energy. The design goal of the Atlas muon spectrometer is a transverse momentum resolution of

$$\frac{\Delta p_t}{p_t} < 10^{-4} \cdot \frac{p}{\mathrm{GeV}} \tag{1.1}$$

for a momentum $p > 300\,\mathrm{GeV}$. For lower momenta the resolution is limited to a few percent by multiple scattering. In order to reach (1.1), which implies a position resolution of 50 μm in each of the three stations, not only the resolution of the individual drift tubes must be very good ($\lesssim 80\,\mu$m), but also the relative position of the wires and chambers with respect to each other must be known to a very high degree of precision. Within each chamber this is achieved by a special assembly procedure in which the MDTs are held in a precision jig on a granite table during the glueing process. Chamber deformations due to temperature changes and gravitational forces are measured continuously during the operation of Atlas with the help of light rays (fig. 1.6). An LED at one end of the chamber is used together with a lens mounted on the middle cross plate to project an encoded chess-board pattern mask onto a CCD camera at the other chamber end. Changes in the chamber geometry will result in a movement or rotation of the image; by analysing the CCD data this can be corrected for during the track reconstruction process. The system described is known as 'in-plane alignment'; only the continuous recording of the chamber shape, a concept which was rarely applied for large-scale detectors before but which is a

[5]The sagitta is the distance of the muon trajectory in the middle station from the straight line one obtains by connecting the track position in the inner and outer stations.

core feature of the Atlas muon spectrometer, turns a drift tube into an MDT, with the 'M' standing for 'monitored'.

Global alignment system: Owing to the large size of the muon system, relative chamber movements with respect to each other of up to several millimeters can be expected when the toroid magnet is switched on or as a consequence of temperature variations. Equally important to the measurement of the individual chamber shapes is therefore the monitoring of the total muon spectrometer geometry. This so-called 'global alignment system' is, as the in-plane one, based on optical sensors connected by light rays. The barrel chambers are arranged such that they form projective towers (fig. 1.7): The hypothetical lines connecting the corners of an inner, middle and outer station chamber point towards the interaction point. Adjacent chambers are optically linked by proximity sensors; axial lines are parallel to the beam axis and connect chambers within a station. A set of projective alignment rays finally provides for a connection of the three stations themselves. In the endcap region the situation is slightly more difficult since the vacuum vessels of the endcap toroids block the line of sight between some of the stations. In addition to the elements described above for the barrel, a system of rigid reference bars is therefore used. These are cylindrical metal tubes which are themselves equipped with an optical system to monitor their deformation. Sensors mounted on the alignment bars are then utilized to interconnect the individual chambers and stations.
Table 1.1 summarizes the different contributions to the precision with which a wire position is known; figure 1.8 demonstrates the high accuracy with which the momentum of a high-energetic muon can be determined from the muon spectrometer data alone. This stand-alone capability is, in addition to the large toroid magnet system, a unique feature of the Atlas design.

Trigger chambers: Trigger chambers are Resistive Plate Chambers (RPCs) in the barrel and Thin Gap Chambers (TGCs) in the endcap. An RPC consists of a pair of parallel bakelite plates of high resistivity with a well defined distance; the gap between the two plates is filled with a gas mixture on the basis of tetrafluoroethane ($C_2H_2F_4$). A high voltage of several kilovolts is applied across the gap; this causes primary ionization electrons produced by a traversing particle to multiply while drifting towards the anode. Signals

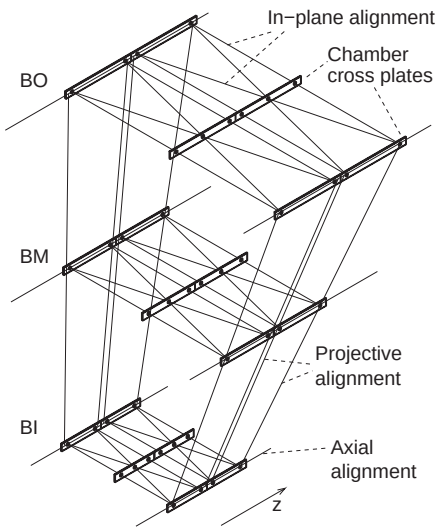

Figure 1.7:
Muon chamber alignment for the barrel region [9]. All chambers are arranged such that the lines connecting their corners point towards the interaction point ('projective towers'). A set of optical alignment rays is used to monitor chamber movements. Axial lines run parallel to the beam axis while projective lines connect different stations. Adjacent chambers are additionally connected by so-called proximity sensors (not shown).

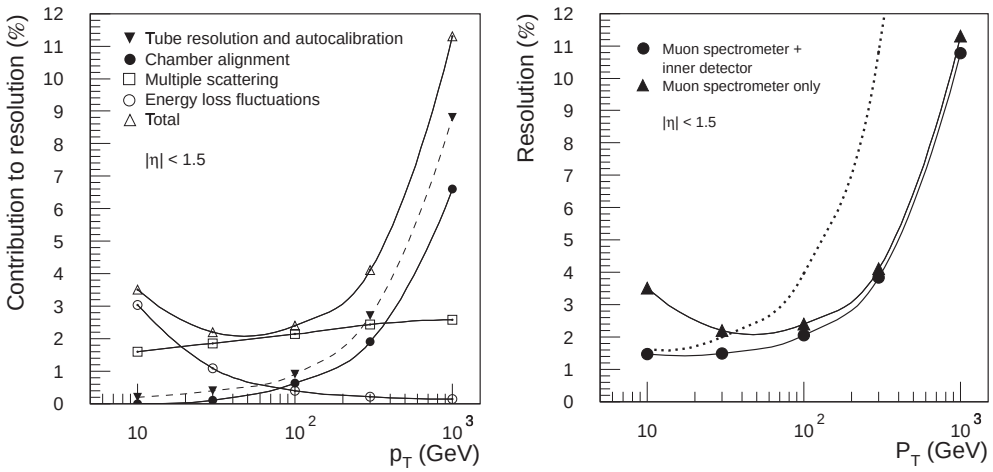

Figure 1.8: Muon spectrometer momentum resolution [13]. Left: Resolution using only the muon spectrometer. Above an energy of 300 GeV the dominant contribution stems from the single tube resolution, followed by the chamber alignment. For $p_t = 1$ TeV the relative precision $\Delta p_t/p_t$ is about 10% which meets the requirement of equation (1.1). Right: Combined momentum resolution of the Inner Detector and the muon spectrometer. One can see that for energies above ≈ 100 GeV the muon spectrometer stand-alone performance almost equals the combined one. The dotted line is the resolution achievable using only the Inner Detector.

are read out via capacitive coupling by a set of metal strips on the outside of the bakelite plates. Strips on the two sides of the chamber are perpendicular with respect to each other; 'η-strips' are parallel to the MDT wires; they reflect the bending of a track in the muon spectrometer. 'φ-strips' provide the second coordinate of a trajectory, i.e. the position in direction of the MDT axis. The time resolution of a RPC is 1.5 ns with a granularity of about 3 cm.
As to their principle of operation, TGCs are multi-wire proportional chambers with a distance between the anode and the cathode plane that is smaller than the anode wire pitch. The electric field configuration and the short drift distance provide for a good time resolution and a fast response. In Atlas all TGCs are arranged such that their wires are parallel to the MDT ones. A signal is read out both from the anodes and from strips attached to the cathode. As in the case of the RPCs this allows for establishing the track

Parameter	Requirement
Wire position within a MDT	$\leq 10\,\mu$m r.m.s.
Relative positioning accuracy of MDTs within a chamber	$\leq 20\,\mu$m r.m.s.
Local chamber alignment (in-plane alignment)	$\leq 10\,\mu$m
Global chamber alignment (sagitta correction)	$\leq 30\,\mu$m
Intrinsic single MDT resolution	$\approx 80\,\mu$m

Table 1.1: Contributions to the MDT wire position accuracy. In order to reach a momentum resolution of 10% for an energy of 1 TeV (equation (1.1)), the requirements given in the right column must be met.

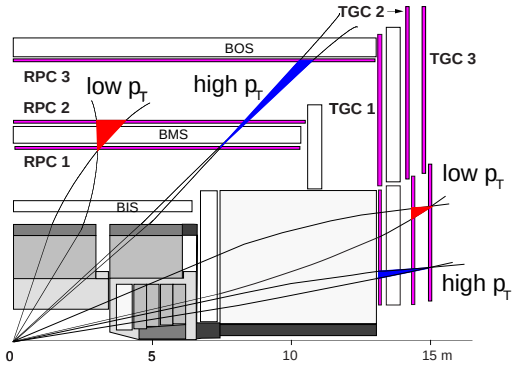

Figure 1.9:
Atlas level-1 muon trigger scheme [13]. A low-p_t trigger ($p_t > 6\,GeV$) requires a coincidence of hits in two trigger chambers while for a high-p_t trigger ($p_t > 20\,GeV$) hits in 3 planes are needed.

position in two dimensions.

Trigger scheme: The rate with which events occur at Atlas is equal to the LHC bunch crossing frequency of 40 MHz, multiplied with the average number of proton-proton collisions per bunch crossing. For a luminosity of $10^{34}\,\mathrm{cm}^{-2}\mathrm{s}^{-1}$, one arrives at an interaction rate of 10^9 Hz. Most of these events are of no interest from a particle physics point of view; it is therefore neither desirable, nor is it actually practicable due to the large amount of data, to store all information measured by the different sub-detectors for later offline analysis. Atlas implements a three level trigger system to select those events which might contribute to finding an answer to the still open question of particle physics. The so-called level-1 trigger reduces the rate to 75 kHz, examining relatively crude data from selected parts of the experiment (muon spectrometer, calorimeter). Events passing the level-1 trigger are examined more closely by the level-2 and level-3 algorithms. The final rate with which events are released for permanent storage on tape is about 100 Hz.
The principal objective for the muon level-1 trigger is the selection of muons with a transverse momentum $p_t > 6\,\mathrm{GeV}$ at a luminosity $\mathcal{L}$ of $10^{33}\,\mathrm{cm}^{-2}\mathrm{s}^{-1}$ and $p_t > 20\,\mathrm{GeV}$ at $\mathcal{L} = 10^{34}\,\mathrm{cm}^{-2}\mathrm{s}^{-1}$. The latter condition is usually referred to as 'high-p_t' trigger, the former as 'low-p_t' trigger. Figure 1.9 illustrates the way in which the selection works: Both in the barrel and in the endcap the trigger chambers, respectively RPCs or TGCs, are located on either side of the middle muon station. A third layer of RPCs is installed adjacent to the MDTs of the outer station. The low-p_t trigger uses predefined coincidence patterns, consistent with the bending power of the toroid, in two trigger planes. For the high-p_t trigger the additional presence of hits in a third plane is required. The thresholds of 6 GeV and 20 GeV were chosen such that the event rate is reduced sufficiently while the discovery potential for a Higgs decaying into a final state involving muons is affected as little as possible.

1.4 Atlas physics potential

Higgs sector

As already pointed out in section 1.1, the discovery of one or several Higgs bosons will be fundamental for a better understanding of the mechanism of electroweak symmetry-breaking. In the Standard Model the Higgs sector is largely unconstrained; from theoretical considerations one obtains an upper limit on the Higgs mass m_H of around 1 TeV. Additional constraints can be derived if one requires the perturbative nature of the Standard Model to be valid up to a certain energy scale Λ. If the cutoff value is chosen only at the

Planck mass, i.e. if no new physics appears below this scale, then m_H must be in the range between ≈130 GeV and ≈190 GeV [15]. This restriction becomes weaker if new physics appears already at lower energies. For $\Lambda \approx 1\,\text{TeV}$, which is favoured by the advocates of super symmetry, the Higgs mass is constrained to $50\,\text{GeV} < m_H < 800\,\text{GeV}$.
Experimentally, bounds on m_H stem from direct searches and from high precision measurements in the electroweak sector which is sensitive to the Higgs mass via loop corrections. The present best fit to all available data predicts $m_H = 88^{+53}_{-35}\,\text{GeV}$ [58]. A Higgs mass below 114.1 GeV is excluded on a 95% confidence level by the combined results of the LEP experiments Aleph, Delphi, L3 and Opal [58].
Figure 1.10 shows some of the processes by which a Higgs boson can be produced at the LHC. The two dominant mechanisms are gluon fusion and the fusion of two W's. Of the Higgs decay modes only some have a signature which makes it possible to sufficiently distinguish them from background events. The most promising ones at Atlas are

- $H \to \gamma\gamma$: This is a rare decay, only observable for a small Higgs mass where both the production cross section and the branching ratio are relatively large. It requires an excellent energy and angular resolution in the electromagnetic calorimeter to observe the narrow mass peak caused by the Higgs decay over the large irreducible background.

- $H \to b\bar{b}$: This is the dominant mode if m_H is smaller than twice the W mass. The direct production $gg \to H$ with $H \to b\bar{b}$ cannot be extracted from the huge QCD[6] two-jet background. This mode can therefore only be observed if a Higgs is produced together with a W-boson or a $t\bar{t}$ pair; the leptonic decays of the W and semi-leptonic decays of the top pair in this case provide a handle to distinguish events from background.

- $H \to ZZ^{(*)} \to 4l$: This is the 'gold-plated' mode for a Higgs mass between 130 GeV and 800 GeV. Its clear signature with 4 leptons (e, μ), which makes detection relatively easy, had a large influence on the design choice for the Atlas muon spectrometer.

- $H \to ZZ \to ll\nu\nu$ and $H \to WW \to l\nu jj$: Above $m_H \approx 800\,\text{GeV}$ the 4 lepton mode becomes rate-limited; processes involving neutrinos in the final state provide the best chance for discovering a Higgs particle in this mass range.

- $H \to ZZ \to lljj$: This is a decay which is mainly important for a Higgs mass close to 170 GeV. In this region the branching ratio of the $H \to ZZ^* \to 4l$ channel is reduced since the $H \to WW$ mode opens up.

[6] QCD: Quantum Chromo Dynamics, the theory describing the strong interaction

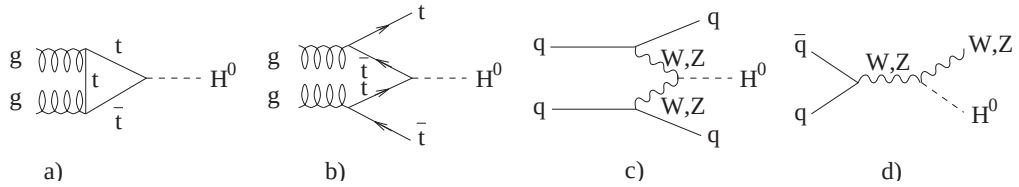

Figure 1.10: Higgs production mechanisms in proton-proton collisions. The dominant processes at the LHC are gluon fusion (a) and the fusion of two W bosons (c).

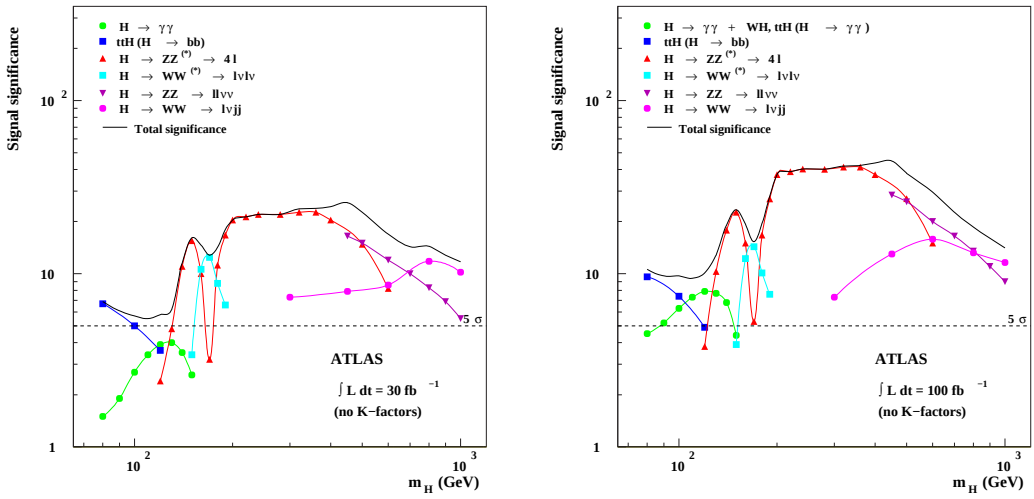

Figure 1.11: Discovery potential for a Standard Model Higgs with Atlas [15]. The left plot shows the sensitivity expected for different decay channels after 3 years of data taking at a luminosity $\mathcal{L}$ of $10^{33}\,cm^{-2}s^{-1}$; the right plot corresponds to one year running at $\mathcal{L} = 10^{34}\,cm^{-2}s^{-1}$.

Figure 1.11 shows the signal to background ratio for the different channels as expected at Atlas after 3 years of data taking at a luminosity of $10^{33}\,\mathrm{cm}^{-2}\mathrm{s}^{-1}$ ($30\,\mathrm{fb}^{-1}$) and for one year at the nominal luminosity of $10^{34}\,\mathrm{cm}^{-2}\mathrm{s}^{-1}$ ($100\,\mathrm{fb}^{-1}$). A Standard Model Higgs can be discovered with a statistical significance of at least 5σ within the first few years of LHC running for the full mass range up to 1 TeV.

Super Symmetry

Atlas will focus on the discovery of super symmetry in various ways. As has been discussed in section 1.1, SUSY models predict the existence of more than one Higgs boson ($h, H, A, H^{\pm}$). For the MSSM at tree level all Higgs masses and couplings can be expressed in terms of only two parameters, which are normally chosen as a mass m_A and the tangent of an angle β. Figure 1.12 shows in which region of the m_A-tan β plane a detection of SUSY Higgs particles will be possible with Atlas. One can see that for an integrated luminosity of $300\,\mathrm{fb}^{-1}$ almost the complete parameter space is covered.
In addition to searching for the Higgs bosons h, H, A and $H^{\pm}$ Atlas will concentrate on detecting super symmetric particles directly. The SUSY cross section is dominated by gluinos[7] and squarks[8]; they should be strongly produced with a cross section similar to the Standard Model QCD background. Gluinos and squarks will decay into the lightest super symmetric particle (LSP), which may either be stable or may itself decay into Standard Model particles. The decay typically involves a number of intermediate stages, which lead to a variety of signatures including multiple jets, leptons, missing energy, as well as W and Z bosons.
Due to the high luminosity of LHC and therefore the large number of expected events, Atlas should not only be able to discover SUSY, if it exists at a mass scale of ≈ 1 TeV, but

[7] the super partners of gluons
[8] the super partners of quarks

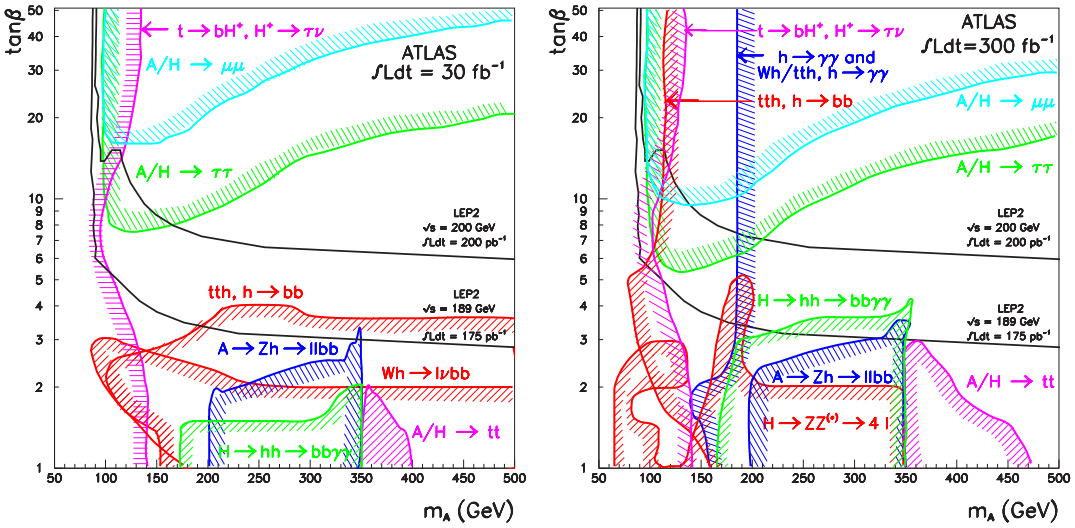

Figure 1.12: Atlas sensitivity for the discovery of MSSM Higgs bosons with a statistical significance of 5σ [15]. The shaded areas indicate the side of the contour curves where different signals would be observable in the so-called 'minimal mixing scenario', the most difficult case for LHC. The solid lines denote the region excluded by the results from LEP.

it should also be possible to test the different super symmetric models and to determine some of their (numerous) parameters.

Other fields of interest

With its large center of mass energy LHC is well suited to study QCD effects. Of particular interest in this context is the measurement of the strong coupling constant α_s and the determination of the parton and gluon densities of the proton in regions which have been inaccessible so far. Another attractive field are processes involving top quarks, which will be produced in a large number. Both an accurate measurement of the top mass and the detailed investigation of the top decay channels will be possible. A last area worth mentioning is B-physics; here one especially expects new insights into the phenomenon of CP violation.

'You have to understand the whole to understand the smallest part.'
J.W. Goethe, 1749 – 1832

Chapter 2

(Atlas Monitored) Drift Tubes

This chapter discusses the working principle of drift tubes. Particular emphasis is put on the different physical processes involved from the passage of a particle through the detector to the generation of a signal at the output (section 2.2). The background conditions expected at the LHC are also summarized (section 2.3).

2.1 Atlas MDTs

The basic components of an Atlas drift tube are shown in figure 2.1. Each MDT consists of a 29.97 mm outer diameter aluminium tube, a gold plated tungsten-rhenium wire with a diameter of 50 μm running along the tube axis and two endplugs which close off the MDT at both ends. Each endplug comprises a body made of modified polyphenylenether (PPE, sold by the company General Electric under the brand name Noryl®), re-enforced with glass fibres, an accurately machined outer aluminium ring and a high precision central brass insert (fig. 2.2). The different materials are firmly attached to each other by mould injection of the Noryl polymer during the production process.
In addition to sealing the two ends of the MDTs, the endplugs provide electrical insulation between the high voltage carrying anode wire and the outer tube wall; they further fixate

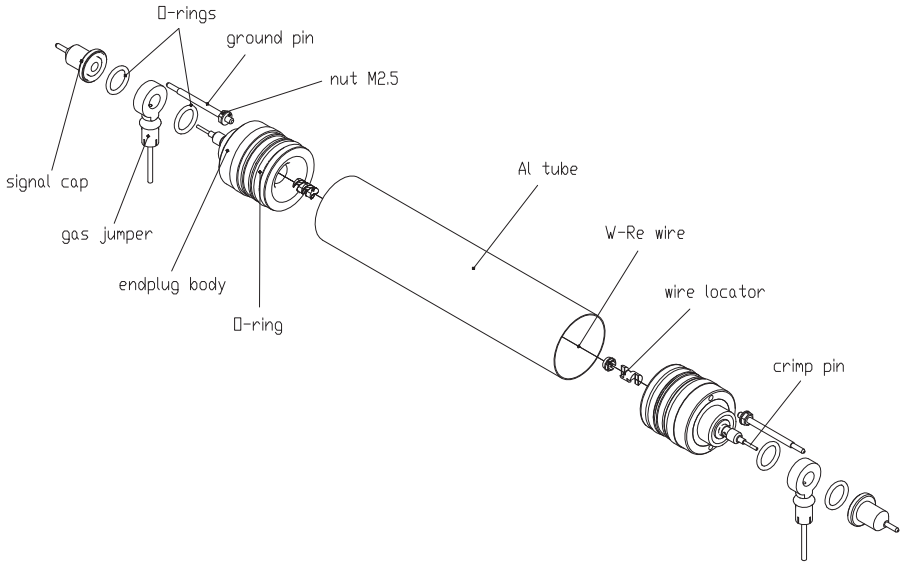

Figure 2.1: Exploded view of an Atlas Monitored Drift Tube [16].

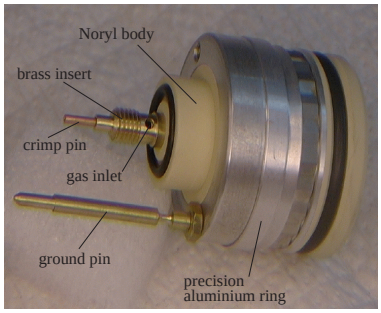

Figure 2.2:
Photograph of an MDT endplug. The hole visible in the brass insert is used to supply the tube with gas during operation. The copper crimp pin fixates the anode wire in the assembled drift tube.

and position the wire with respect to the aluminium tube and allow the connection of the MDT to the gas distribution and front end electronics. The precisely machined outer surface of the endplug is used during assembly of the individual MDTs into a precision chamber to control the relative position of the wires to the required 20 μm level.

2.2 Principle of operation

Drift tubes are gas-filled ionization detectors which operate in proportional mode. The thin anode wire is supplied with a high voltage of typically a few kV, while the metallic tube wall is grounded. Electrons and ions created in pairs by a traversing ionizing particle drift towards the anode and the cathode respectively in the radially symmetric electric field

$$E(r) = \frac{V}{\ln b/a} \cdot \frac{1}{r}\,, \tag{2.1}$$

where V is the anode wire potential, b the tube and a the wire radius.
Close to the wire the electric field is sufficiently high for the drifting electrons to gain enough kinetic energy to cause secondary ionization; the total number of electron-ion pairs increases by a factor G known as gas gain or gas amplification. For the Atlas MDTs the nominal gas gain was chosen as $2 \cdot 10^4$ [13]. Other important operating parameters are summarized in table 2.1. In the following the consecutive processes involved in the signal generation of a drift tube are reviewed in more detail.

Parameter	Nominal value
Outer tube radius	14.985 mm
Wall thickness	400 μm
Tube material	Aluminium
Anode wire radius	25 μm
Anode wire material	W-Re alloy (97:3), gold-plated
Anode wire resistance	44 Ω/m
Operating gas	Ar:CO_2 = 93:7 (Vol.-%)
Operating pressure	3 bar (abs.)
Gas gain	$2 \cdot 10^4$
High voltage	3080 V

Table 2.1: Important MDT operating parameters.

2.2.1 Ionization

Muons: For muons and other charged particles the average energy loss when traversing a material layer of thickness dx is described by the Bethe-Bloch formula [58]

$$-\frac{dE}{dx}\cdot\frac{1}{\rho} = Kz^2\cdot\frac{Z}{A}\cdot\frac{1}{\beta^2}\cdot\left(\frac{1}{2}\ln\frac{2m_ec^2\beta^2\gamma^2T_{max}}{I^2}-\beta^2\right) \tag{2.2}$$

with $K = 0.31\,\mathrm{MeV\,g^{-1}cm^{-2}}$. In this equation ρ is the density, Z the atomic number and A the mass number of the absorbing material; z is the charge of the traversing particle. The dimensionless parameters β and γ are defined in the standard way as $\gamma = E/(mc^2)$ and $\beta^2 = 1 - 1/\gamma^2$. T_{max} is the maximum kinetic energy which can be imparted to a free electron in a single collision; I is the mean excitation potential of the absorbing material. Formula (2.2) describes the mean energy loss of a particle in matter only; fluctuations around the average value can be significant. In the case of a thin absorber, i.e. in particular for gases, the actual energy deposition follows a Landau distribution [51]

$$f(\lambda) = \frac{1}{\pi}\cdot\int_0^\infty e^{-s\ln s - s\cdot\lambda}\cdot\sin(\pi s)\,ds\,, \tag{2.3}$$

where the parameter λ is a function of the actual deposited energy E, the mean energy loss $\bar{E}$ and the absorber material and its dimensions. Since (2.3) cannot be written in an analytic form, one often uses the so called Moyal approximation [53]

$$f(\lambda) = \sqrt{\frac{e^{-(\lambda+e^{-\lambda})}}{2\pi}} \quad \text{with} \tag{2.4a}$$

$$\lambda := \frac{E-E_p}{\xi}\,. \tag{2.4b}$$

E_p is the most likely energy loss and ξ the width parameter of the distribution. Figure 2.3 shows both the Landau and the Moyal distribution. One can see that the Moyal approximation does not have the pronounced tail towards high energies as the Landau function. On the other hand the approximation is a pretty good one when restricted to the rising edge and the center of the peak of the distribution.
The average energy needed to ionize a single argon atom is [27]

$$n_p = 26\,\mathrm{eV}\,, \tag{2.5}$$

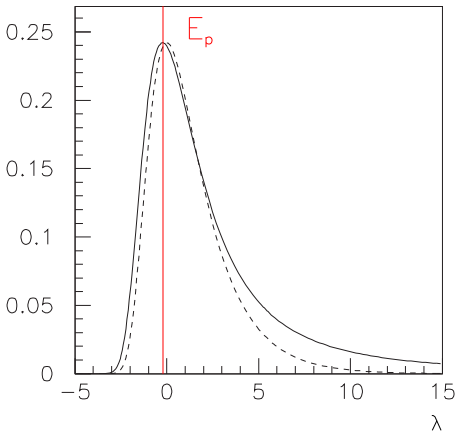

Figure 2.3:
Moyal approximation (dashed curve) for a Landau distribution (solid line). One can see that the approximation is good for the rising edge of the distribution, but does not correctly reproduce the long tails which are due to a small number of very high individual energy losses ('knock-on collisions'). The Landau distribution was numerically computed using the function DENLAN() of the CERN program library CERNLIB.

more or less independent of the type of ionizing particle. In a fraction of events the produced electron has enough energy to cause secondary ionization itself, usually very close to the point of the original interaction. This leads to the formation of electron-ion clusters along the particle trajectory. In some cases the electron produced has an energy high enough to travel a macroscopic distance; this so-called 'δ-electrons' will be discussed below. Figure 2.4 shows the cluster size distribution for a 100 GeV muon in an MDT. A consequence of both the cluster size fluctuations and the finite distance between the points of ionization is that muon signals of a drift tube typically show more than one maximum (fig. 2.5); this is in particular true for tracks close to the wire for which the drift distance is largely different for electrons produced close to the tube wall and in the middle of the track.

Photons: Photons below 1.02 MeV can interact with the operating gas or the tube wall of an MDT either by the photo-electric effect or by Compton scattering. In the first case, which dominates at low energies, the full photon energy E_γ is transferred to a single electron; for $E_\gamma \lesssim 25\,\text{keV}$ the range of the produced photo electron in argon at 3 bar is of the order of a few millimeters maximum[1]. The consequence is that the full photon energy is deposited in the drift gas over a relatively small path length — the MDT signal of such interactions shows a single peak without the multiple maxima typical of muons (fig. 2.6, left plot). Measured pulse charge spectra are usually Gaussian in shape; (mono-energetic) γ-sources of a few tens of keV energy like ^{109}Cd are therefore well suited for pulse height studies.

[1] For a 25 keV electron e.g. one finds a range of 4.5 mm [54].

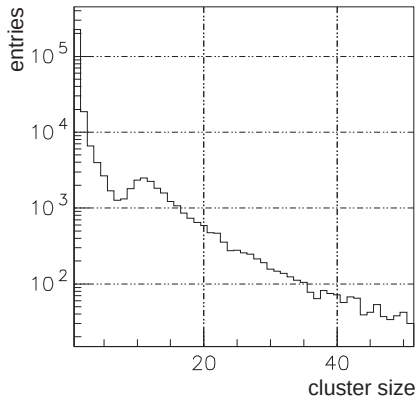

Figure 2.4:
Electron cluster size distribution for a 100 GeV muon in Ar:CO_2 = 93 : 7 at 3 bar pressure. The shown graph is the result of a simulation with the program packages GARFIELD [71] and HEED [67]. The distribution has a sharp peak at 1. Please note the logarithmic vertical scale.

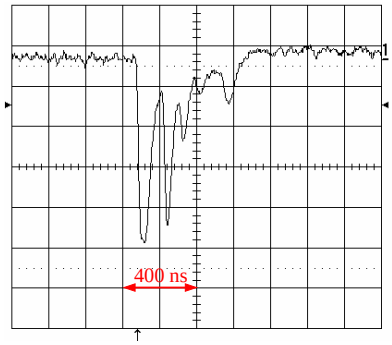

Figure 2.5:
MDT signal generated by a muon. For tracks not too close to the tube wall the signal typically shows several maxima; these are caused by different ionization clusters along the muon trajectory.

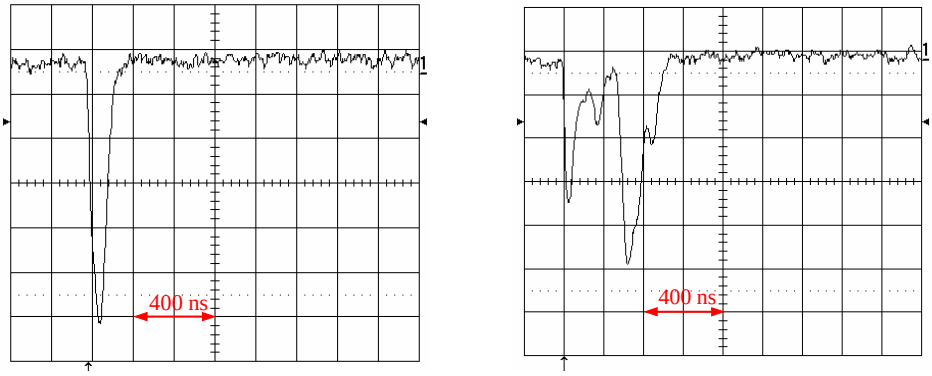

Figure 2.6: Left: MDT signal generated by a 22 keV photon from a ^{109}Cd source. The signal shows a single peak structure. Right: MDT signal generated by a 660 keV photon from a ^{137}Cs source. The signal looks similar to the one caused by a muon and is typical of photons interacting via Compton scattering.

For higher photon energies (typically above $\approx 100\,\text{keV}$) Compton processes prevail; in this case the energy E_e imparted to a quasi-free electron in a single Compton interaction is not fixed but follows a variant of the Klein-Nishina formula, namely [51]

$$\frac{d\sigma}{dE_e} = \frac{\pi \cdot r_e^2}{m_e c^2 \gamma^2} \cdot \left[2 + \frac{s^2}{\gamma^2 (1-s)^2} + \frac{s}{1-s} \cdot (s - \frac{2}{\gamma}) \right] \tag{2.6}$$

where $\gamma := E_\gamma / m_e c^2$ and $s := E_e / E_\gamma$. (2.6) is non-zero up to a maximum energy of

$$E_{e,max} = E_\gamma \cdot \frac{2\gamma}{1+2\gamma}\,, \tag{2.7}$$

which is known as Compton edge.
MDT signals caused by Compton interactions look similar to the ones caused by muons (fig. 2.6, right plot); this is due to the fact that in a large fraction of the cases the Compton recoil electrons have enough energy to traverse the complete tube. The deposited energy or charge spectrum is difficult to calculate since not only the Compton process itself but also the energy loss of the recoil electron in the gas and its angular direction has to be taken into account.

δ-electrons: It was mentioned already that muons traversing an absorber will in some cases transfer an exceptionally high fraction of their energy to an electron of the absorber material in a single collision. Such electrons are known as δ- or 'knock on' electrons. They are typically energetic enough to produce themselves a secondary track of significant length. For the operation of drift tubes they play an important role as they can cause a fake drift radius measurement: This is the case if a δ-electron, usually produced in the aluminium tube wall, causes a secondary track which passes closer to the wire than the original muon trajectory. In that case electrons from the fake track reach the anode wire earlier than the fastest electrons from the true track; the obvious result is a too small measured drift time and thus drift radius and as a consequence a reduced track reconstruction efficiency.

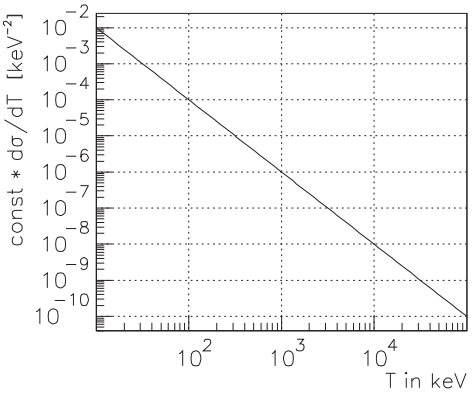

Figure 2.7:
Cross section $d\sigma/dT \cdot const$ for the production of δ-electrons by a 100 GeV muon with $const = (2\pi \cdot Z \cdot r_0^2 \cdot m_e)^{-1}$. One can clearly see that the probability for the production of a δ-electron decreases rapidly with its kinetic energy T.

The cross section for the production of a δ-electron with kinetic energy T is given by [23]

$$\frac{d\sigma}{dT} = 2\pi \cdot Z \cdot r_0^2 \cdot m_e \cdot \frac{1}{\beta^2 \cdot T^2} \cdot \left[1 - \beta^2 \frac{T}{T_{max}} + \frac{T^2}{2E_\mu^2}\right] . \tag{2.8}$$

E_μ is the energy of the traversing muon, r_0 the electron radius. The remaining variables are the same as in equation (2.2). Figure 2.7 shows the cross section (2.8) versus T for 100 GeV muons. One can see that the probability for the production of δ-electrons decreases rapidly with their kinetic energy.

2.2.2 Electron drift

The movement of the primary electrons produced along the trajectory of a charged particle traversing a drift tube is governed both by the electric field (2.1), which exerts a force in direction of the wire, and by frequent collisions with the molecules of the operating gas. The drift process can be described by the so called rt-relation $r(t)$ which for each track distance r from the wire gives the corresponding time t the fastest electrons need to reach the anode and produce a signal. An accurate knowledge of the rt-relation, in the case of the Atlas MDTs to a level of $\leq 20\,\mu$m, is a prerequisite for using drift tubes to precisely reconstruct particle tracks.
The rt-relation is highly dependent on the chosen operating gas and on the operating parameters. The MDT mixture, Ar:CO_2=93:7, belongs to the group of so-called non-linear drift gases for which the electron drift velocity v_{drift} is not independent of the reduced electric field strength E/ρ where ρ is the gas density. It immediately follows that v_{drift} is not constant over the cross section of the tube (fig. 2.8).

Diffusion: Without the presence of an electric field any movement of the primary electrons is due to diffusion according to the equation

$$\frac{\partial n(\vec{x}, t)}{\partial t} - D \cdot \Delta n(\vec{x}, t) = 0\,, \tag{2.9}$$

where n is the electron density and D the diffusion coefficient. Electrons localized at a position $\vec{x}_0$ at time $t = 0$ will show a Gaussian distribution with center $\vec{x}_0$ and width $\sigma \sim \sqrt{Dt}$ for times $t > 0$. If the electric drift field is 'turned on', longitudinal (in direction of the electric field lines) and transverse diffusion are usually different from each other. Both have the effect that the individual electrons follow a zigzag path towards the anode

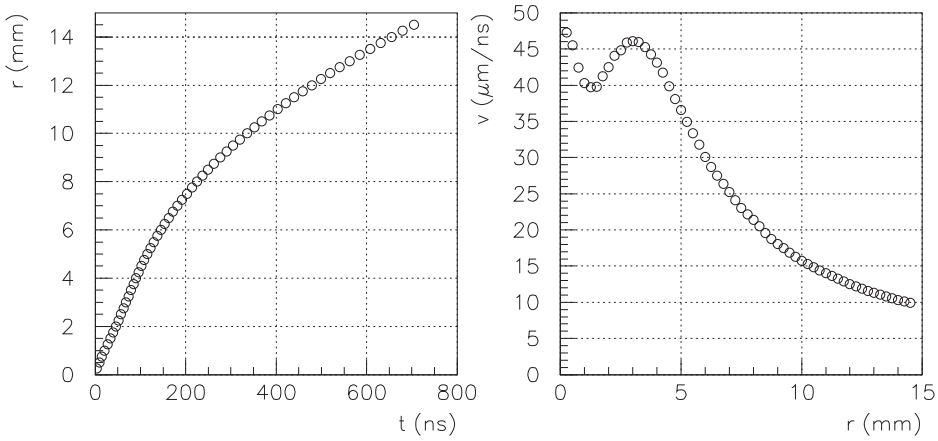

Figure 2.8: Rt-relation and drift velocity for the MDT operating mixture Ar:CO_2=93:7. The drift gas is non-linear; the electron drift velocity is significantly larger close to the wire than close to the tube wall. The shown graphs are the result of simulations with the program packages GARFIELD [71] and MAGBOLTZ [26].

wire rather than a straight line. The actual path length travelled by an electron is not fixed but follows a distribution with a finite width; the same is true for the drift time. Diffusion is therefore one of the limiting factors for the position resolution of a drift detector.

Influence of trace impurities: The presence of certain admixtures in the gas even at concentrations of a few hundred to a few thousand parts per million can have a large impact on the drift process, either by changing the transport parameters itself or due to electron capture. The latter will result in a loss of signal height, especially for long drift distances. The most common trace impurities are oxygen, nitrogen and water. Oxygen and nitrogen will usually get into the active volume of a drift chamber through small leaks in the detector itself or in the gas system. Water is ubiquitous in almost any system due to outgassing and surface desorption effects. A second mechanism for the accumulation of water is by diffusion through plastic materials which are often permeable for H_2O molecules to a greater or lesser extent.
Figure 2.9 shows simulation results for the influence of different water concentrations on the maximum drift time[2] t_{max} for an Atlas MDT operated with the standard Ar:CO_2 mixture. The large change in t_{max} with the amount of water in the gas is caused by the water molecules having a large static electric dipole moment. This leads to an exceptionally high inelastic scattering cross section for electrons due to excitation of rotational degrees of freedom [25]. Electron capture effects and thus a loss of signal height are negligible (fig. 2.10).
Trace levels of oxygen or air in Ar:CO_2 drift mixtures have only a small influence on the electron transport. The main problem with O_2 is its large electro-negativity and thus a high affinity towards electrons [46]. Its concentration in a drift gas has to be well controlled in order to avoid a large signal attenuation. For the Atlas MDTs the maximum oxygen concentration permitted is 100 ppm.

[2]The maximum drift time is the time needed for electrons to drift from the tube wall to the anode.

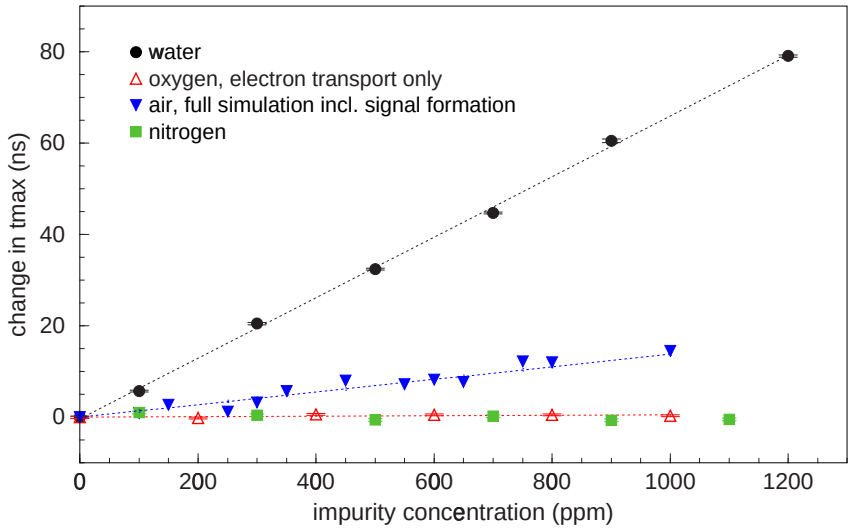

Figure 2.9: Simulation results obtained with the program GARFIELD [71] for the change of the maximum drift time t_{max} with the concentration of common impurities in the operating gas for Ar:CO_2=93:7. The data for air is taken from [68]. Traces of oxygen or air do not affect the electron transport itself; they however do have an influence on t_{max} if the full signal formation is included in the simulation; this is due to the fact that oxygen impurities cause a loss in signal height which shifts the time the signal crosses a given discriminator threshold.

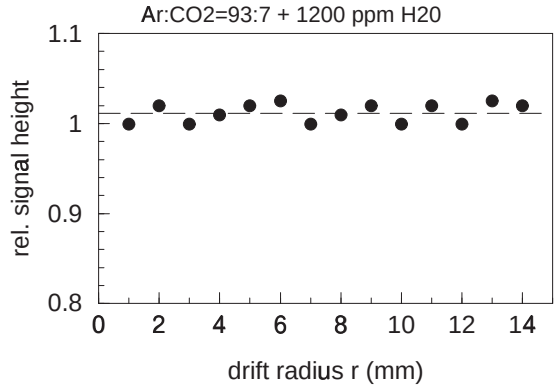

Figure 2.10: Influence of trace levels of water in the MDT operating gas on the signal height. The graph shows the simulation result obtained with the program GARFIELD [71] for single electron clusters produced at a distance r from the wire and a water concentration of 1200 ppm. No signal attenuation is visible.

2.2.3 Ion drift

The majority of drifting ions in an MDT is produced during the gas amplification process close to the anode wire. The small fraction of ions which are created directly during the primary ionization process is negligible for a gas gain of $2 \cdot 10^4$. Typical ion drift velocities v_{ion} are of the order of a few mm/ms. For small field strengths, v_{ion} is proportional to the electric drift field E [27], i.e.

$$v_{ion} = \mu \cdot \frac{E}{p} \,. \tag{2.10}$$

The constant μ is known as ion mobility; p is the gas pressure.
For Ar^+ ions in Ar (2.10) is a good approximation up to field strengths of about 20 V per cm and Torr, as can be seen from figure 2.11. For an MDT operated at nominal high

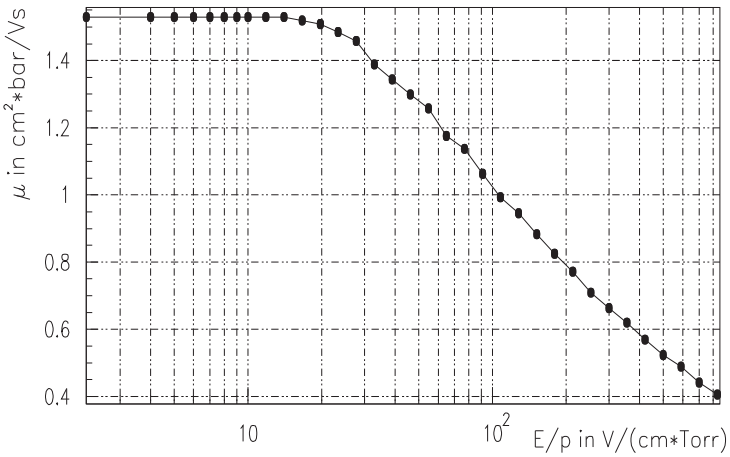

Figure 2.11:
Ion mobility μ for Ar^+ in Ar [28]. Up to field strengths of 20 V/(cm·Torr) μ can be considered as constant. For an MDT operated under nominal conditions this corresponds to $r \gtrsim 100\,\mu$m; equation (2.10) is therefore a good approximation for all radii except in the direct vicinity of the wire.

voltage this corresponds to $r \gtrsim 100\,\mu$m; the assumption of a constant ion mobility is thus justified except in the direct vicinity of the anode wire.

2.2.4 Gas amplification

Close to the wire the electric field strength becomes sufficiently large for the drifting electrons to gain enough kinetic energy to cause secondary ionization, as already mentioned. The gas amplification process follows the relation

$$dN = \alpha \cdot N \cdot ds\,; \tag{2.11}$$

the increase dN of electrons over a small drift distance ds is proportional to the number N of already existing electron-ion pairs. The factor α is known as first Townsend coefficient and depends strongly on the gas used, the electric field and the gas density ρ.
For drift tubes with a typical electric field E between 10^2 and 10^3 V/(cm·Torr) near the anode wire, an analytic formula for the gas gain G can be derived by making the assumption that α is proportional to E [40]. Doing so one finally arrives at the expression

$$G = \left[\frac{E(a)\cdot\rho_0}{E_{min}(\rho_0)\cdot\rho}\right]^{\frac{\ln 2\cdot a\cdot E(a)}{\Delta V}}\,, \tag{2.12}$$

or, substituting (2.1) for the electric field $E(a)$ at the anode wire surface,

$$G = \left[\frac{V}{a\cdot\ln\frac{b}{a}\cdot E_{min}(\rho_0)\cdot\frac{\rho}{\rho_0}}\right]^{\frac{\ln 2\cdot V}{\ln(b/a)\cdot\Delta V}}\,, \tag{2.13}$$

which is known as Diethorn formula. As in equation (2.1) a denotes the wire, b the tube radius and V the applied voltage. For a given gas the two constants ΔV and E_{min} must be obtained experimentally. E_{min} can be interpreted as the minimum electric field at a given gas density ρ_0 at which the gas amplification process sets in.
The Diethorn parameters for the Atlas MDT operating gas Ar:CO_2=93:7 were measured as

$$\Delta V = 34\,\text{V} \tag{2.14a}$$
$$E_{min} = 24\,\text{kV/cm} \tag{2.14b}$$

with an estimated accuracy of ±10% for a ρ_0 of 1 bar and a temperature of 25 °C [5].

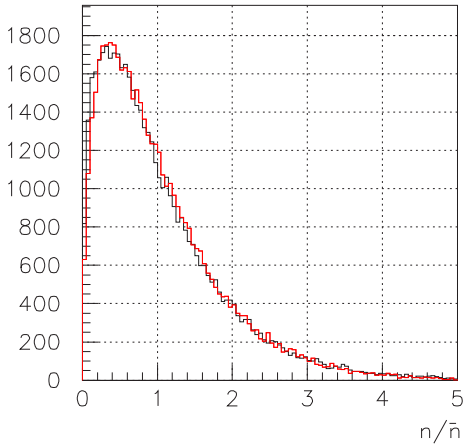

Figure 2.12:
Polya distributions for $\theta = 0.5$ (black) and $\theta = 0.38$ (red), describing the fluctuations in the gas amplification process for a single primary electron. The difference between the two choices of the parameter θ is negligible.

Gas gain fluctuations: In the same way as the Bethe-Bloch formula (2.2) gives merely the average energy loss of an ionizing particle, G in equations (2.12) and (2.13) describe the mean gas gain only. Fluctuations of G around its mean value $\bar{G}$ for a single primary electron are usually assumed to follow a Polya distribution [43],[6]

$$P(n) \sim \left(\frac{n}{\bar{n}}\right)^{\theta} \cdot e^{-(\theta+1)\cdot\frac{n}{\bar{n}}}, \qquad n \in \mathbb{N} \tag{2.15}$$

with $n \equiv G$, $\bar{n} \equiv \bar{G}$ and a value of the parameter θ of either 0.5 or 0.38. The difference between the two choices of θ is negligible, as can be seen from figure 2.12 which also gives an impression of the shape of the Polya distribution.

2.2.5 Signal formation

The charges q produced in the gas amplification process will generate an electric current I in the anode wire when moving in the electric drift field. If the anode is kept at a constant potential V then I can be calculated with the help of Ramo's theorem [27] as

$$I(t) = -\frac{q}{V} \cdot \vec{v}(t) \cdot \vec{E}(\vec{r}(t))\,. \tag{2.16}$$

(2.16) is a simple consequence of energy conservation, with the minus sign being convention.
For a drift tube with an electric field according to equation (2.1) it can be shown that the induced current signal is dominated by the ions drifting towards the tube wall. Substituting relation (2.10) for the ion velocity v_{ion}, one finally finds the expression

$$I(t) = -\frac{q}{2 \cdot \ln(b/a)} \cdot \frac{1}{t + t_0} \tag{2.17}$$

for the signal induced by a single ion cluster of charge q.
The way in which $I(t)$ transforms into the voltage signal $V(t)$ observed at the output of a drift tube depends strongly on the front end electronics. Appendix A discusses the technical details for the MDT case with the help of so-called system response functions; these will be used in sections 5.4 and 6.4 to include electronics effects in the simulation of the MDT behaviour.

2.3 Background environment at LHC

A large fraction of hits detected in the Atlas muon spectrometer will be due to background events rather than due to muons themselves. In this the LHC detectors differ significantly from past experiments like those at the Large Electron Positron Collider LEP, where rates in the muon systems were negligible.
In the MDT case the main background contributions are photon and neutron interactions. Neutrons typically stem from secondary particles produced in the beam pipe and other machine elements as well as in the calorimeters. Photons are to a large extent created by (n,γ)-reactions. Both neutrons and photons have in common that they are essentially uncorrelated to any primary interaction products due to the large number of scattering and (re)absorption processes involved in their creation [9].
Figure 2.13 shows simulation results for the expected photon flux in the Atlas muon spectrometer; photon rates are highest in the region close to the beam pipe, in particular in the two innermost endcap stations (EI, EM). The mechanisms by which a photon will deposit energy in an MDT were discussed in section 2.2.1; the interaction probability (efficiency) as well as the number of produced primary electrons depend on the photon energy (fig. 2.14). Combining simulation results for the expected photon energy spectrum with the γ-efficiency curve gives

$$\bar{N}_{p.e.} = 1235 \tag{2.18}$$

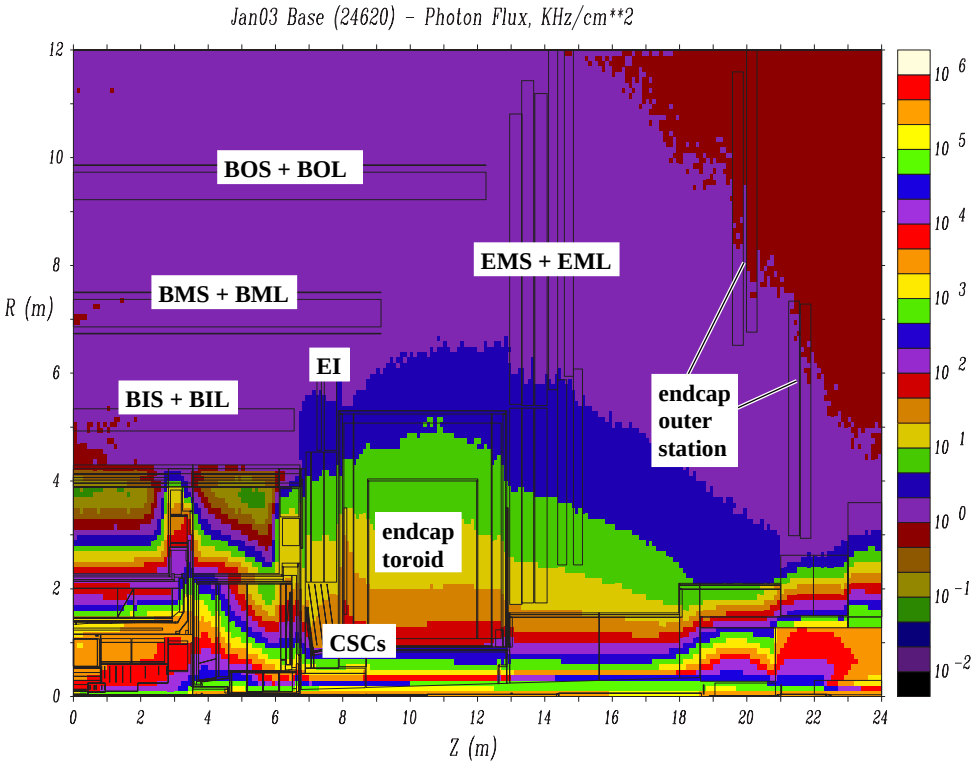

Figure 2.13: Expected photon flux in the Atlas muon spectrometer for a luminosity of $10^{34}\, s^{-1} cm^{-2}$ according to [17]. Photon rates are highest in the innermost part of the inner endcap station (EI).

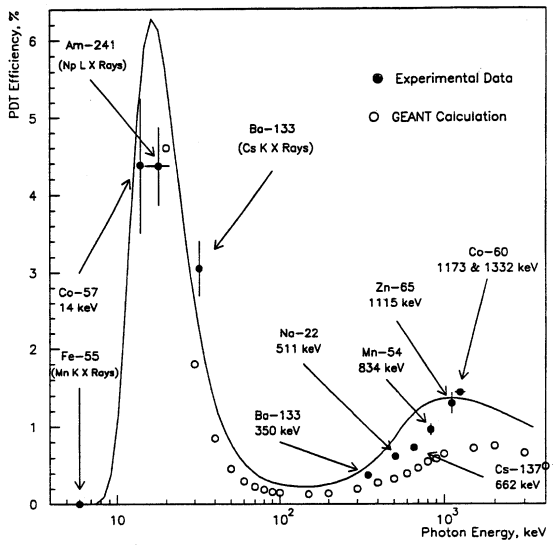

Figure 2.14:
Photon interaction probability (efficiency) in a single MDT [24].

for the average number of expected primary electrons per photon event [13], compared to about 750 primary electrons for a minimum ionizing muon. The average photon efficiency is approximately $5 \cdot 10^{-3}$.
MDT neutron detection probabilities are typically smaller by a factor 10, as has been verified experimentally both for thermal [29] and fast neutrons [2]. Thermal neutrons can activate atoms in the tube wall or the detector gas; the electrons emitted in the subsequent β-decay will ionize the MDT operating gas and thus lead to a detectable signal which in charge is similar to the one caused by a muon. Fast neutrons, whose flux is of the same order as the one for photons, react in a different way by transferring a fraction of their energy to a nucleus of the traversed gas in elastic scattering processes. The recoil nucleus will then lose its kinetic energy by atomic collisions and by ionization, where the latter will again lead to detectable MDT signals. Signals produced in this way can have a significantly larger charge than muon (or photon) pulses due to the high recoil energies possible for energetic neutrons and the small nuclei range.

2.3.1 MDT rate capability requirements

The sum of expected neutron, photon and charged particle count rates in the Atlas muon spectrometer is shown in figure 2.15. The highest rate, in the inner part of the EI station, is approximately $100\,\mathrm{Hz/cm^2}$. Based on these results the rate the MDTs must be able to sustain without significant degradation of their performance was defined as [13]

$$R_{max} = 5 \cdot 100\,\mathrm{Hz/cm^2} = 5 \cdot 300\,\mathrm{Hz/cm}\,. \tag{2.19}$$

The factor 5 with respect to the actual prediction was introduced to allow for uncertainties in the background simulations as well as for changes in the shielding design[3] and a potential luminosity upgrade in the future.
Formula (2.19) translates into a maximum accumulated charge of

$$Q_{max} = 5 \cdot 0.12\,\mathrm{C/cm} = 0.6\,\mathrm{C/cm} \tag{2.20}$$

[3] which was not frozen at the time of [13]

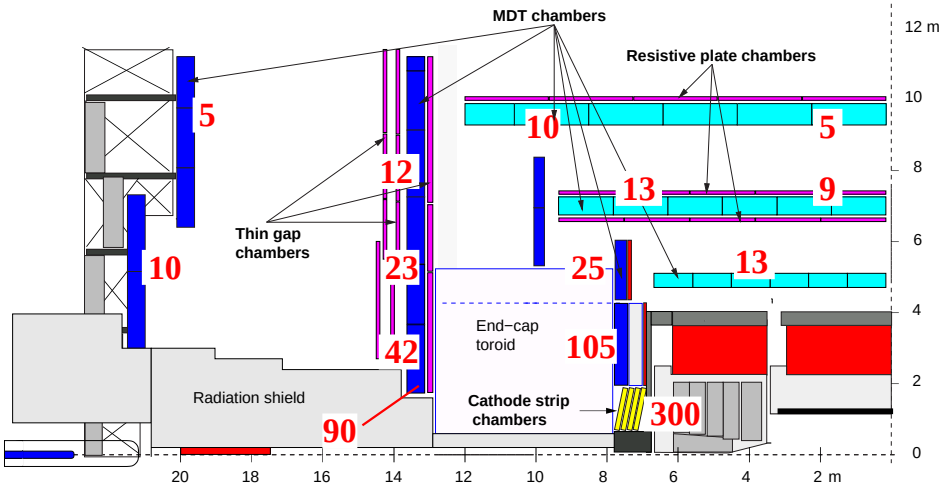

Figure 2.15: Approximate total MDT count rates in Hz/cm^2 for a luminosity of $10^{34}\, s^{-1} cm^{-2}$. The values shown are based on the latest background simulation [17], which takes into account photon, neutron, proton, muon, pion and electron contributions.

in 10 years of LHC operation (10^8 sec), assuming a gas gain of $2 \cdot 10^4$ and treating all background events as photons ($\bar{N}_{p.e.} = 1235$).
The safety factor 5 in formula (2.20) decreases if the larger pulse charge of neutrons is correctly included. Calculations carried out by P. Nevski et al. [55] for the innermost EI MDT chambers[4] indicate that even though the count rate due to fast neutrons ($E_n >$ 100 keV) is 10 times smaller than the count rate due to photons, the energy deposited by ionization is almost equal ($\int E_n^{ion} / \int E_\gamma^{ion} = 1.2$) for the two types of interaction. As a consequence the safety margin in (2.20) is 2.5 instead of 5, which has to be kept in mind particularly when discussing ageing results.

[4] position z = 720 cm, r = 270 cm in fig. 2.13

'Everything should be made as simple as possible, but not one bit simpler.'
Albert Einstein, 1879 – 1955

Chapter 3

Experimental setup

This chapter gives details on the experimental setup(s) used for the high rate and ageing studies; all data was taken at the CERN Gamma Irradiation Facility GIF, using both cosmic and test beam muons to evaluate the MDT performance. The different run periods are listed in section 3.1, while 3.2 gives an overview over the main features of GIF. The MDT chamber utilized for all measurements is described in paragraphs 3.3 (mechanics) and 3.4 (on-chamber gas system).
The setup included a scintillator hodoscope in those phases in which data was acquired from cosmics. The hodoscope was used to provide a trigger signal and for a crude reconstruction of muon tracks; details on the scintillator system are given in section 3.5. Paragraph 3.6 discusses the MDT front end electronics; the data acquisition and readout chain is also addressed. Building on what is said in sections 3.2 to 3.5 , 3.7 summarizes the different mechanical configurations during the various data taking phases, while 3.8 introduces naming conventions and several coordinate system definitions which were used in the analysis and will be needed in chapters 4 and 6. The chapter closes with a detailed description of the off-chamber gas system, with particular emphasis on the portion providing gas recirculation to half of the drift tubes studied. Experiences with operating the circulation system, whose construction and design was an important part of this thesis, are also reported.

3.1 Data taking periods

The data presented and analysed in this thesis was taken between November 2001 and May 2003 with several interruptions. The setup had to be modified repeatedly due to changing operating conditions at the Gamma Irradiation Facility and space constraints imposed by other users. The measurement program carried out can be grouped into the following periods:

1. Ageing period 'Age1' – 15/3/02 to 10/5/02.
2. Test beam period – 27/5/02 to 7/6/02.
3. Ageing period 'Age2' – 27/9/02 to 8/5/03.

Period 'Age1' was preceded by a 2-month commissioning phase in Nov./Dec. 2001 and by two months of data taking (5/1/02 to 15/3/02) without irradiation[1]. The test beam period

[1]Use of the γ-source was not possible in this period due to rebuilding of the GIF gas zone.

was dedicated to studying MDT performance under Atlas-like background conditions with the help of 100 GeV muons from CERN's SPS accelerator complex.

3.2 Gamma Irradiation Facility GIF

The Gamma Irradiation Facility GIF (fig. 3.1) is a dedicated experimental zone located in the West Area at CERN; it was specifically built to allow for large area (photon) irradiation tests of detectors for the LHC experiments. Chambers, with a size up to $6\times4\,m^2$, are irradiated by an intense radioactive ^{137}Cs-source (740 GBq initial activity) with photons of 660 keV energy. A set of movable lead filters in front of the source can be used to adjust the photon flux over a range of several orders of magnitude. The γ-fluence emitted by the point source is initially uniform over a spherical surface; a specially shaped lead absorber installed at the source aperture provides for uniform rates over a planar surface more suited to studies of usually flat detectors. Part of the initial photon flux is scattered on the floor and in the filters; the consequence is a contribution of photons with $E_\gamma < 660$ keV to the spectrum 'seen' by the chambers under investigation [1].
Being situated in the West Area of CERN's SPS complex, during accelerator operation a weak muon beam can be extracted to the GIF zone via the X5 beam line. This makes it possible to study the performance of muon detectors under realistic LHC conditions by exposing them to intense levels of background irradiation from the ^{137}Cs-source while simultaneously attempting to reconstruct beam muons.

3.3 The MDT chamber BIS 'Beatrice'

An Atlas MDT chamber, named 'Beatrice', of type BIS (Barrel Inner Small) was used in the studies presented here. BIS chambers consist of 240 MDTs which are arranged in two

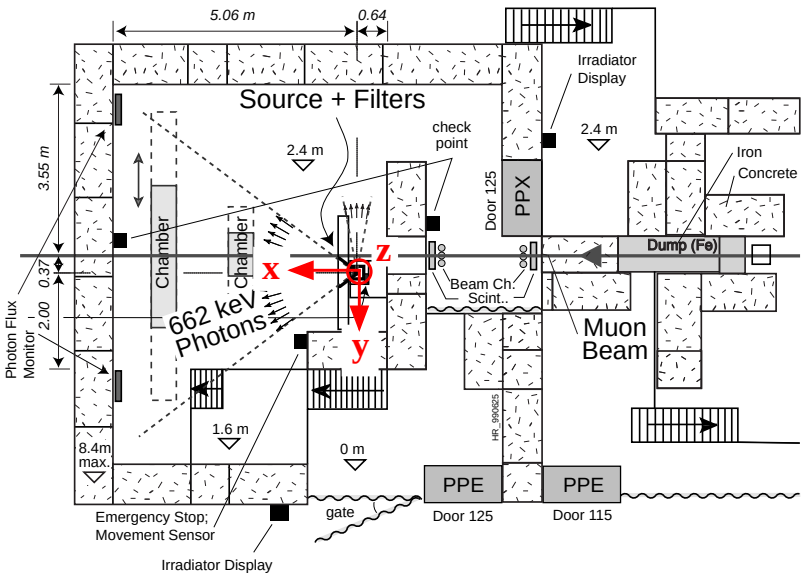

Figure 3.1: Layout of the Gamma Irradiation Facility GIF at CERN. The coordinate definition shown in red is described in section 3.8.

multilayers of 4×30 tubes each. The tube length is 170 cm, the distance between the two multilayers is 6 mm. 'Beatrice' is the first series production chamber (module-0) built by the Aristotle University in Thessaloniki [65], which is responsible for the construction of a total of 128 BIS chambers.
All materials and MDT components used for the module-0, as well as the assembly procedures, were identical to the final Atlas ones, with the exception of the front end electronics (section 3.6), the material of the on-chamber gas distribution and the Faraday cage. 4 metal bars glued to the surface of one multilayer hold 3 kinematic mount blocks in which the chamber is supported when installed in the Atlas detector or a test setup. Gas to the individual MDTs is supplied by 4 manifolds; these are oriented perpendicular to the tubes at each chamber end (fig. 3.2).

3.4 On-chamber gas system

For chambers of type BIS the gas supply to the individual drift tubes is fully parallel; each MDT is separately supplied with gas from the manifolds described in the previous section. One of the foremost requirements in designing the gas distribution system was to avoid the use of glue, adhesive sealant compounds and soft plastics. The former two harbour the risk of causing chamber ageing, especially when not properly cured; soft plastics like polyamide (Rilsan® hoses etc.) on the other hand are often permeable to H_2O molecules and lead to an uncontrolled water content in the gas.
The chosen design relies on O-ring joints for leak tightness. Tubes are connected to the chamber gas manifolds with the help of metal tubelets (fig. 3.3). Each tubelet ends in a plastic 'jumper' which fits over the outside part of the brass insert of the MDT endplugs.

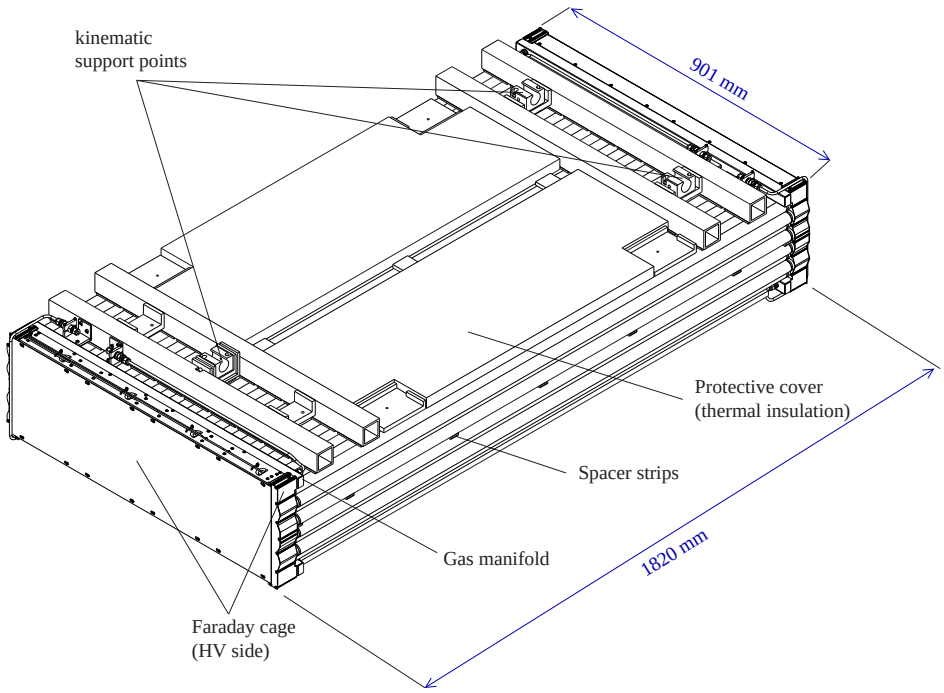

Figure 3.2: 3D model of a BIS MDT chamber.

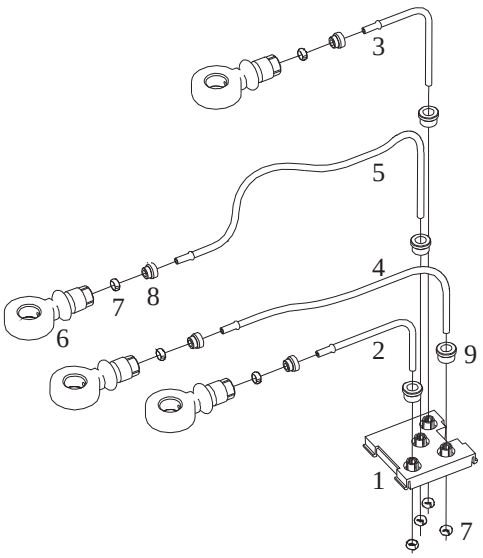

Figure 3.3:
Gas connection for a group of 4 MDTs. The rectangular plate (1) snaps onto the gas manifold bar glued to the chamber. Each tube is supplied with gas via small diameter metal tubelets (2-5). The jumper (6) fits over the central brass insert of the MDT endplugs with gas reaching the tube interior through a hole in the insert (fig. 2.2).
The inner diameter R of the tubelets is matched to their respective length l such that the product R^4/l is constant. This is necessary to ensure equal gas flow in all MDTs.

A brass cap (signal cap, not shown) screws onto the insert and fixates the jumper with O-rings between cap and jumper and jumper and endplug body providing gas tightness. Materials in contact with the gas are Pocan[2] (jumpers), EPDM[3] (O-rings) and brass or stainless steel[4].

Leak rates

The Atlas specification for the maximum permitted leak rate at 3 bar absolute pressure is 10^{-5} mbar·l/s for a bare MDT and twice as much when the gas connections are included. For the two BIS multilayers with a volume of 150 l each this corresponds to a pressure drop of 1.4 mbar/day. Measured leak rates for BIS Beatrice were slightly higher (9.2 mbar/day for both multilayers together), but no single big leak could be found.

3.5 Scintillator trigger hodoscope

During the periods 'Age1' and 'Age2' weekly reference runs with cosmic muons were taken to monitor the chamber performance. A scintillator hodoscope, consisting of 24 plastic scintillators, was used for triggering in this case. The trigger signal served as start signal for the measurement of the muon drift time and generated the gate for an integration of the pulse charge; the latter was used to check for any evidence of ageing, as will be pointed out in 3.6.4.
The hodoscope scintillators were arranged in two double layers (fig. 3.4) with an active area of $100 \times 105\,\mathrm{cm}^2$. Top and bottom plane of each double layer were shifted by half a scintillator strip width with respect to each other to achieve better granularity in the direction perpendicular to the strips; they were read out to opposite sides, which made it possible to reconstruct the muon track position with the help of TDCs recording the

[2]Pocan®: polybutylenterephthalate, by Bayer Polymers
[3]EPDM: Polymerized ethylene propylene diene monomers
[4]The tubelet material was changed from brass to stainless steel in 2003 after problems with corrosion; brass tubelets were used in the work presented here.

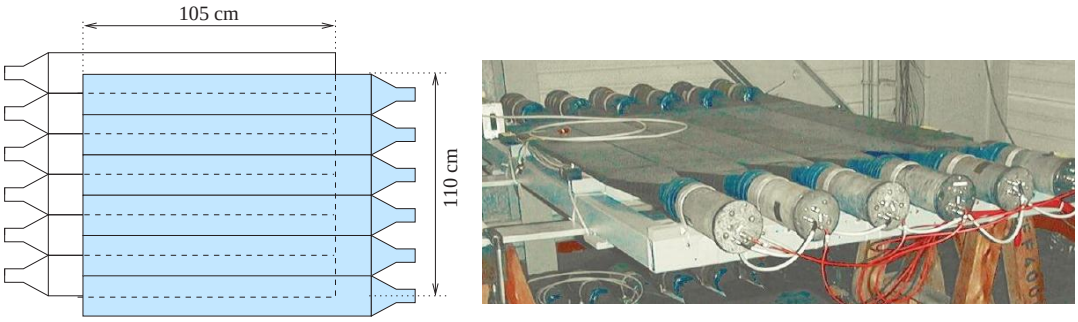

Figure 3.4: Scintillator trigger hodoscope. Only one of the two double layers is shown. Each of the scintillators is connected to a photo tube at one end; the orientation is such that the top 6 scintillators are read out to one side, the bottom 6 to the opposite side.

individual scintillator signals, as described below. For all scintillators the photo tube signal was converted into a fast NIM pulse by a constant fraction discriminator to achieve a good time resolution.

Trigger logic

To generate a trigger signal a coincidence of hits in all four scintillator planes was required. Figure 3.5 shows a schematic of the trigger logic. The digital signals from scintillators in each layer were connected to a Fan In/Fan Out module which provided their logic OR; the output signals for the two top layers and the two bottom layers respectively were then fed to a mean timer. The two mean timer outputs formed the input of the coincidence unit used to generate the final trigger signal. Input pulses to the coincidence unit were stretched to 20 ns by a discriminator module; an additional delay of 10 ns in the signal path of the bottom hodoscope layers guaranteed that the coincidence signal was always 'triggered' by the bottom scintillators. The coincidence signal was also used as common start for 24 TDCs LeCroy 2228, which were read out via Camac. The TDCs recorded the time between the arrival of the trigger signal and the individual scintillator signals which were delayed by 100 ns. The timing information was used to reconstruct the muon hit position along the scintillators according to the method described in appendix B.
The system was operated in single-event mode by blocking the generation of further trigger signals during the time needed to read out an event; this was achieved using the veto input of the coincidence unit together with a Camac accessible flip-flop (Status-A module). A 'Busy' signal was set by the trigger signal and reset by the data acquisition after reading out the event had finished.

3.6 MDT electronics and readout; data acquisition

3.6.1 Passive front end electronics

Passive printed circuit boards, also known as hedgehog boards, are attached to the BIS chamber at each end (fig.3.6). Each board provides connections to a group of 24 MDTs. Tubes are supplied with high voltage at one end with the signal being read out at the other end after decoupling the high voltage with a capacitor.

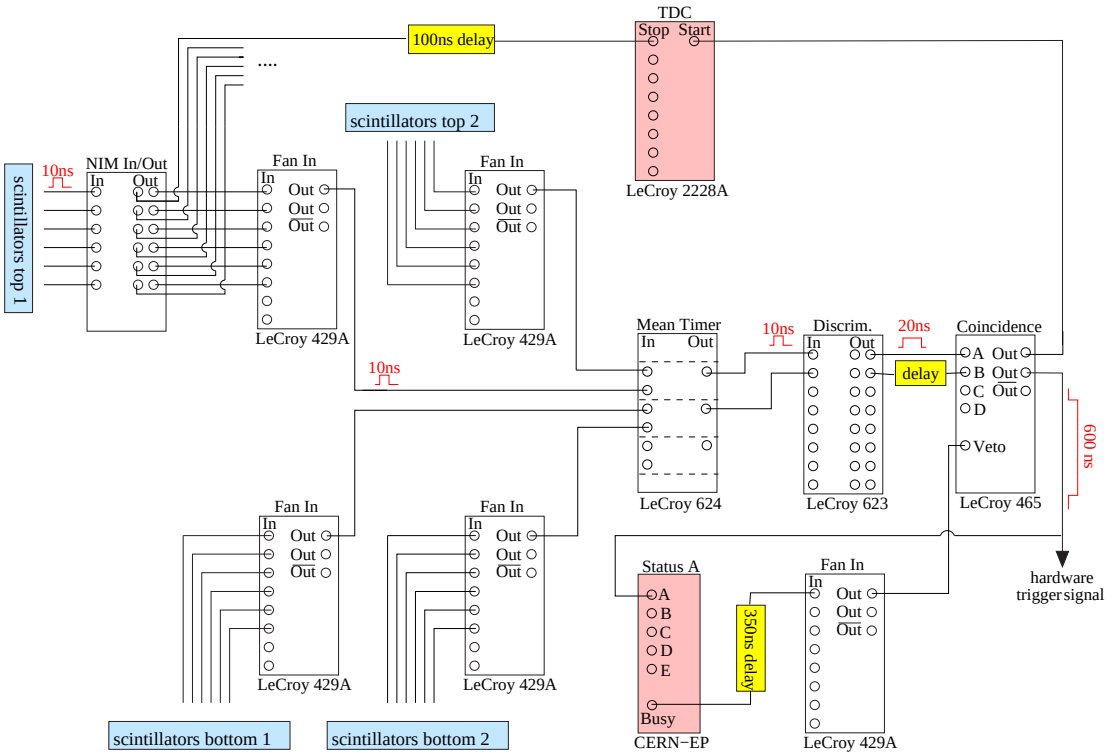

Figure 3.5: Schematic of the trigger logic. A coincidence of hits in all four hodoscope layers is required to form a trigger signal. The time between the arrival of the individual scintillator signals and the trigger signal is measured by Camac TDCs (LeCroy 2228).

3.6.2 Active front end electronics

Pulses generated in the MDTs by traversing particles are fed to an amplifier-shaper-discriminator (ASD) combination which together with the Atlas Muon TDC AMT for drift time measurements constitutes the active part of the front end electronics. Both ASD and AMT are located on a separate printed circuit board (mezzanine card) which plugs onto the readout hedgehog. Each mezzanine can handle the signals of 24 tubes using a single AMT and either 8 (prototype version ASD-lite) or 3 (final version) ASD chips. ASD-lites and the pre-production TDC version AMT-1 were used in this thesis.

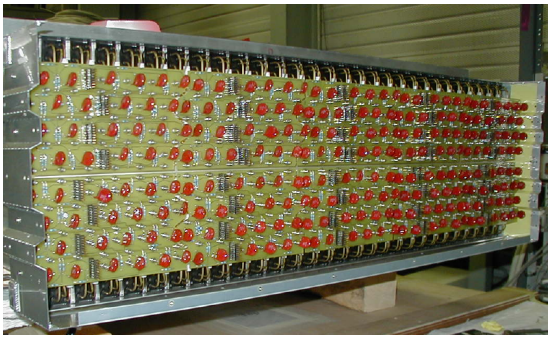

Figure 3.6: MDT passive front end electronics. The photograph shows the BIS chamber from the readout side. The rectangular connectors visible allow for plugging the active part of the front end electronics (mezzanine cards).

ASD: The design of the amplifier-shaper-discriminator chain [61] is differential as rejection against common mode pickup noise. The discriminator threshold can be adjusted, for the ASD-lite either with the help of a potentiometer on the mezzanine or by using an on-board DAC which can be programmed from the data acquisition. If not stated otherwise, a threshold of 60 mV was used. The dead time for the ASD-lite is small (<100 ns); a typical muon signal as the one shown in figure 2.5 therefore produces multiple threshold crossings and thus several hits in the event data. Only the first hit contains information about the drift radius of the muon trajectory; all later hits are discarded during offline analysis.

AMT: One of the main requirements in designing the Atlas Muon TDC [7],[8] was the capability to record closely spaced pulses without introducing any dead time. Together with the high rates expected at LHC, this necessitates that the AMT is able to continuously accept new hits while selectively extracting temporarily stored hits belonging to a given trigger once the trigger signal is generated. Several levels of data buffering are used for this purpose, as can be seen from figure 3.7. The arrival time of each hit is first recorded in a level-1 buffer. Time data is stored as two numbers which are commonly referred to as coarse and fine time counts. The coarse time measurement comes from a 40 MHz counter running synchronously to the LHC bunch crossing frequency, while a phase locked loop

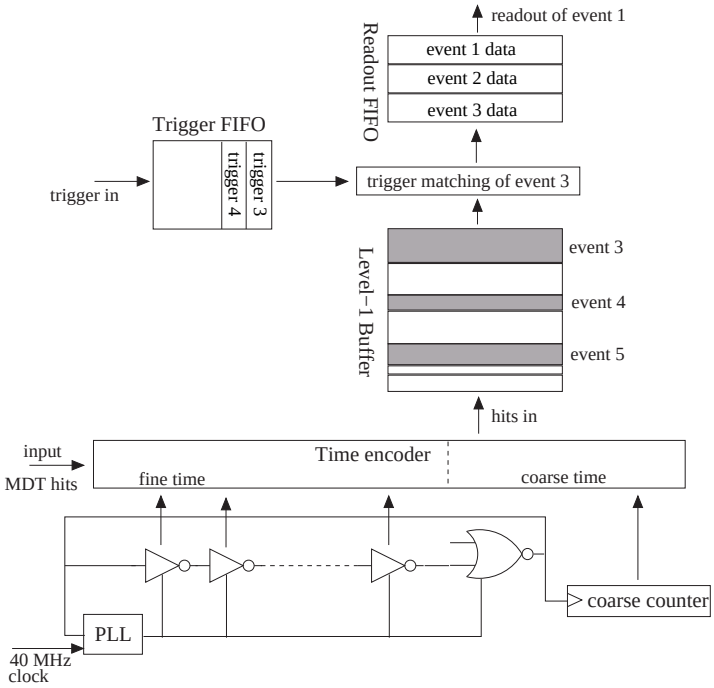

Figure 3.7: Architecture of the AMT (simplified). Several data buffers are used to avoid introducing dead time while an event is being processed. All logic runs at 40 MHz, synchronous to the LHC bunch crossing frequency. The time between the arrival of a trigger signal and an MDT hit is stored as a pair of numbers, commonly referred to as coarse and fine time counts. The coarse time comes directly from a clock-synchronous counter, while a phase locked loop (PLL) gate chain with a well-defined delay between the individual gates is used to obtain the fine time measurement.

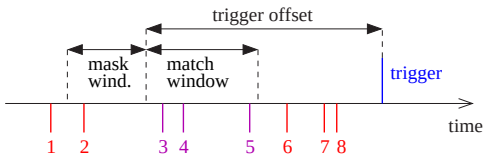

Figure 3.8:
AMT trigger matching. In the example shown hits 3,4 and 5 would be selected by the matching algorithm. The mask flag would be set due to the presence of hit 2.

(PLL) chain of CMOS gates is used to obtain a fine time measurement within the clock cycle. The total time resolution is 0.78 ns.
Trigger signals are stored in a dedicated trigger FIFO. A matching algorithm associates data from the level-1 buffer with a given trigger and transfers the corresponding hits to the AMT readout buffer. Hits are selected if they fall into a time window (match window) of a given length, which starts a certain number of clock ticks (trigger offset) prior to arrival of the trigger signal (fig. 3.8). A mask window can be programmed to precede the match window. If for a given MDT hits are found by the trigger matching algorithm both in the mask and the match window, a special flag is generated in the event data. This flag makes it possible during offline analysis to spot events for which the drift time, and consequently the drift radius measurement is potentially masked by secondary threshold crossings of an earlier muon pulse. Data presented in this thesis was taken with a match window of 1 μs and a mask window of 500 ns, if not stated otherwise.

3.6.3 Event building

Data from the individual mezzanine cards is transmitted as LVDS[5] signal to the so-called Chamber Service Module CSM, which in its stand-alone version CSM-0 resides in a VME crate [37]. The CSM-0 has to

1. generate a 40 MHz clock signal and send it to the mezzanine cards,
2. handle trigger signals and distribute them to the AMTs,
3. combine data from the individual AMTs into a single event and add information on the event size, event number etc. to it (event building),
4. provide a way to set or change the programmable configuration of each mezzanine card (ASD threshold, trigger matching parameters,...),
5. allow for control and readout via VME.

Figure 3.9 shows the connections between CSM-0 and front end electronics as well as all other off-chamber electronics elements. Power to the mezzanine cards is supplied by a module known as CSM adapter; two separate power supplies are used to feed the analogue (ASD) and digital (AMT) part of the circuitry. The AMT configuration and the ASD threshold can be changed by sending a special bitstream via JTAG[6]. A JTAG interface is part of the CSM-0.
The coincidence signal from the hodoscope is used as trigger signal. Alternatively pulses from a timing unit can be used (so-called 'random' trigger). This option, in which the

[5] Low Voltage Differential Swing, a method of digital signal transmission which minimizes noise emission
[6] Joint Test Action Group, IEEE standard 1149.1, a protocol used for in situ testing of digital circuits and access to their registers

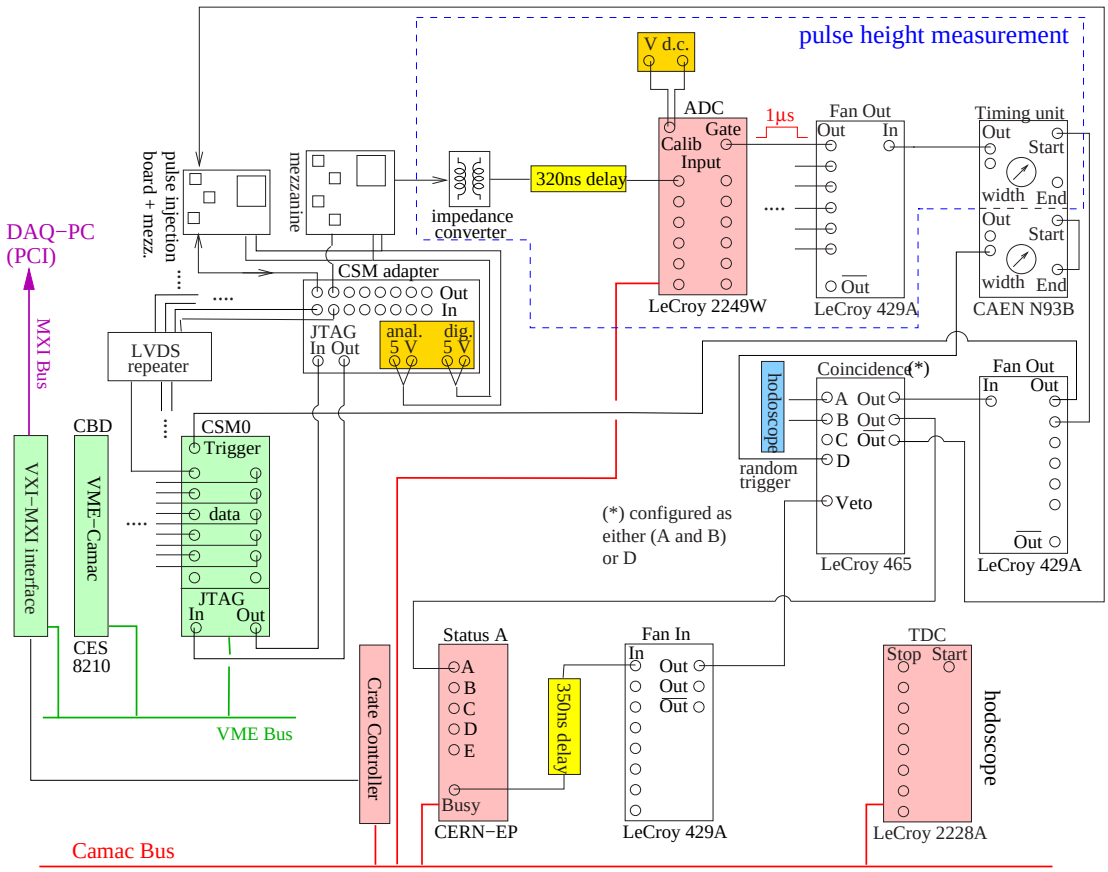

Figure 3.9: Off-chamber electronics and readout system. Modules shown in red are read via Camac, modules shown in green via VME. The complete system was interfaced to the PC running the data acquisition by an MXI-2 bus from National Instruments. For the setup at GIF, the distance between the front end electronics located on the BIS chamber and the racks housing all Camac and VME modules was approximately 25 m; LVDS repeaters had to be used to ensure reliable communication between the mezzanine cards and the CSM-0.

trigger is not correlated to the passage of particles, is used for noise and γ-rate measurements (section 4.1). The CSM-0 relays a received trigger signal to the AMT only with the next rising edge of its internal 40 MHz clock. Without a correction this introduces a 25 ns uncertainty into all drift time measurements. This situation can be remedied if the trigger signal is additionally injected into a separate mezzanine channel; the measured 'drift' time of this channel is then subtracted from all other time data.

3.6.4 Pulse height readout

For ageing studies a monitoring of the MDT gain and thus the measurement of pulse heights is essential. While the final Atlas ASD will include an on-board ADC for this purpose, this option is not available for the prototype ASD-lite used in the work presented here. Since on the other hand the analogue output signal, taken after the shaper, is available for every third channel, it was decided to perform the pulse height measurement with external, charge integrating Camac ADCs LeCroy 2249W. The originally 100 Ω

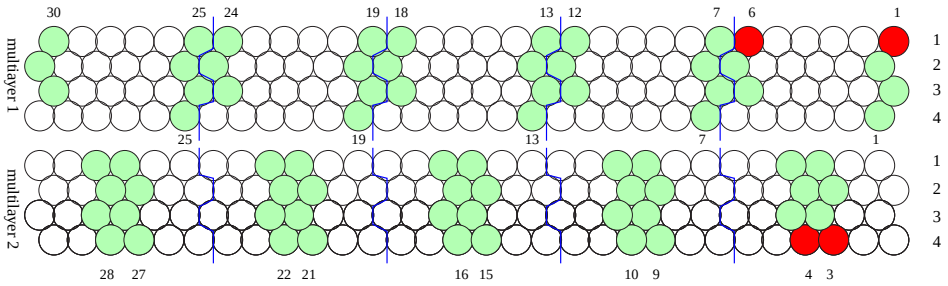

Figure 3.10: Position of tubes for which a pulse height measurement was performed, seen from the readout side of the chamber. The first 6 tubes each in multilayer 1, layer 1 and multilayer 2, layer 4, were disconnected from HV during γ-irradiation to serve as a reference.

differential signal was converted to a single ended 50 Ω pulse by an impedance converter (pulse transformer). The gate length was set to 1 μs to allow for integration of the complete muon signal. Figure 3.10 shows for which MDTs a pulse height measurement was performed. In total 12 MDTs, 6 in each multilayer, were disconnected from high voltage during γ-irradiation. They served as a reference in order to help disentangle changes in the observed gas gain due to temperature effects etc. from a real gain reduction due to chamber ageing.
The conversion constant between integrated charge and ADC counts can vary from channel to channel. The LeCroy ADC 2249W has a mode in which these constants can be calibrated by supplying different d.c. voltage levels to a special calibration input, as shown in figure 3.9. A calibration was performed at regular intervals and after each change in the channel assignment.

3.6.5 Data acquisition

The data acquisition software used is based on the MiniDAQ package [22] developed at the University of Michigan, which was adapted for the studies carried out in this thesis. All code was written in the LabWindows/CVI framework from National Instruments and running under Windows 95[7]. Data was stored in a binary format described in appendix D.

[7] Windows 2000 since Feb. 2003

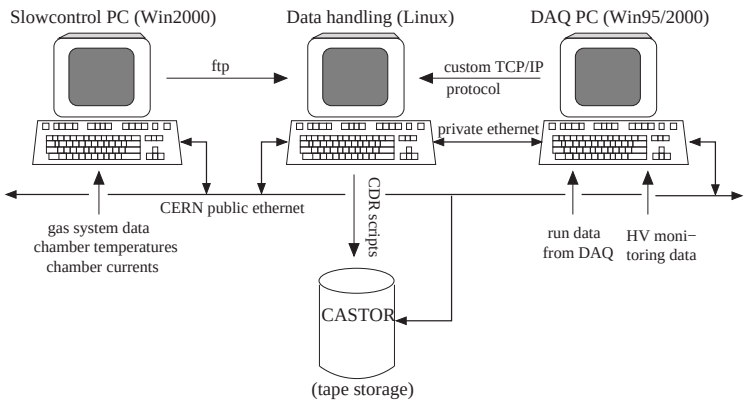

Figure 3.11: Connection between data acquisition, gas system slow-control and tape storage. A private ethernet link was used to transfer data during a run to a PC running Linux for analysis. All data was archived on tape as backup.

A TCP/IP interface was developed to transmit data during a run via a private ethernet connection to a second PC running Linux for a first analysis (fig. 3.11). All data, including the one originating from monitoring the gas recirculation system described in section 3.9, was automatically copied to CERN's tape storage system CASTOR[8].

3.7 Mechanical setup during the different run periods

As already mentioned, the geometric and mechanical configuration used for the studies presented in this thesis had to be modified several times. The original layout, used during period 'Age1', is shown in figure 3.12. The MDT chamber was mounted with an inclination of $\approx 45°$ with respect to the vertical direction. This position guarenteed an adequate exposure both to photons from the GIF radioactive source and to cosmic muons for the monitoring runs. The gas inlet to the chamber was at the end closer to the floor (readout side), the gas outlet at the opposite end (HV side).
The two hodoscope double layers were installed horizontally; the distance between them was chosen such that the upper scintillator plane was outside the (direct) γ-irradiation of the ^{137}Cs-source. The lower plane was shielded by 5 cm of lead against photon hits. The

[8] CERN Advanced Storage

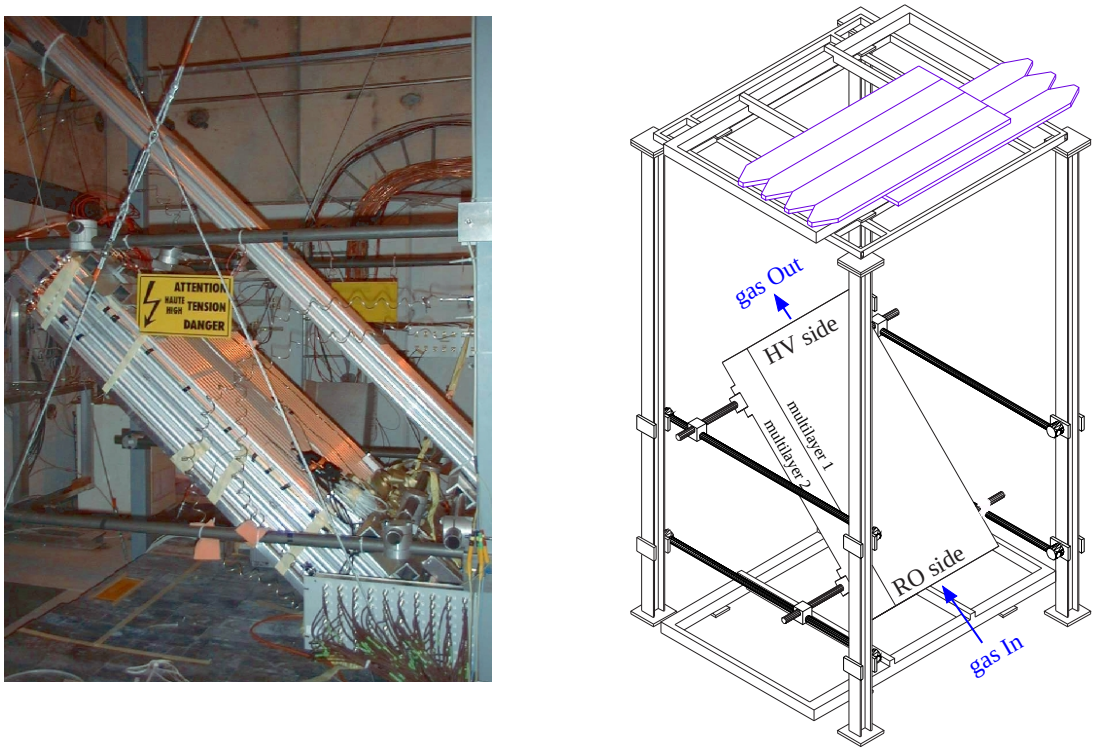

Figure 3.12: Layout and mechanical setup during period 'Age1'. Both hodoscope double layers were mounted horizontally while the BIS chamber had an inclination of $\approx 45°$ to ensure adequate exposure both to cosmic muons and to photons from the GIF radioactive source. The hodoscope scintillator strips were oriented perpendicular to the MDT wire direction. The long MDTs visible in the photograph above the BIS chamber belonged to a different study, which will not be discussed in this thesis.

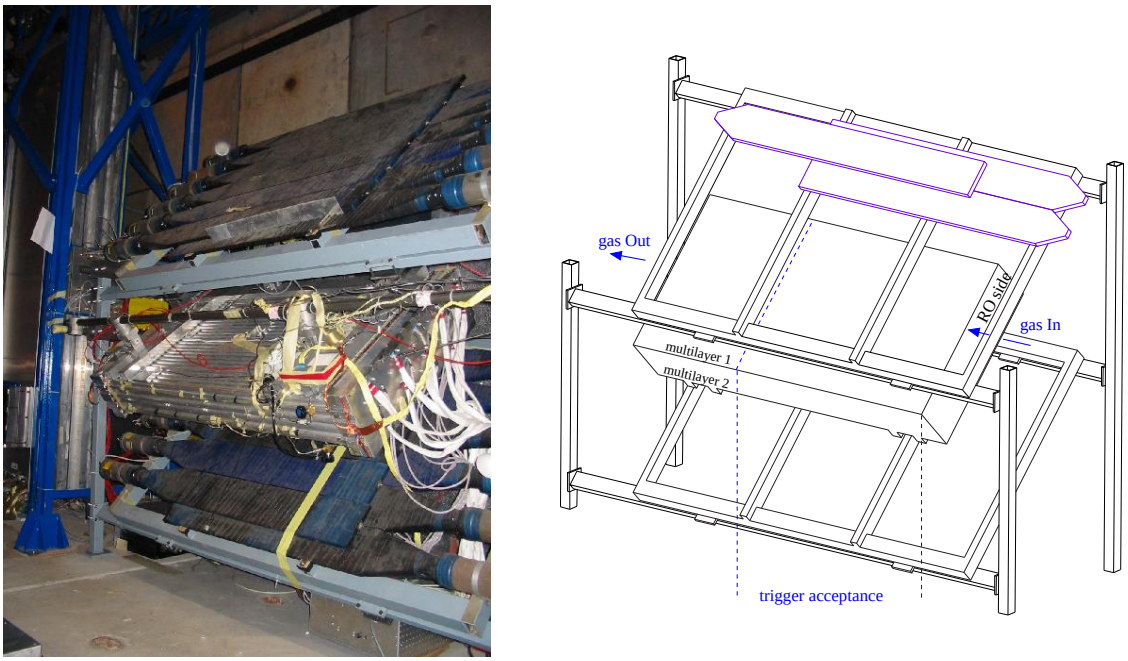

Figure 3.13: Layout and mechanical setup during period 'Age2'. MDT wires and hodoscope scintillator strips were parallel to each other. Only 2/3 of the MDT chamber was within the trigger acceptance; the pulse height could therefore only be monitored for the first 105 cm, measured from the MDT readout side.

scintillator strips were oriented perpendicular to the MDT axis; the position of a muon track along the tube wires could be determined directly from the pattern of scintillators which showed a signal. The trigger acceptance covered the complete BIS chamber with the exception of the first 30 cm, measured from the readout side, of multilayer 1.
During period 'Age2' the setup was compressed in size (fig. 3.13). The BIS chamber was mounted such that the wires were horizontal; the hodoscope was arranged in such a way that the scintillator strips were parallel to the MDT axis. This made it necessary to use

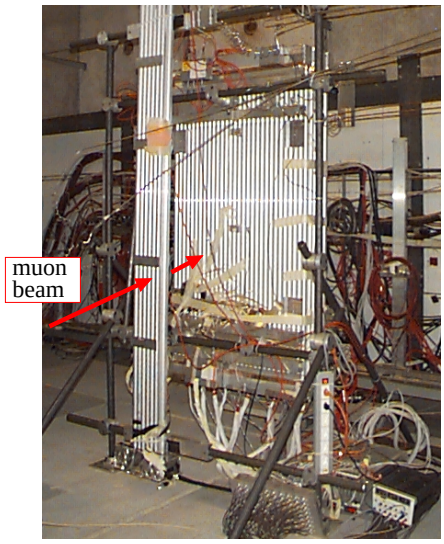

Figure 3.14:
Setup during test beam data taking. A set of scintillators centered on the muon beam line (not shown) was used for triggering instead of the hodoscope. The 'bundle' of MDTs mounted in front of the BIS chamber belonged to a different study not part of this thesis.

timing information from the hodoscope TDCs to reconstruct the position of muon tracks along the tubes. The distance between the two hodoscope planes was greatly reduced and all shielding was removed. The BIS gas inlet remained on the readout side of the chamber. The pulse height could be monitored with muons only for the first 105 cm, measured from the readout side, since the remaining part of the chamber was outside the hodoscope trigger acceptance.
During data taking with the X5 muon beam in summer 2002 (testbeam period) the BIS chamber was mounted with the MDT wires in a vertical orientation (fig. 3.14). In this way having to compensate for a gravitational wire sag in the offline analysis was avoided. The hodososcope was removed from the setup; a set of three plastic scintillators with an overlap of $16 \times 16\,\mathrm{cm}^2$ was used as beam trigger instead.

3.8 Coordinate systems and naming conventions

This paragraph introduces a set of coordinate definitions and labelling schemes which will be used in later sections to refer to individual tubes and when discussing track fitting.

Global and local coordinates

The basic geometry objects for track reconstruction in the given setup are the two BIS multilayers and, for the ageing runs, the two hodoscope (double) planes. For each of these subdetectors a local cartesian coordinate system is defined which is best adapted to the respective geometry. In addition a global coordinate system is used when the relative orientation of the different elements is needed. The **global coordinate system** origin coincides with the center of the radioactive ^{137}Cs source of GIF; the z-axis is vertical, the x-axis runs in the direction of, the y-axis perpendicular to the muon beam (fig. 3.1).
For the **local BIS coordinate system** the convention is such that the positive x-axis is pointing from the HV side to the readout side, along the wire direction. Both y- and z-axis are oriented perpendicular to the tube axis, with the z-direction parallel to the tube layers. y is increasing in flight direction of a traversing particle (fig. 3.15, left part). The coordinate origin is the center of mass of each multilayer.
In **hodoscope local coordinates** y is perpendicular to the scintillator plane, with values again increasing in flight direction of a traversing muon. x is oriented along the scintillator strips, z under 90° with respect to them (fig. 3.15, right part).

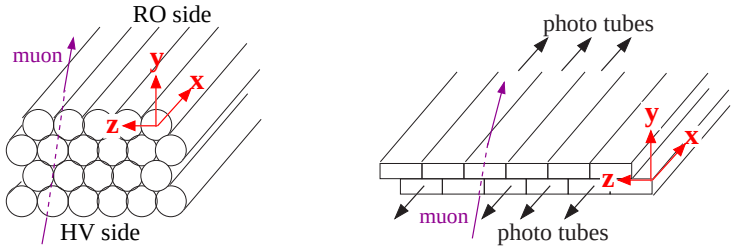

Figure 3.15: Local coordinate systems for the BIS multilayers (left) and each of the hodoscope planes (right).

Naming conventions

Elements of the BIS chamber referred to in the analysis are individual tubes, tube layers and multilayers. Multilayers are numbered starting from 1 in the direction of traversing muons (local y-direction); the same convention is used for tube layers within each multilayer. Single MDTs are identified by a five digit tube number, which is defined as

$$tube\_ID = x\,y\,z\,aa\,; \tag{3.1}$$

x is the chamber number (1 in the case of a single chamber only), $y = 1, 2$ the multilayer, $z = 1..4$ the layer and $aa = 1..30$ the tube number within a given layer. aa increases in positive z-direction of the local coordinate system.

3.9 Off-chamber gas system and gas recirculation

With a total active volume of roughly $800\,\mathrm{m}^3$ the Atlas MDT system is one of the largest gaseous detectors ever built. Although the operating mixture Ar:CO_2=93:7 is made of fairly inexpensive and inert standard gases, financial constraints still limit the amount of gas which can be replaced in a given time. A certain gas exchange with at least a limited fresh gas injection is necessary to compensate for leaks and to prevent impurities from building up in the system. Impurities can come from materials in contact with the gas (outgassing) and from leaks (back diffusion of air); they can also be produced by chemical reactions associated with the gas amplification process.
Table 3.1 summarizes the specifications of the MDT gas system (at Atlas). The daily gas refreshing rate is 10% of the total detector volume. The gas circulation through the MDTs will be higher by a factor 10, i.e. 1 volume/day; in this way radiation induced impurities, which will mainly be formed in the innermost stations of the muon spectrometer, are diluted. The same holds for air contamination, should there be a few leaks significantly larger than the rest. A purification stage, filtering out oxygen and possibly water, might be added to the circulation loop to stabilize the gas mixture. As for the drift tube components themselves, a careful selection of any material in contact with the gas as well as the elimination of lubricants wherever possible are essential in order to limit the risk of chamber ageing caused by a pollutant.
Evaluating the long-term operation of MDTs under gas recirculation in an environment similar to the later Atlas one was the main goal of this thesis, in addition to studying the MDT high rate behaviour. The circulation prototype system utilized will therefore be discussed in more detail in the remainder of this section. 3.9.1 summarizes the main features of the so-called Argon Turbo Circulator, the core component of both the final Atlas and the prototype gas recycling setup; paragraph 3.9.2 describes the rest of the system and discusses different modes of operation. 3.9.3 is dedicated to the control software and to special safety interlocks. Section 3.9.4 finally discusses results on the long-term stability and reliability of the gas system as well as particular difficulties encountered. Results pertaining to chamber ageing are discussed in chapter 6.

3.9.1 The gas circulator ATC

Any recirculation system has to include a compressor to pump the gas and to compensate for the pressure drop in the gas returning from the previous pass through the detector,

Parameter	Value
Total gas volume:	$754\,\mathrm{m}^3$
Operating pressure:	3.0 bar abs.
Gas composition:	Ar 93 ± 0.25 %, CO_2 7 ± 0.25 %
Number of chambers:	682 (barrel) + 512 (end cap)
Number of gas channels:	112 (barrel) + 162 (end cap)
Gas circulation:	1 volume/day (100 Nm^3/h)
Refreshing rate:	10% of total volume/day
Total leak rate:	$\lesssim 0.1$ Nm^3/h (incl. MDTs)
Impurities:	≤ 100 ppm O_2
Water content[9]:	500 - 1000 ppm, value to be defined
Purification:	to be decided (O_2, H_2O)
Materials in contact with the gas:	Al, stainless steel, copper, brass, Noryl, Pocan, EPDM, Viton, ... **— avoid any lubrication —**

Table 3.1: Atlas MDT gas system specification [45],[18].

which is envisaged to be around 300 mbar for the MDT part of the Atlas muon spectrometer. The choices for a suitable compressor are severely limited due to the high Atlas flow rate ($100\,\mathrm{Nm}^3$/h) and the requirement of a lubricant-free design. A high-speed gas turbine was eventually agreed on. The turbine technology combines long maintenance intervals with essentially no pressure fluctuations at the output and is thus superior to diaphragm pumps which are the classical alternative for lubricant-free applications. The selected turbine, running at up to 55000 rpm, was custom-designed for Atlas by the Czech company Ateko[10]; it is commonly referred to as Argon Turbo Circulator or ATC (fig. 3.16).
No lubrication is used anywhere in the ATC. Materials in contact with the gas are limited to steel, aluminium, graphite and a few Viton O-rings. During operation the rotor shaft with the turbine blade wheel is supported by three dynamic gas bearings (2 radial, 1 axial). With their special geometry they ensure that the rotor 'floats' on a cushion of the pumped gas itself without direct contact to the bearings once a rotation speed of more than 4000 rpm is reached. Mechanical bearings made out of electro-graphite[11] serve as backup and support the rotor during the run up and run down phase.
The turbine is driven by an electrical 3-phase induction motor. The coils of the fixed stator are separated from the revolving rotor by a thin, glass fibre re-enforced epoxy sleeve. Only the rotor carrying the turbine wheel is in contact with the pumped gas, thus preventing contamination of the detector by outgassing from materials used in the stator volume for coil insulation etc. The separation sleeve is coated on the rotor side by a $5\,\mu$m thick titanium layer to avoid outgassing of the epoxy resin. Additional important parameters

[9] A certain amount of water is needed in the gas to prevent the MDT endplugs from drying out, which might result in HV problems (sparking) and/or micro cracks in the plastic material. On the other hand the sustainable water concentration is limited to a maximum of 1000 ppm in order to exclude corrosion of the compressor used to pump the gas.
[10] Aparáty Technologie Konstrukce, Hradec Králové, Czech Republic
[11] Electrografit GU 118, loaded with 5% anitmony, Kompozitum (Electrocarbon) Topolcany, Slovakia

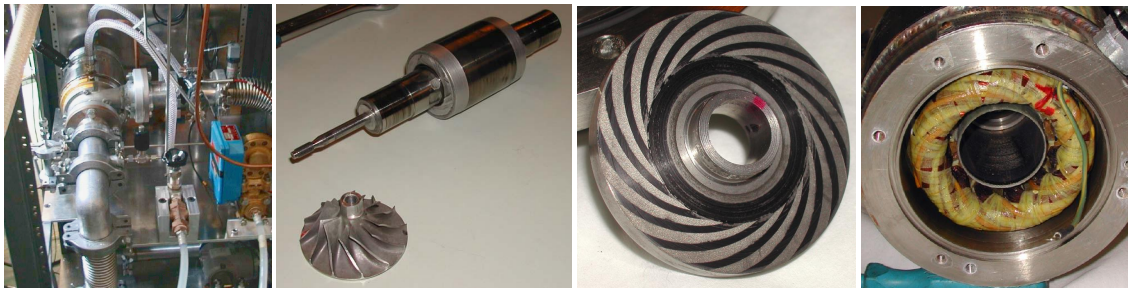

Figure 3.16: Argon Turbo Circulator ATC. From left to right: ATC installed in the setup at GIF, turbine rotor shaft and blade wheel, axial gas bearing (gas flowing through the precisely machined spiral grooves produces a cushion on which the rotor 'floats'), separation sleeve between stator coils and rotor volume.

of the ATC are summarized in table 3.2.

3.9.2 Gas supply and regulation system

The full gas supply and regulation system built for the measurements presented in this thesis is schematically shown in figure 3.17. Except for the analysis equipment, the system in principle consists of two independent subsystems, one for each multilayer of the BIS chamber under study. Gas going to multilayer 1 is recirculated using the ATC; multilayer 2 is operated in the classical flushing mode for comparison. The Ar:CO_2 operating gas is provided as a premix in batteries of 90 Nm^3 which supply both multilayers. The gas volume per battery is large enough to last for several months of operation.
The amount of gas flowing through multilayer 2 is regulated by a mass flow controller (MFC) (1)[12] while a back pressure regulator (3) keeps the drift tubes at the required 3 bar absolute pressure. Both instruments are electrically controlled by supplying an appropriate analogue input voltage as setpoint and by reading an output voltage corresponding to the value currently measured. Since the adjustable flow rates through the MFC (1) are

[12]Labels correspond to figure 3.17; the exact type of all components can be found in appendix C.

Parameter	Value
Nominal operating gas flow (Ar):	100 Nm^3/h
Maximum flow rate (Ar):	200 Nm^3/h
Gas pressure at inlet:	≈2.8...3.0 bar (abs.)
Gas pressure at outlet:	≈3.0...3.3 bar (abs.)
Maximum achievable Δp:	≈400 mbar
Maximum power at full speed:	2.5 kW
Maximum speed:	55 000 rpm
Cooling water flow:	≥ 1.5 l/min at 20°C
Electrical Supply:	3× 380 V 3 phase, up to 4.54 A each

Table 3.2: Operation parameters of the gas circulator ATC.

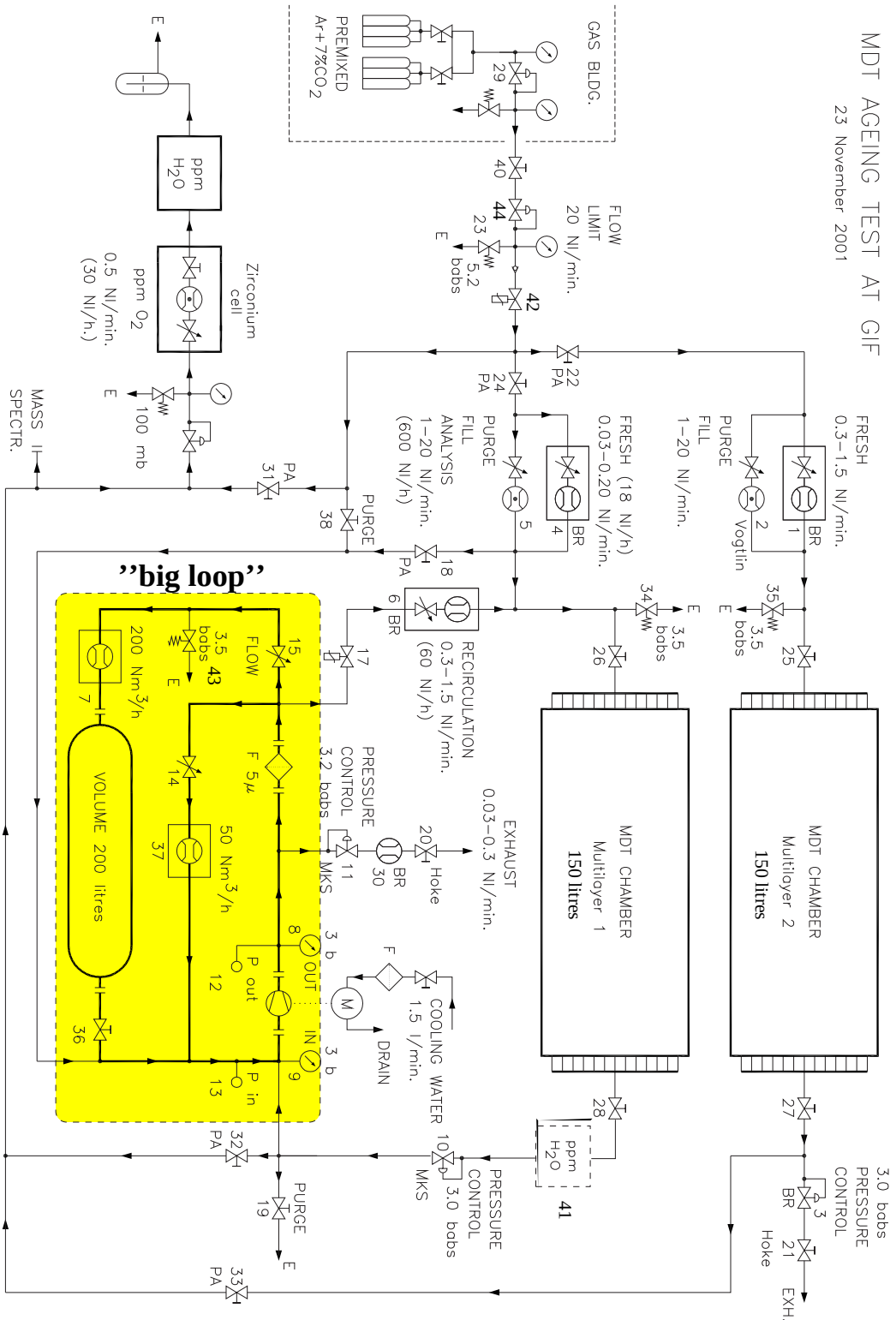

Figure 3.17: Off-chamber gas system. The so-called 'big loop' of the circulating part of the system is highlighted. Flow rates shown in brackets correspond to the maximum value possible for a given component; all other flow rates are nominal operating settings.

limited to a maximum of ≈ 100 Nl/h, an additional mechanical rotameter (2) can be used in parallel to increase the gas flow, especially during filling and purging of the system.
The setup for multilayer 1 is considerably more complicated; this is due to the fact that the gas flow through the ATC can only be adjusted within a small range while any test setup naturally has a much smaller volume than the full Atlas detector. In the system shown in figure 3.17 the so-called 'big loop' acts as a bypass for the major part of the circulating gas. Only a small fraction of less than 0.1% of the total flow of 100 Nm^3/h passes the BIS MDTs. The 200 l buffer volume is needed to limit mechanical stress due to vibrations caused by the turbulent flow regime in the big loop. Two large diameter manual valves (14,15) allow for the adjustment of the gas flow. Additional elements in the big loop are a particle filter (F) to retain dust rubbed off the graphite bearings during the startup phase of the ATC and any other material involuntarily introduced into the system, two flow meters (7,37) for monitoring and two simple pressure gauges (12,13) to check the pressure before and after the compressor.
The drift tubes of multilayer 1 are supplied from the big loop via the mass flow controller (6), while the fresh gas intake can be adjusted with mass flow controller (4). As for multilayer 2 a second branch in parallel allows for faster filling and/or purging of the system with larger quantities of fresh gas via MFC (5). Two pressure controllers (10,11) are used to keep the MDTs at 3 bar and to regulate the amount of gas released from the system to exhaust. In equilibrium conditions the exhaust flow, which is monitored by mass flow meter (30), is

$$Q_{out} = Q_{in} - Q_{leak}\,. \tag{3.2}$$

Figure 3.18 shows the measured exhaust flow versus time. One clearly sees that the flow rate is too small for the pressure regulator used, which causes alternating closed and open states of the control valve. Equation 3.2 still holds, if the flow rates Q are integrated over several oscillations. Pressure fluctuations in the big loop are negligible due to the large volume of the buffer. Operating the compressor such that the system is at 3.2 bar (abs.) on the high pressure side (8) and at 2.9 bar on the low pressure side (9) of the pump has turned out to be suited best for stable conditions and lies well within the operating range of the ATC. In all periods in which recirculation was used the fresh gas intake was set to 10% of the circulating flow, which was between 1 and 2 volume exchanges per day.

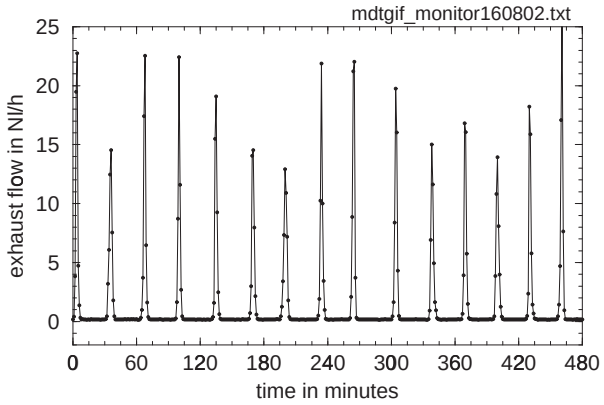

Figure 3.18:
Gas recirculation system exhaust flow versus time. The fresh gas intake rate was 2 Nl/h.

System behaviour in case of circulation failure

In case the flow in the big loop is stopped, the pressure difference between low and high pressure side of the compressor vanishes. Since the pressure drop in the big loop almost completely occurs across the strangulation valve (15), the main part of the loop is normally at ≈2.9 bar. This value slowly rises after a circulation failure due to the uninterrupted fresh gas intake via MFC (4). Gas will be released from the system by the controller (11) only when a pressure of 3.2 bar is reached. The pressure in the BIS chamber will initially stay at the nominal 3 bar, until the pressure drop across regulator (10) falls below the minimum of ≈50 mbar needed for the control valve to function properly. If the stop in circulation is not detected by then, the whole system (big loop and chamber) will stabilize at a total pressure of 3.2 bar, which is uncritical for the MDTs which have to stand up to 4 bar (abs.) according to the Atlas safety and quality assurance specification. For further protection self-releasing overpressure valves, set to open at 3.5 bar, have been included in the circuit at the chamber inputs. To avoid a back flow of gas from the chamber to the big loop if the gas recirculation is stopped, the electropneumatic valve (17) is automatically closed if the ATC is not running.

Operating multilayer 1 in flushing mode

Multilayer 1 can also be operated in classical single pass mode without gas recirculation. In this condition the fresh gas intake has to be increased typically by a factor 10. The only other change necessary to the setup is lowering the setpoint of pressure controller (11) in the exhaust line from the nominal 3.2 bar to around 2.8 bar, to allow for the necessary pressure drop across the chamber pressure regulator (10). The system was operated in this way during test beam data taking and during the period prior to phase 'Age1' (Jan./Feb. 2002), in which no irradiation was possible at GIF.

Gas analysis equipment

Several devices for monitoring the water and oxygen concentration in the gas have been included in the prototype system. Water and oxygen levels are measured in a special analysis line which can alternatively receive gas from either of the two chamber multilayers or directly from the premix supply. During ageing period 'Age1' the water content was measured using a moisture meter model SDA[13], which deduces the H_2O concentration from measuring the humidity dependent dielectric constant of a special analysis cell. This instrument was later found to be not working and was replaced by a dew point hygrometer model M4, by General Eastern Instruments, Woburn, US. The dew point is the temperature at which water can exist in equilibrium in both vaporized and liquid state. This temperature can be measured by cooling down a mirror in the gas flow until water condenses on its surface, a condition which is detected by a change in the reflectivity for light. Oxygen is monitored using a Teledyne 316A-2X[14] with a zirconium cell A-2C suitable for use with CO_2 containing gas mixtures.
The water measurement turned out to suffer from the low available flow (which goes to exhaust and is thus 'lost' from the circulation loop); a second dew point hygrometer (41), model 2000 Series DewPrime by EdgeTech, Milford, US, was therefore installed into the system just in front of the chamber pressure regulator (10) during ageing period 'Age2'.

[13] Shaw Moisture Meters, Westgate, UK
[14] Teledyne Analytical Instruments, Los Angeles, US

3.9.3 Slowcontrol and safety interlocks

The gas recirculation system had to run continuously without the presence of personnel. A dedicated monitoring software, commonly referred to as slowcontrol, was developed by C. Cernoch to record all slowly varying parameters of the system and to constantly check for any abnormal and potentially dangerous situation such as a loss of pressure, overheating of the pump, etc. All slowcontrol code was written in LabView 6i from National Instruments. Only the most relevant features are summarized here, more details can be found in [35] and [36].
The ATC, or more precisely the frequency converter supplying power to it, was interfaced to the slowcontrol PC using a Profibus[15] connection. Profibus was also used to access special slowcontrol ADCs which read the analogue output signals from the various pressure and flow sensors in the system. In addition to the gas system parameters the HV supplied to and the current in both BIS multilayers as well as the chamber temperature was recorded. All readings were written to disk in an ASCII format once per minute. The ATC was immediately switched off if any of the following situations occured:

- cooling water off
- ATC inlet pressure too low ($p_{in} < 2.7\,\text{bar abs.}$)[16]
- ATC outlet pressure too high ($p_{out} > 3.4\,\text{bar abs.}$)[17]
- big loop gas flow below $90\,\text{Nm}^3/\text{h}$
- ATC overheating

In case the ATC was turned off by the slowcontrol the high voltage of the MDTs was switched off and the user was notified by email and SMS.

3.9.4 Experiences with operating the recirculation system

During the 9 months of continuous operation in ageing periods 'Age1' and 'Age2' no major problems were encountered with the recirculation system, with the exception of electromagnetic interference caused by the ATC frequency converter which is discussed below. Figure 3.19 shows the Δp generated by the compressor and the flow rate in the big loop over 24 hours. Both quantities are constant within 3 (Δp) and 1 percent (flow) respectively, which is adequate for the later Atlas operation.
The recirculating part of the gas system itself had a total leak rate of $\approx 4 \cdot 10^{-2}\,\text{mbar}\cdot\text{l/s}$; this is roughly twice as much as the leak rate of BIS multilayer 1. The combined leak rate (gas system plus MDTs) is higher than expected at Atlas by a factor of at least 5. The oxygen concentration in the gas nevertheless stayed below the required 100 ppm. A purification stage for oxygen will therefore probably not be needed in the final Atlas system.

Water concentration in the gas

In section 2.2.2 it was pointed out that the amount of water in the operating gas strongly influences the electron drift process. Figure 3.20 shows the water content in the circulation

[15] field bus system according to standards IEC 61158 and IEC 61784
[16] Too low pressures lead to vibrations, which quickly damage the ATC gas bearings.
[17] Too high pressures or an excessive gas flow overload the pump motor.

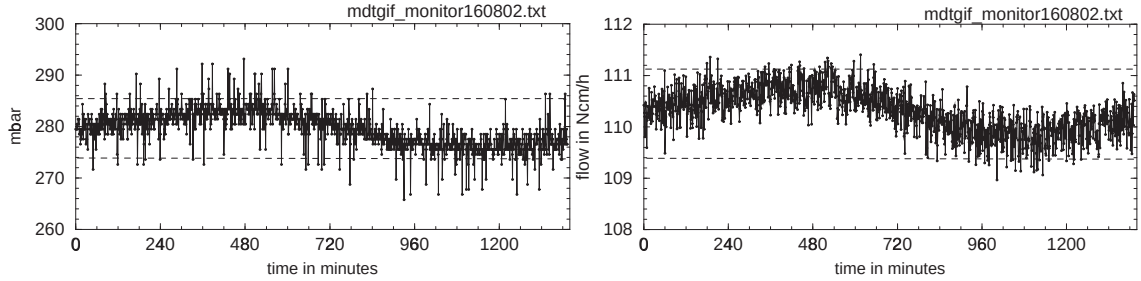

Figure 3.19: Measured pressure difference between in- and output of the ATC (left) and gas flow rate (right) in the 'big' loop over 24 hours. Except for isolated points which are most likely noise spikes on the analogue slowcontrol readings, the stability is better than $\approx 3\%$ for Δp and better than 1% for the flow rate. ATC operation was at 42000 rpm.

system, measured with the help of dew point hygrometer (41), for two different periods. At $t = 0$ in the left plot the system was purged with fresh gas from the premix supply; after this a circulating flow of 20 Nl/h and a fresh gas replacement rate of 2 Nl/h was maintained (standard Atlas conditions, 1 vol./day circulation, 10% fresh gas exchange). The water concentration exhibits a fast increase and stabilizes around 1000 ppm which is the maximum set by the ATC manufacturer in order to exclude corrosion of the ATC bearings. The obtained curve follows the relation

$$c_{water}(t) = c_0 \cdot e^{-\frac{\dot{V}}{V}t} + c_1 \cdot (1 - e^{-\frac{\dot{V}}{V}t}) \tag{3.3}$$

which is expected if a constant 'influx' of water into the system (diffusion, desorption from surfaces) is assumed. c_0 is the initial, c_1 the final water concentration; $\dot{V}$ is the gas refreshment rate.
The right plot of figure 3.20 shows the water concentration during ageing period 'Age2', together with the maximum drift time obtained in weekly reference runs with cosmic

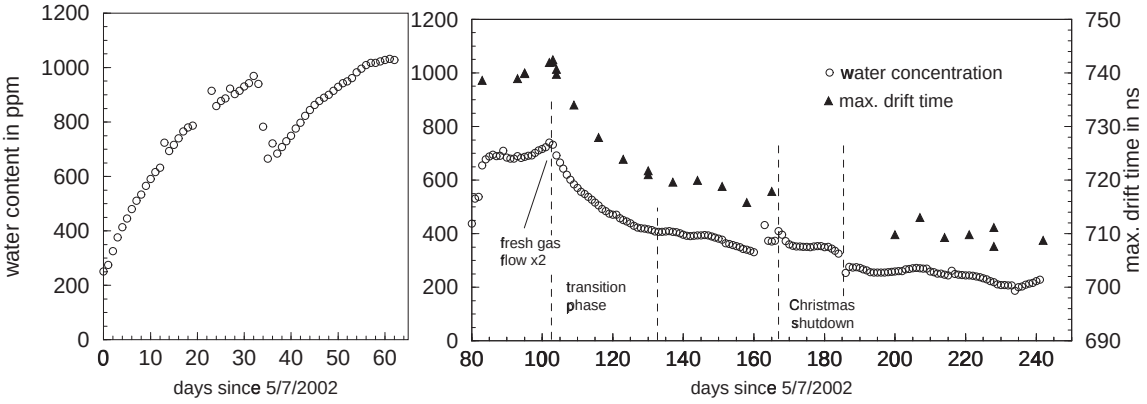

Figure 3.20: Water concentration in the gas recirculation system. The left plot shows the water content in a 60 day period after (partially) purging the system. Water concentrations up to 1000 ppm were reached. The right plot shows the water concentration and the measured maximum drift time t_{max} in ageing period 'Age2'. There is a clear correlation between the two quantities. t_{max} values have been corrected for temperature changes.

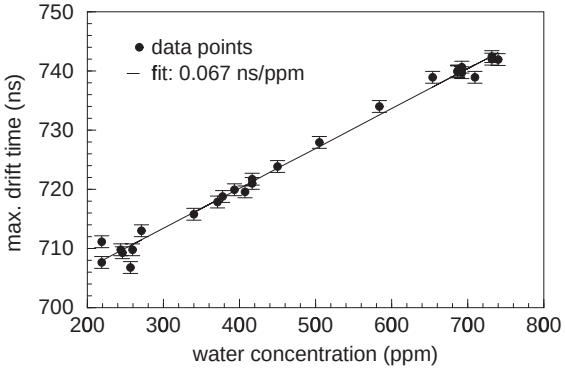

Figure 3.21:
Maximum drift time versus water concentration. The data confirms a linear relation, as expected from GARFIELD simulations. The slope obtained from the measurements is 0.067 ns/ppm while the simulation yields 0.066 ns/ppm.

muons. The sudden decrease in the water content at day 103 is due to a doubling of all flow rates which was done to compensate for increased high voltage settings from that time onwards. From equation (3.3) one expects the system to stabilize again within ≈ 3 volume exchanges after a modification in the flow rates. This is not true for the right part of figure 3.20, where the water concentration decreases over the full time range shown. It is currently believed that this is at least partially due to water getting into the system via diffusion through the MDT endplugs and plastic gas connections. In this case the water 'influx' depends on the outside humidity which was lower towards the end (winter) of period 'Age2' than at the beginning (autumn). Drying up of residual traces of water in the materials forming an MDT may also play a role.
Rather than plotting maximum drift times and water concentrations separately versus time both values can be plotted against each other. This is done in figure 3.21. The result agrees with a linear relation, as expected from the GARFIELD simulation (section 2.2.2, fig. 2.9).

Electromagnetic interference and induced noise

When the BIS chamber was put under high voltage and read out for the first time with the gas recirculation system running, an unacceptably high level of noise was found in the MDTs. Noise rates dropped by several orders of magnitude when the gas circulation was switched off.
The problem was traced to the ATC frequency converter which generates a large amount of electromagnetic interference due to the high power alternating currents in the kHz domain it supplies to the pump. Figure 3.22 shows measured MDT noise rates with the gas recirculation system switched on and off after the grounding and shielding configuration of the frequency converter and pump was improved. There is still a significant difference between the two cases, especially in the outer tube layers.
One is tempted to think that the problem of electromagnetic emission by the ATC will be less critical for the final Atlas setup due to the large spatial distance between the gas system (surface building) and the detector (underground cavern). This is certainly true if noise is induced on the chamber by direct electromagnetic radiation through the air, but is less obvious if electric disturbances travel via conducting materials and/or the ground connections. For the setup used in this thesis the dominant mechanism of noise propagation seemed to be via the metal gas pipes connecting the BIS chamber to the recirculation system 30 m away. With the pipes removed no increased noise rates were observed when the ATC was running. Decoupling the gas lines electrically from the MDTs

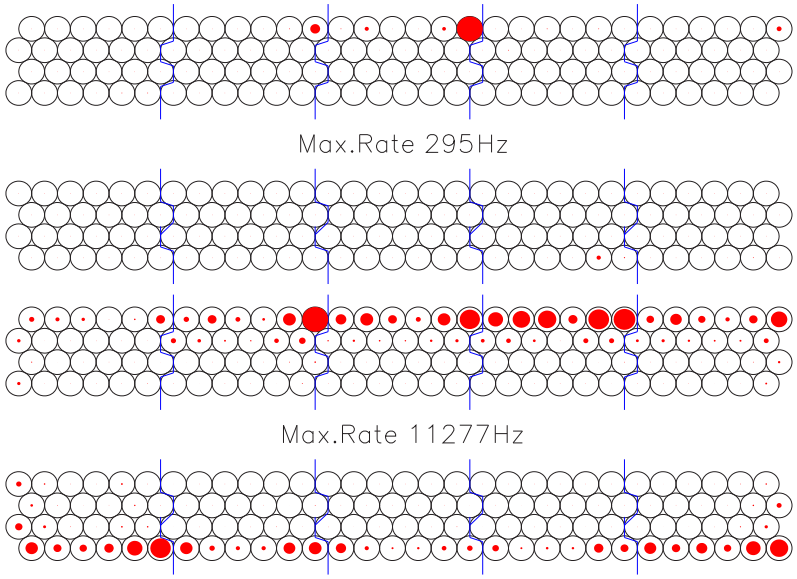

Figure 3.22: Measured single tube noise rates at nominal threshold with the ATC switched off (top) and running (bottom), after the electromagnetic emission had been reduced by an improved shielding and grounding configuration. The area of the filled circles is proportional to the measured count rate.

at the chamber connection point and from the gas recirculation rack helped to reduce the amount of electrical disturbance seen in the drift tubes, but did not fully eliminate it.

'Wise Man: One who sees the storm coming before the clouds appear.'
Elbert Hubbard, 1856 - 1915

Chapter 4

Test beam studies – MDT performance under high rates

This chapter is devoted to the MDT performance under high rates. Results presented here are based on the analysis of data taken at GIF during the test beam period in summer 2002. 100 GeV muons from CERN's X5 beam line were used to study track reconstruction and the MDT behaviour; an Atlas-like background environment was simulated with the help of the GIF radioactive γ-source.
Section 4.1 gives an overview over the beam and radiation conditions during data taking while section 4.2 presents the changes observed in the drift time spectrum with increasing rate. Paragraph 4.3 summarizes the basics of track reconstruction; the remainder of the chapter discusses single tube resolution (4.4) and efficiency (4.5).

4.1 Radiation environment and muon beam

Determining photon count rates

When discussing the MDT behaviour in a high background environment it is important to know the actual rate with which interactions occur. Rates in this thesis were measured using a 'random' trigger, i.e. a trigger signal coming from a pulse generator and thus uncorrelated to the passage of any particle through the detector. Tube count rates were obtained by counting the number of hits recorded by the AMT in the total time interval

$$\Delta t = \text{number of triggers} \cdot \text{ AMT match window} \tag{4.1}$$

for a given channel. This definition is appropriate when measuring noise rates; for energetic particles (muons, photons above ≈100 keV) the situation is more complicated since each particle interaction will usually result in more than one MDT hit due to the small dead time of the front end electronics (sections 2.2.1 and 3.6.2). To deal with these multiple threshold crossings only the first hit found by the AMT in its match window was counted. Rates calculated in this way as

$$R' = \dot{N}_{count} = \frac{total\ number\ of\ first\ hits}{total\ time\ interval\ \Delta t} \tag{4.2}$$

are too small since not only multiple hits from the same event, but also hits from a second event within the same AMT match window are suppressed. This can be corrected for in the following way:

Assume the 'true' rate of particle interactions is R. Then the probability to observe at least one hit in a given AMT match interval Δt_{AMT} is

$$\int_0^{\Delta t_{AMT}} R \cdot e^{-R \cdot t} dt = 1 - e^{-R \cdot \Delta t_{AMT}}.$$

If the total number of recorded AMT match intervals is n, on average

$$n \cdot (1 - e^{-R \cdot \Delta t_{AMT}})$$

of them contain at least one hit. The rate R' defined in equation (4.2) is therefore

$$R' = \frac{n \cdot (1 - e^{-R \cdot \Delta t_{AMT}})}{n \cdot \Delta t_{AMT}} \ , \tag{4.3}$$

which can be solved for the true rate R. If one does not apply the correction described here, the systematic error in the rate determination exceeds 10% for $R \cdot \Delta t_{AMT} > 0.2$, which is well within the range of γ-rates encountered in the measurements presented in this chapter.

Primary ionization per photon event

From the individual MDT count rates $\dot{N}_{count,i}$ and the chamber current the average number $\bar{N}_{p.e.}$ of primary electrons created in the gas by one interacting photon could be calculated. A value of

$$\bar{N}_{p.e.} \cdot G = \frac{I_{chamber}}{e \cdot \sum_i \dot{N}_{count,i}} = 2.57 \cdot 10^7 \pm 20\% \tag{4.4}$$

was found; assuming a gas gain $G = 2 \cdot 10^4$ one arrives at $\bar{N}_{p.e.} = 1285$. Comparing this number to the value of $\bar{N}_{p.e.} = 1235$ given in section 2.3 as expected at the LHC, one can see that the radioactive ^{137}Cs source at GIF is well suited to simulate Atlas conditions.

Background uniformity

Figure 4.1 shows measured MDT count rates for various settings of the lead absorber system between the radioactive source and the BIS chamber. The decrease in count rate is less pronounced than it would be expected from the nominal filter attenuation factors; this is due to the high percentage of photons losing only part of their energy in Compton-interactions with the filter material, rather than being fully absorbed.
More important is the fact that the photon flux was distinctly non-uniform across the width (90 cm) of the BIS chamber. This is contrary to the measurements performed during the commissioning phase of GIF [1]. Even in the much smaller region covered by the muon beam γ-rates varied by almost a factor 2. The non-uniformity of the radiation background was attributed to uneven shielding effects caused by several small size setups from other groups which were located between the ^{137}Cs-source and the MDT setup.

Muon beam

All data presented in this section was taken at a beam energy of 100 GeV. A 5.40 m iron dump in front of the GIF zone stopped all particles except muons. Depending on whether additional dumps upstream were in the beam line or not, the diameter of the beam spot in GIF varied between 10 and 20 cm with muon count rates between 400 and 1200 Hz.

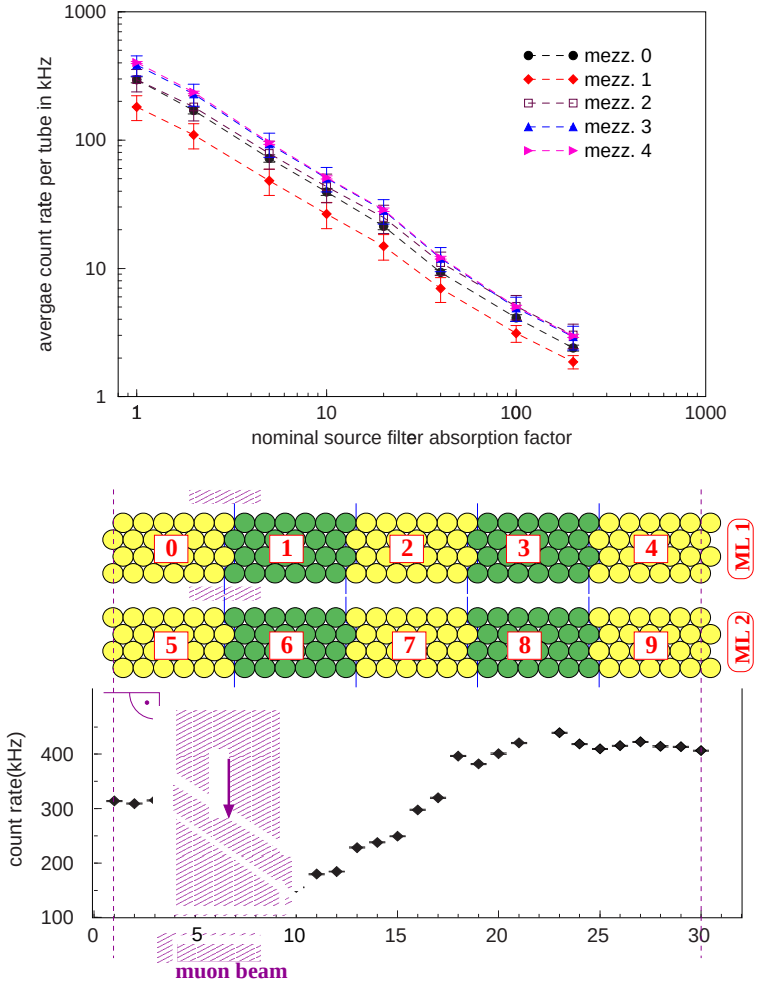

Figure 4.1: Photon background during test beam data taking. The top figure shows the average tube count rate for the mezzanine cards in BIS multilayer 1 and different absorption filters in front of the GIF source. Error bars correspond to the variation of the rate within each card. The results for multilayer 2 are equivalent. The curves for different mezzanines do not coincide; this is clear evidence for the γ-irradiation being non-uniform across the chamber width. The bottom figure shows the rate variation in more detail for the maximum level of background. In the region covered by the muon beam the background changes by almost a factor 2.

For about 5% of the events double tracks were found (fig. 4.2, top); another 4% showed hits in more than 25 of the MDTs (fig. 4.2, bottom). Only events with single tracks have been used in the data analysis.

4.2 Drift time spectrum analysis

Typical MDT drift time spectra, with and without the presence of a photon background, are shown in figure 4.3. Commonly used parameters to characterize the spectrum are the position of the rising (leading) edge, t_0, the position of the falling (trailing) edge, t_{end}, and

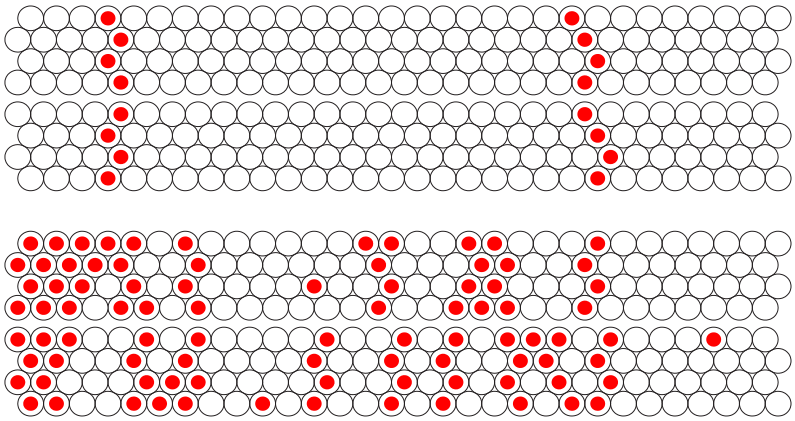

Figure 4.2: Top: double track event as observed with a probability of $5-6\,\%$*. Bottom: typical shower hit pattern (*≥ 25 *hits) as found in* $\approx 4\,\%$ *of all events (without* γ*-background).*

the maximum drift time

$$t_{max} = t_{end} - t_0\,. \tag{4.5}$$

In the case of no radiation background, t_0 and t_{end} are obtained by fitting a Fermi-function,

$$f(t) = p_1 + \frac{p_2}{1 + e^{-\frac{t-t_0}{p_3}}}, \quad p_3 > 0, \tag{4.6}$$

to the leading edge of the spectrum and a modified Fermi-function,

$$g(t) = q_1 + \frac{q_2 + q_3 \cdot t}{1 + e^{-\frac{t-t_{end}}{q_4}}}, \quad q_3, q_4 < 0\,, \tag{4.7}$$

to the trailing edge. The value of t_0 is defined to a large extent by the trigger latency, i.e. the time between the passage of a particle through the detector and generation of the trigger signal. The parameter p_3 of the rising edge fit is directly related to the MDT resolution close to the wire; a larger spread in the electron arrival time leads to larger values of p_3.

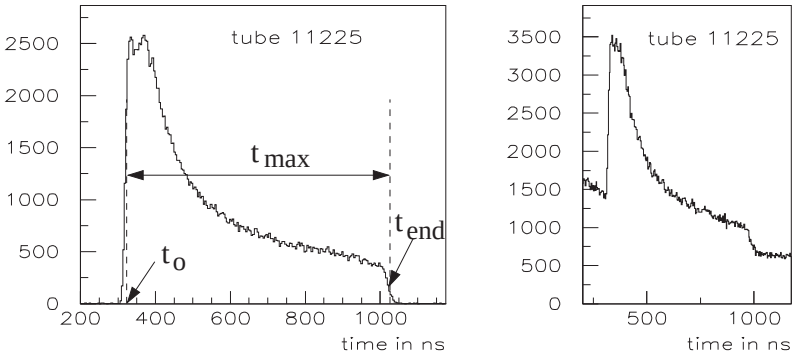

Figure 4.3: MDT drift time spectrum with and without photon background. The left plot shows the spectrum when no background radiation is present. The right plot shows the spectrum for the same tube at $\approx 200\,kHz$ γ*-count rate (400 Hz/cm*^{2}*).*

4.2.1 Spectrum unfolding

Under γ-irradiation the muon drift time spectrum is overlaid by photon hits, as can be seen from the right part of figure 4.3. Before a fit to the leading and trailing edge can be performed the muon contribution has to be extracted from the full spectrum. This process is known as unfolding and will be discussed here.
Seen from a statistical point of view, the measured drift time spectrum is the probability distribution for the arrival time of hits with respect to the trigger signal. If all hits found in the AMT match window were used, the observed drift time spectrum would be a simple superposition of the muon and photon contributions,

$$\rho_{obs,\,all\,hits}(t) = \rho_\mu(t) + \rho_\gamma(t)\,.$$

In truth only the first hit found in the match window is considered (since both muons and high-energetic photons produce several threshold crossings, as discussed in sections 2.2.1 and 3.6.2); in this case and provided that only events where the tube under study was actually crossed by the muon generating the trigger signal are used, the more complicated expression

$$\rho_{obs,\,first\,hit}(t) = \underbrace{\rho_\gamma(t)\cdot\left[1-\int_{t_0}^{t}\rho_\mu(t')dt'\right]}_{A} + \underbrace{\rho_\mu(t)\cdot\left[1-\int_{t_0}^{t}\rho_\gamma(t')dt'\right]}_{B} \quad \text{with} \tag{4.8}$$

$\rho_\mu(t)$: probability distribution for the arrival time of the first muon hit
$\rho_\gamma(t)$: probability distribution for the arrival time of the first γ-hit

holds. Expression A is the probability to observe the first γ-hit at time t and no muon hit at a time $t' < t$; B is the probability to observe a muon at time t which is not masked by an earlier photon. t_0 is the time of the trigger signal. In the following the steps necessary to solve (4.8) for the muon time spectrum $\rho_\mu(t)$ will be described. The index 'first hit' will be omitted for simplicity.

The γ-spectrum $\rho_\gamma(t)$: For photon interactions occurring with a constant rate λ_γ the waiting time for observing the first hit follows an exponential distribution

$$\rho_\gamma(t) = \lambda_\gamma \cdot e^{-\lambda_\gamma \cdot t}\,. \tag{4.9}$$

When looking at arrival time spectra for pure γ-radiation, measured using the same uncorrelated 'random' trigger as for photon rate determination, at a first glance the obtained distributions seem however to deviate from the expected exponential relation (fig. 4.4, top curve). This is due to the fact that part of the observed hits at small times t are secondary threshold crossings from photon events outside the actual AMT match window. If only events which show no hits in the 500 ns preceding the start of the match window are selected[1], the surplus of small arrival times disappears (fig. 4.4, red curve). The histogram now has the expected exponential shape with a λ_γ corresponding to the measured γ-rate. All drift time analysis has been limited to such events.
In a first step an exponential is fitted to the region $t > t_{end}$ of the measured drift time spectrum. Entries in this part of the spectrum come exclusively from background hits. They furthermore stem from such events, in which the tube under study was not crossed

[1] by checking if the AMT mask flag was set or not for a given tube

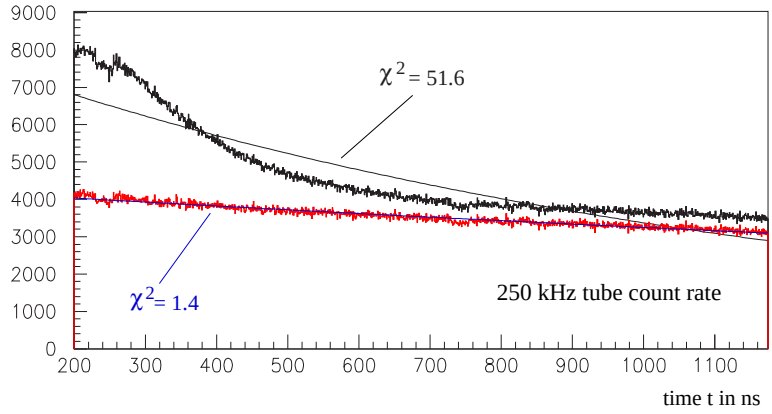

Figure 4.4: Time distribution for the first γ-hit observed when using a pulse generator trigger uncorrelated to the beam. Triggers were disabled during the beam spill to guarantee a pure photon data sample. The top black curve shows the obtained histogram if no events are rejected. In this case the distribution cannot be fitted with an exponential (black line). For the red curve below, events for which a hit was seen in the 500 ns preceding the actual AMT match window were rejected. The resulting histogram can very well be described by an exponential (blue line).

by the beam muon which generated the trigger signal (otherwise this muon would have caused a histogram entry at a time smaller than the trailing edge which in turn would have masked the γ-hit). The exponential is extrapolated to earlier times t and subtracted from the measured spectrum. The result of this operation is ρ_{obs} in equation (4.8).
Next ρ_{obs} is fitted in the region to the left of the leading edge with a second exponential, giving the photon arrival time distribution $\rho_\gamma(t)$.

Obtaining $\rho_\mu(t)$: Formula (4.8) can be rearranged into

$$\rho_\mu(t) = \frac{\rho_{observed}(t) - \rho_\gamma(t) \cdot \left[1 - \int_{t_0}^{t} \rho_\mu(t')dt'\right]}{\left[1 - \int_{t_0}^{t} \rho_\gamma(t')dt'\right]} \,. \tag{4.10}$$

Since for a given t on the left hand side only times $t' < t$ appear on the right hand side, (4.10) can be evaluated in discrete steps once ρ_γ is known. Figure 4.5 compares the muon drift time spectrum obtained using the unfolding method to the one obtained using the 'naive' approach of simply subtracting $\rho_\gamma(t)$ from $\rho_{obs}(t)$. One can see that with the simple subtraction method there is a suppression of large drift times; t_{max} values calculated from such spectra are systematically too small.

4.2.2 Maximum drift time changes with background rate

Figure 4.6 shows the maximum drift times t_{max}, obtained from the unfolded drift time spectra, for various levels of photon background. t_{max} decreases linearly with increasing count rate. In chapter 5 it will be shown that this behaviour can be understood from a simple model for the space charge created in background events, which modifies the electric drift field. For the maximum radiation levels of 500 Hz/cm^2 expected at Atlas the change in drift time is ≈ 30 ns. Assuming an average electron drift velocity of approximately 20 μm/ns, this corresponds to a change by up to 600 μm in the rt-relation. Since the

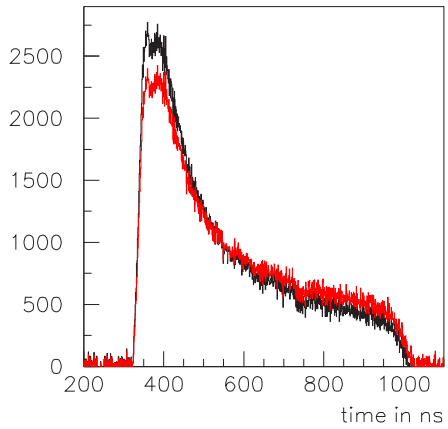

Figure 4.5:
Black: muon arrival time spectrum $\rho_\mu(t)$ obtained by simply subtracting $\rho_\gamma(t)$ from $\rho_{obs}(t)$. Red: Drift time spectrum after applying the unfolding method described in the text. Both distributions have been normalized to the same number of entries. One can see that the simple subtraction method suppresses large drift times. The shown spectra are for a tube count rate of 250 kHz. If t_{max} is calculated from the black spectrum, the value found is too small by 6 ns compared to the number obtained from the correctly unfolded spectrum.

rt-relation must be known with an uncertainty no larger than 20 μm in order for the Atlas muon spectrometer to reach its full precision, rate effects clearly have to be taken into account.

4.2.3 Temperature dependence

The maximum drift time is temperature dependent. This is due to the fact that the electron drift in the operating gas becomes faster when the gas density decreases. The linear relation

$$\Delta t_{max} = (-2.3 \pm 0.1)\,\mathrm{ns/K} \cdot \Delta T \tag{4.11}$$

was found measuring t_{max} for different temperatures during test beam data taking.

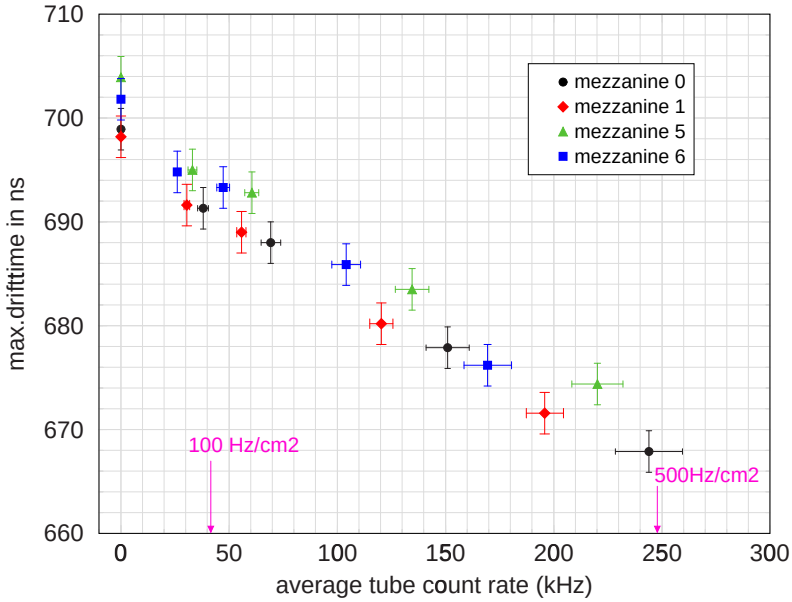

Figure 4.6: Maximum drift time t_{max} versus background intensity. t_{max} shows a linear decrease with rate. For the maximum radiation levels expected at Atlas (500 Hz/cm^2) the change in drift time is ≈ 30 ns.

4.3 Track reconstruction and autocalibration

Since no magnetic field was present during the test beam measurements presented here, trajectories of high-energetic particles traversing the MDT chamber can be considered as straight lines. A track can be defined in the plane perpendicular to the wires as

$$z(y) = m \cdot y + c\,. \tag{4.12}$$

y and z are the local multilayer coordinates defined in section 3.8. The parameters c and m are found by minimizing the expression

$$\chi^2 = \frac{1}{n-2} \cdot \sum_{i=1}^{n} \Bigg(\underbrace{\frac{|m \cdot y_i + c - z_i|}{\sqrt{1+m^2}} - r_i}_{=:\,\Delta_i} \Bigg)^2 / \sigma_i^2\,. \tag{4.13}$$

The sum runs over all hits belonging to the track; for each hit, (y_i, z_i) are the coordinates of the wire, r_i is the drift radius calculated from the measured drift time t_i and σ_i is the single tube resolution, i.e. the standard error of r_i. The term Δ_i is commonly referred to as residual; it is the closest distance between the track and a circle with radius r_i around the wire belonging to the i-th hit. All track fitting was carried out using the software package CALIB [21].

4.3.1 Finding an initial rt-relation

Before a track can be reconstructed, all measured drift times, t_i, have to be converted into corresponding drift radii $r_i = r(t_i)$. For this the rt-relation, $r(t)$, must be known. A first approximation of $r(t)$ can be obtained from the (unfolded) drift time spectrum by a procedure known as integration method [39]:
Assume the track distance from the wire of an MDT is distributed according to $\rho_r(r)$. The drift time spectrum is, except for normalization, the probability distribution $\rho_t(t)$ for the arrival of the first drifting electrons at the wire. If the rt-relation is $f(t) \equiv r(t)$, then conservation of probability dictates

$$\int_{t_1}^{t_2} \rho_t(t)dt \stackrel{!}{=} \int_{f(t_1)}^{f(t_2)} \rho_r(r)dr = \int_{t_1}^{t_2} \rho_r(f(t)) \cdot \frac{df}{dt}(t)\,dt \tag{4.14}$$

and therefore

$$\rho_t(t) = \rho_r(f(t)) \cdot \frac{df}{dt}(t)\,. \tag{4.15}$$

For a uniform tube illumination, ρ_r is given as (a : wire radius, b : tube radius)

$$\rho_r(r) = \begin{cases} \frac{1}{b-a}, & a < r < b \\ 0, & \text{otherwise} \end{cases} \tag{4.16}$$

which makes it possible to solve (4.15) for the rt-relation

$$r(t) \equiv f(t) = a + (b-a) \cdot \int_{t_0}^{t} \rho_t(t')dt'\,. \tag{4.17}$$

Rt-relations calculated by this method are accurate to a few hundred micrometers. Deviations from the 'true' rt-relation come from the limited MDT resolution, noise and δ-electron contributions in the drift time spectrum etc. An iterative procedure, known as autocalibration, is therefore normally applied to improve the rt-relation.

4.3.2 Autocalibration method

For a perfect rt-relation one expects the distribution of the residuals Δ_i defined in formula (4.13) to be centered at 0. During autocalibration tracks are reconstructed using an approximate initial rt-relation $r_0(t)$. The mean $\overline{\Delta}_i(t)$ of the residual distribution for a certain 'slice' in t is then used as a correction to $r_0(t)$,

$$r_1(t) = r_0(t) + c \cdot \overline{\Delta}_i(t)\,.$$

The procedure is iterated until a stable rt-relation is reached. The factor c is a constant which depends on the number of tube layers used for track reconstruction, the geometry and the position of the MDT(s) used to calculate Δ_i.
The rt-relations used in this thesis were obtained combining runs for 5 different angles[2] of the chamber with respect to the beam (-12, -7, 0, +7, +15^o). Track reconstruction was done using all 8 tube layers with separate rt-relations in the 2 multilayers (which had slightly different drift times due to an individual regulation of the pressure).
A full autocalibration was performed for a few selected γ-rates only. For all other levels of background the rt-relations were calculated from the one without background as [5]

$$r(t) = r_0(t) + \delta r(t) \quad \text{with} \tag{4.18a}$$

$$\delta r(r) = \nu \cdot \left[t \cdot \dot{r}_0(t) - r_0(t) + \frac{6 \cdot ln\frac{b}{a}}{b^2} \cdot \dot{r}_0(t) \cdot \int_0^t \left(\frac{\dot{r}_0(t')}{\dot{r}_0(t)} - 1\right) \cdot r_o(t')^2 \, dt' \right], \tag{4.18b}$$

$$\nu := \frac{\lambda_\gamma \cdot \bar{N}_{p.e.} \cdot e \cdot G}{8 \cdot \pi \cdot \varepsilon_0 \cdot V^2} \cdot \frac{b^2 \cdot ln\frac{b}{a}}{\mu \cdot p}\,, \tag{4.18c}$$

a : wire diameter,
b : inner tube diameter,
λ_γ : count rate per cm tube length,
$\bar{N}_{p.e.}$: primary electrons per γ-event,
G: gas gain,
V : anode wire potential,
μ : ion mobility, p : pressure,
$r_0(t)$: rt-relation without γ-background.

A formula identical to (4.18a) with

$$\delta r(r) = \left(\frac{T}{T_0} - 1\right) \cdot [r_0(t) - t \cdot \dot{r}_0(t)], \quad T, T_0 \text{ in Kelvin}, \tag{4.19}$$

was used to correct for changes in the temperature [5].

4.4 Single tube resolution

The single tube resolution σ is the intrinsic accuracy of a drift tube with which a track position can be reconstructed. σ depends on the drift radius. For a sample containing a large number N of tracks, which all traverse an MDT in a distance d from the wire, the resolution is defined as

$$\sigma^2(d) = \frac{1}{N} \cdot \sum_i^N |d - r(t_i)|^2\,; \tag{4.20}$$

$r(t_i)$ is the drift radius reconstructed from the measured drift time of the i-th track.

[2] A certain minimum spread in angle is necessary to prevent the autocalibration from converging to a wrong rt-relation.

A good single tube resolution is crucial to a precise momentum reconstruction in the Atlas muon spectrometer, in particular for high-energetic particles. The design goal of the Atlas MDTs is an average tube resolution of better than 80 μm [13]; if one requires at least 3 'good' hits for track reconstruction, this value translates into a track position accuracy of 50 μm for each of the three Atlas muon stations. The average resolution $\bar{\sigma}$ in this context is defined as

$$\frac{1}{\bar{\sigma}^2} = \left\langle \frac{1}{\sigma(r)^2} \right\rangle \tag{4.21}$$

where $< ... >$ stands for a mean value. (4.21) takes into account that points with a small $\sigma(r)$ contribute more to the track fit than points with a large one.

4.4.1 Determining tube resolutions without external reference

To calculate the tube resolution directly according to equation (4.20), the track position d with respect to the wire must be known accurately. This is e.g. the case if d is measured independently of the drift chamber by a high precision external reference tracker (silicon telescope or similar). No such detector was available in the studies presented here. d had to be determined from the MDT data itself and a more complicated procedure had to be used to obtain the resolution curve $\sigma(r)$. The following steps were necessary:

1. Search for hit-patterns belonging to tracks with ≥ 8 hits; use events with one identified track only;
2. Exclude one tube from the track, fit a straight line to the remaining hits according to equation (4.13), using an estimated resolution $\sigma_n(r)$ with $n = 0$.
3. Extrapolate the found track to the excluded tube; calculate the track distance r_{track} from the tube wire;
4. Calculate the residual $\Delta(r_{track}) = r_{track} - r_{drift}$ and the fit extrapolation error, i.e. the error in r_{track}, $\epsilon(r_{track})$ for the excluded tube;
5. Repeat 1. to 4. until all events are processed;
6. For 0.5 mm wide slices in r, fit a Gaussian with width σ_δ to the center of the residual distribution. Calculate the average extrapolation error $\bar{\epsilon}$ in the same slice;
7. Calculate a new estimate for the tube resolution as[3]
$$\sigma_{n+1}(r) = \sqrt{\sigma_\delta(r)^2 - \bar{\epsilon}(r)^2}\,; \tag{4.22}$$
8. Iterate 1. to 7. until $\sigma_{n+1} = \sigma_n$.

Equation (4.22) can be derived in the following way: Assume the 'true' track distance from the wire of the excluded tube is r_{true}, the one found from the track fit is r_{track}. Let $< ... >$ denote an expectation value. Then

$$\begin{aligned}\sigma_\delta^2 &= < (r_{drift} - r_{track})^2 > = < (r_{drift} - r_{true} + r_{true} - r_{track})^2 > \\ &= < (r_{drift} - r_{true})^2 > + < (r_{true} - r_{track})^2 > + 2 < \underbrace{(r_{drift} - r_{true})}_{A} \cdot \underbrace{(r_{true} - r_{track})}_{B} >\end{aligned}$$

[3] This is only true if the width of the extrapolation error distribution is negligible. Otherwise the more general relation $\sigma^2 = \sigma_\delta^2 - \bar{\epsilon}^2 - Var(\epsilon)$ must be used.

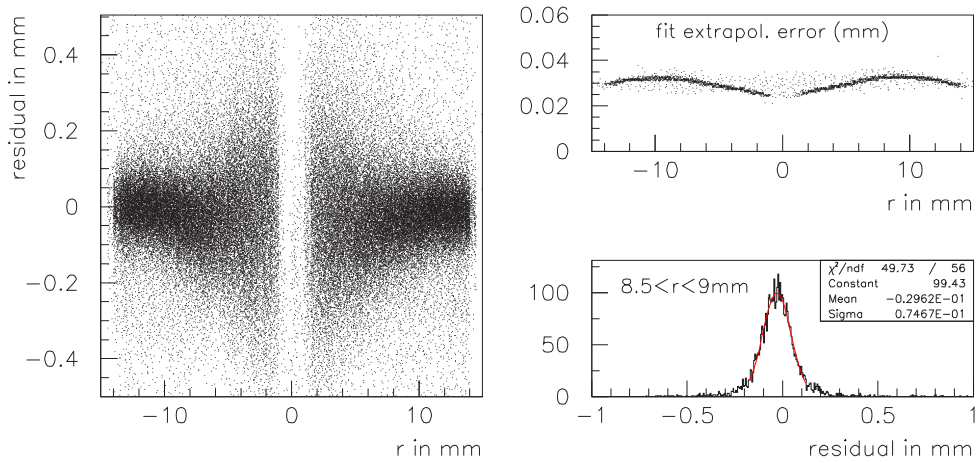

Figure 4.7: Distributions encountered in resolution determination. The left plot shows calculated residuals versus the track distance r from the wire; the right top plot shows the fit extrapolation error ϵ. The bottom plot on the right contains the residuals for a 'slice' in r; σ_δ is obtained by fitting a Gaussian to this distribution.

Since the tube under study was excluded from the track fit, r_{drift} and r_{true} and therefore also A and B are stochastically independent; the expectation value $< A \cdot B >$ vanishes. One obtains

$$\sigma_\delta^2 = \underbrace{< (r_{drift} - r_{true})^2 >}_{=\sigma^2} + \underbrace{< (r_{true} - r_{track})^2 >}_{=<\epsilon^2> = \bar{\epsilon}(r)^2 + Var(\epsilon) \approx \bar{\epsilon}(r)^2}$$

which after rearrangement gives (4.22). Typical distributions found for the residual σ_δ and the fit extrapolation error ϵ are shown in figure 4.7.
All MDT drift times are measured relative to the trigger signal; a limited trigger timing precision therefore affects the measured MDT resolution. If the trigger time resolution is δt, then the term

$$\sigma_{trig}(r) = \delta t \cdot v_{drift}(r), \quad v_{drift} : \text{electron drift velocity at radius } r$$

has to be subtracted quadratically from the $\sigma(r)$ found with the iterative method to obtain the 'true' single tube resolution. For the test beam setup δt was measured as $\delta t = (1.4 \pm 0.2)\,\text{ns}$. Without a correction this results in resolution values which are too large by up to $15\,\mu$m for small radii r, where v_{drift} is large.

4.4.2 Imposing χ^2-cuts on the track quality

If the resolution is obtained following the above procedure without using an external reference tracker, care needs to be taken when applying selection criteria to the tracks. A cut on the χ^2-value of the fit (equation (4.13)) is useful to reject tracks which are biased by one or more hits being caused by δ-electrons or background photons. The problem with imposing χ^2 cuts is that they can affect the fit extrapolation error ϵ, which is calculated on an event by event basis from the error estimates σ_m and σ_c for the fit parameters m and c; whether this causes a bias in the obtained resolution or not is a priori difficult to judge.

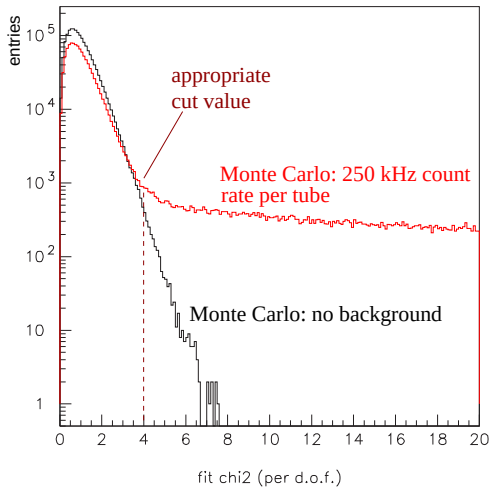

Figure 4.8:
Monte Carlo distribution of the track fit χ^2 with and without simulated photon background. The χ^2 values are normalized to the number of degrees of freedom, i.e. 5 in case of a track defined by 7 hits as for the resolution study. In the presence of a radiation background the distribution shows a long, almost flat tail towards large χ^2-values. The Monte Carlo study showed that for high rate data an appropriate χ^2-cut definition is at the 'kink' in the shown distribution.

The influence of χ^2-cuts on the track fit, as well as other systematic effects, were investigated with a simple Monte Carlo program: Random tracks were generated in the BIS geometry as straight lines within a selected angular range. For each tube intersected by the track, the distance between the track and the wire ('geometric drift radius') r and the corresponding drift time t were calculated. To each r a random number $\sigma(r)$ was added to obtain a 'measured' r'. $\sigma(r)$ followed a Gaussian distribution with mean 0 and an r-dependent width corresponding to an assumed MDT tube resolution. Photons (and δ-electrons) were included into the simulation by throwing a dice on the arrival time (exponential distribution) of the first γ-hit, t_γ. In case $t_\gamma < t$, the arrival time of the photon was reconverted into a drift radius and used as r'. A straight line was fitted to the Monte Carlo hits r' with the help of the same track fitting algorithm used for the experimental data. The Monte Carlo resolution was calculated according to the iterative method described above. The following results were found:

- For data without any radiation background no χ^2-cuts are needed (and no cuts were consequently used in the analysis).

- For Atlas-like background conditions the χ^2 distribution shows a long, almost flat tail towards large values (fig. 4.8). An appropriate choice for an upper χ^2-limit is the value which corresponds to the 'kink' in the distribution (logarithmic plot). With this cut definition the input resolution of the Monte Carlo was correctly obtained back from the simulated data while too loose cuts produced a resolution which was off by up to 20 μm.
  The analysis of the experimental high rate data was consequently done in two steps: First Monte Carlo events with the corresponding background rate were generated and the appropriate χ^2 cut value was determined from the χ^2-distribution; next this value was used as track acceptance criteria in the actual resolution determination.

4.4.3 Results in the absence of background radiation

Figure 4.9 shows the single tube resolution obtained with the GIF radioactive source switched off for different track incidence angles with respect to the chamber. All results

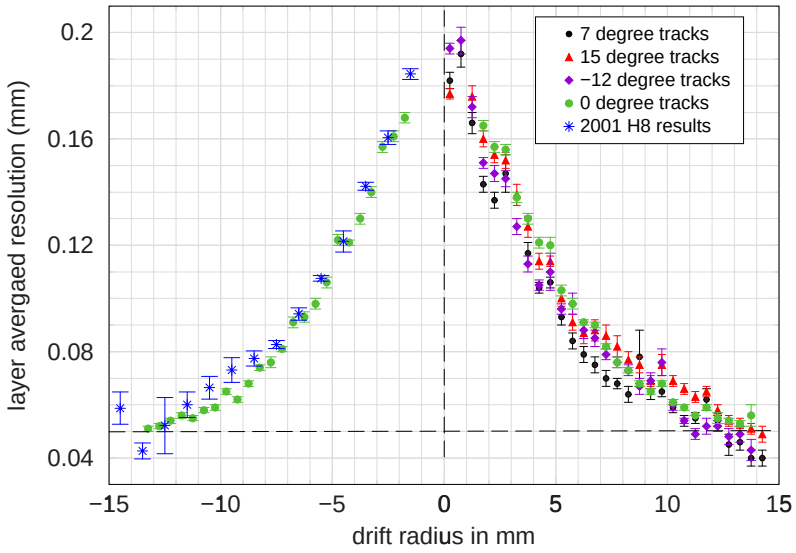

Figure 4.9: Single tube resolution without radiation background. Error bars correspond to the standard deviation calculated from the 8 individual layer results. The right half of the plot shows the resolution curves for different track angles (0^o = tracks perpendicular to the chamber). All curves agree within their errors. The left half compares the obtained results to measurements performed with a different MDT chamber at CERN's H8 beam line in 2001 [19].

are, within their errors, consistent with each other and with the values found in 2001 with a different MDT chamber at the CERN H8 beam line [19].
Resolution values are biggest close to the wire; they decrease by more than a factor 3 when moving towards the tube wall. This behaviour is characteristic for non-linear drift gases like Ar:CO_2 for which the drift velocity decreases with the radius r (fig. 2.8).

Systematic errors: Possible systematic errors in the resolution determination are a wrong rt-relation, deviations from the nominal chamber geometry used in the track fit or an initial resolution curve $\sigma_0(r)$ which causes the iterative procedure to converge against a wrong value. The Monte Carlo program described in section 4.4.2 was used to study the influence of these effects. The following was found:

- Convergence to the correct resolution is not a problem if both BIS multilayers are used for track reconstruction (≥ 7 hits per track). In all cases studied the iterative method reproduced the correct input resolution of the Monte Carlo. The method is less reliable if only one multilayer is used for the analysis.

- A shift of $100\,\mu$m between the two BIS multilayers with respect to each other and a wrong multilayer distance (too large by $200\,\mu$m) were studied as examples for a deviation from the nominal geometry. In the first case the residual distribution is not centered at 0 any longer. No effect on the resolution was observed.
  In the second case tracks which are perpendicular to the chamber ($\phi = 0°$) are not affected while tracks under a large angle are reconstructed with a wrong slope. This causes again an asymmetric residual distribution. The obtained resolution differs from the true one for large radii r; the maximum difference found was $5\,\mu$m.

- A wrong rt-relation was simulated by using

$$r'(t) = r(t) + 200\,\mu\text{m} \cdot \sin(\frac{r - 7.5}{15} \cdot 2\pi),\ r \ \text{ in mm},$$

  instead of the correct $r(t)$. This resulted in an unchanged resolution for $\phi = 0°$ tracks while the obtained resolution for tracks under $\phi = 15°$ is wrong by up to $20\,\mu$m. It should be noted that a bias of $200\,\mu$m in the rt-relation is far larger than what one expects as uncertainty from the autocalibration. For a more realistic bias of $30\,\mu$m the effect on the resolution is negligible ($\leq 5\mu$m).

All systematic effects mentioned have in common that they usually affect tracks under different angles in a different way; the same is true for the individual tube layers. A cross check to exclude any major systematic bias is therefore to compare results obtained for different angles and tube layers. The resolution results presented in this chapter are estimated to be accurate to $\pm 10\,\mu$m.

4.4.4 Results for operation under high background rates

Figure 4.10 shows the single tube resolution for different levels of photon background. Compared to the result without background one observes a deterioration for large radii, which increases with the γ-rate. The degradation is caused by fluctuations in the space charge present in the MDT as a consequence of the photon interactions. In the presence of space charge the electric drift field is modified; this effect is discussed in detail in chapter 5. Variations in the charge present at a given time therefore lead to fluctuations in the drift velocity and consequently to an additional contribution in the tube resolution.

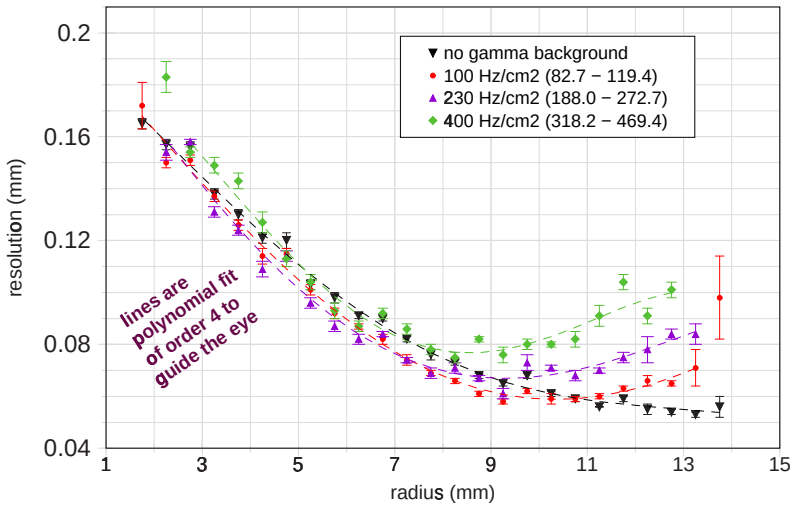

Figure 4.10: Single tube resolution for different levels of photon background. With increasing γ-rate the resolution deteriorates for large drift radii. The stated count rates are the average over the tubes in the beam region. The range of actually found rates due to the non-uniform irradiation discussed in section 4.1 is shown in brackets.

4.5 Single tube efficiency

Besides the tube resolution the MDT efficiency is one of the most important parameters when characterizing the tracking efficiency of the Atlas muon spectrometer. Efficiency studies are also important to verify that no hits are lost in the front end electronics or readout chain.
Two different definitions of efficiency will be used in the following: The so-called **hit efficiency** is the probability that for a muon track crossing the tube at a radius r the MDT registers a hit, irrespective of the measured drift time. For an MDT the hit efficiency is expected to be 1 except for tracks very close to the tube wall[4].
Since for track reconstruction it is not only important to find any hit, but a hit with 'good' position information, a second definition is used. For a muon track crossing the tube at a radius r, the **3σ-efficiency** is the probability that the drift radius r_{drift}, as reconstructed from the drift time t_{drift}, does not differ from r by more than 3 times the single tube resolution. The 3σ-efficiency of an MDT is less than 1 due to the fact that even without any radiation background there is a certain probability for a muon hit to be masked by an earlier δ-electron signal.
Efficiencies were analysed for the 2 innermost tube layers of the BIS chamber, where the track fit extrapolation error is smallest. The correct rt-relation and resolution curves were used for each investigated photon rate. The following procedure was applied:

1. Search for tracks spanning both BIS multilayers, for which at most a hit in one of the innermost layers is missing;
2. Exclude the innermost tubes from the track and fit a straight line to the remaining hits;
3. Interpolate the track to the excluded MDTs and calculate its distance d from their tube centers;
4. Check whether the tubes under study registered any hits and if so, calculate their residuals;
5. Repeat 1. to 4. until all events are processed;
6. For 0.5 mm wide slices in r calculate the hit efficiency as
$$\varepsilon_{hit}(r) = \frac{\#(events\ with \geq 1\ hit\ and\ d = r)}{\#(events\ with\ d = r)}\,; \tag{4.23}$$
7. For the same slices calculate the 3σ-efficiency as
$$\varepsilon_{3\sigma}(r) = \frac{\#(events\ with\ |r_{drift} - d| \leq 3 \cdot \sqrt{\sigma(r)^2 + \epsilon_{fit}^2}\ and\ d = r)}{\#(events\ with\ d = r)} \tag{4.24}$$
where ϵ_{fit} is the extrapolation error of the track fit.

The same Monte Carlo program as for the resolution analysis was used to study the impact of χ^2-cuts on the track fit and the precision of the described method in the case of high background data. An upper limit of 0.01 (1%) was found for the systematic error of the 3σ-efficiencies determined according to the method described above. Statistical errors were calculated as $\sqrt{\varepsilon \cdot (1-\varepsilon)/N}$, where N is the number of tracks used in the analysis.

[4]This is only true if the ASD-lite prototype electronics is used; for the final version the programmable dead time has to be taken into account.

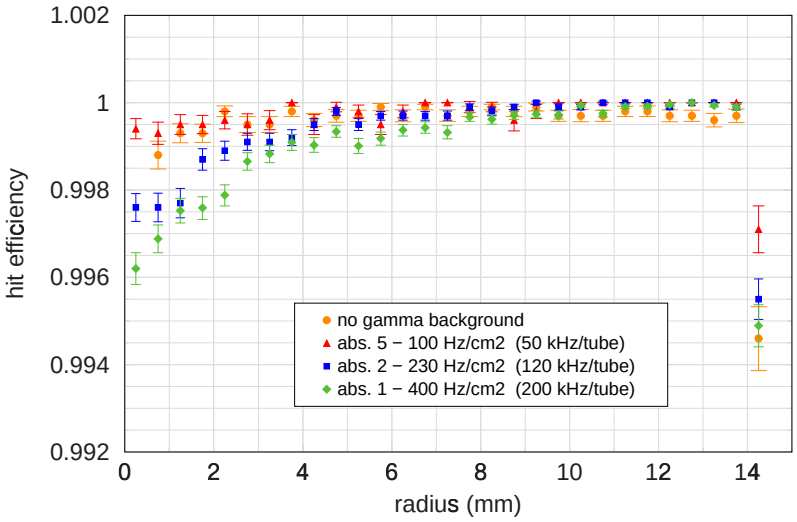

Figure 4.11: Hit efficiency for different background rates. The hit efficiency is, as expected, very close to 1 except for tracks very close to the tube wall. A slight decrease in hit efficiency can be observed close to the wire for increasing photon rates. The cause for this behaviour is not fully understood. The shown error bars are statistical errors only.

4.5.1 Hit efficiency

Figure 4.11 shows the hit efficiency results for different background conditions. The hit efficiency is, as expected, very close to 1 for all radii except very close to the tube wall. A close inspection of the data shows a slight decrease in efficiency near the wire with increasing photon rate. The origin of this behaviour in not fully clear; it cannot be caused by the dead time (< 100 ns) of the front end electronics, since using only events with no hit in the 500 ns preceding the AMT match window yields exactly the same result. A possible explanation is that the effective threshold of the ASD was significantly higher for some events than for the majority. Such a shift in the effective threshold can happen as a consequence of signals with an exceptionally large pulse height, which will lead to a large space charge and thus a drop in gas gain.

4.5.2 3σ-efficiency

Figure 4.12 shows results for the 3σ-efficiency. For all r values the efficiency drops by approximately 8% from an environment with no background to the maximum investigated photon rate of 200 kHz/tube. The average 3σ-efficiency is 0.93 without background and 0.84 for 200 kHz/tube. The probabilities to have at least 3 good hits in a track traversing a chamber with 8(6) tube layers are 0.99997 (0.9996) and 0.9997 (0.993) respectively. An unbiased track fit is therefore possible in almost all cases.
Figure 4.13 shows the residual $r - r_{drift}$ in relation to the track distance r from the tube center for events which were classified as '3σ-inefficient'. One can clearly see that the absolute majority of such events have a positive residual, implying that the real muon hit was masked by an earlier δ-electron or photon signal. The absence of hits in the lower half of the plot (negative residual) is a direct proof that no first threshold crossings were lost by the front end electronics. The group of events with somewhat larger negative residual visible in the region $r < 1$ mm are due to the fact that the residual distribution is no longer Gaussian close to the wire.

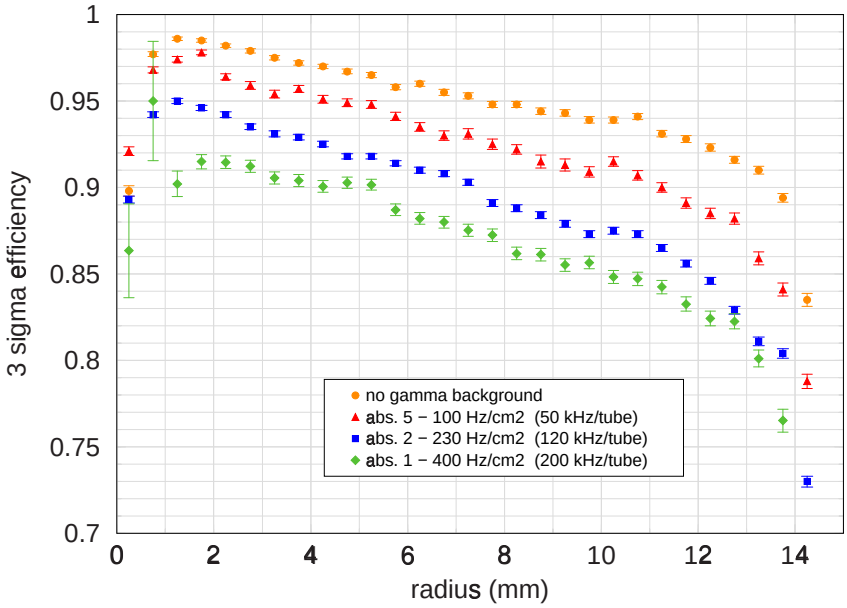

Figure 4.12: 3σ-efficiency for different background rates. The 3σ-efficiency decreases with increasing drift radius r since the probability for a muon hit to be masked by an earlier γ-hit grows with the drift time. The average efficiency is reduced from ≈ 95% in case of no radiation-background to ≈ 85% for the highest photon flux investigated. It should be noted that the decrease in 3σ-efficiency depends on the total tube count rate rather than on the rate per cm^2 as the resolution.

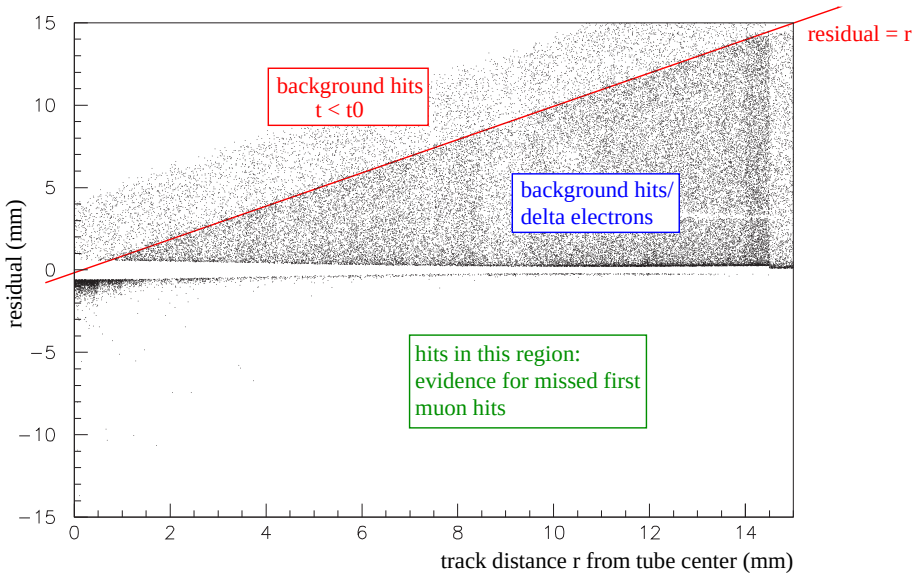

Figure 4.13: Residual plot for 200 kHz average photon count rate. Only hits which are '3σ-inefficient' are plotted. The absence of entries in the lower half of the graph proves that no problems with missed first hits were encountered.

'All truths are easy to understand once they are discovered; the point is to discover them.'
Galileo Galilei, 1564-1642

Chapter 5

Simulation of MDT high rate behaviour

This chapter will concentrate on understanding the reason for the changes in the MDT behaviour observed in a high rate environment. Data from simulating the processes in a drift tube will be compared to the results presented in the previous chapter. Electron transport properties in the operating gas were calculated using the program MAGBOLTZ [26], while HEED [67] was used to obtain the ionization produced by a particle traversing the MDTs. Both HEED and MAGBOLTZ were accessed through the software package GARFIELD [71], version 7.08, which also includes functions to study gas amplification, signal formation and electronics effects.
The way in which space charge produced by background events influences the electric drift field is discussed in section 5.1; models derived here are then used to understand changes in the maximum drift time (5.2), the gas gain (5.3) and the tube resolution (5.4) with the level of background. Section 5.5 presents results on simulating the MDT efficiency.

5.1 Space charge and drift field modifications – steady-state models

Ions produced in the gas amplification region of a drift tube typically need a few milliseconds to reach the tube wall (cathode). If a drift tube is operated under high rates, this leads to the presence of a non-negligible amount of positive space charge and consequently a modified electric drift field $E(r)$. If one assumes the charge density ρ_{ion} to be time-independent (steady-state model), charge conservation leads to the relation

$$\rho_{ion}(r) \sim \frac{\dot{R}_{ion}}{\mu \cdot r \cdot E(r)} \tag{5.1}$$

where μ is the ion mobility and $\dot{R}_{ion}$ the ion production rate. If one makes the additional assumption that $E(r)$ in the presence of space charge deviates only slightly from the standard $1/r$-behaviour, then (5.1) reduces to a constant. In this case $E(r)$ can be calculated directly from Gauss' law $\nabla \cdot E = \frac{\rho}{\varepsilon_0}$; after some rearrangements one arrives at the expression

$$E_1(r) = \frac{V - \overbrace{\frac{\rho_{ion}}{4\varepsilon_0}(b^2 - a^2)}^{\delta V}}{ln\frac{b}{a}} \cdot \frac{1}{r} + \frac{\rho_{ion}}{2\varepsilon_0} \cdot r \tag{5.2}$$

where a is the wire diameter, b the inner tube diameter and V the anode wire potential. For a tube count rate λ per unit length, a gas gain G and $\bar{N}_{p.e.}$ primary electrons per event, the ion density ρ_{ion} is given by

$$\rho_{ion} = \frac{\lambda \cdot G \cdot \bar{N}_{p.e.} \cdot t_{ion}}{\pi \cdot b^2} \quad \text{with} \tag{5.3}$$

$$t_{ion} = \int_a^b \frac{1}{v_{ion}(r)} dr \underset{(2.10)}{=} \int_a^b \frac{p}{\mu \cdot E(r)} dr\,. \tag{5.4}$$

Since the ion drift time t_{ion} itself depends on the electric field, the calculation is performed by iteration.
The assumption that $\rho_{ion}(r)$ is constant is not really necessary to obtain the electric drift field; M. Aleksa et al. [4] showed that (5.1) can be transformed into the differential equation

$$E(r)^2 + r \cdot E(r) \cdot \frac{dE}{dr} = c\,, \tag{5.5}$$

where the constant c is a function of the gas gain, primary ionization per event and background rate. The solution of (5.5) is

$$E_2(r) = \sqrt{c} \cdot \frac{k}{r} \cdot \sqrt{1 + \frac{r^2}{k^2}}\,; \tag{5.6}$$

the constant k is defined by the boundary condition $\int_a^b E(r)dr = V$.
Both models cause a reduction in the drift field close to the wire and an increase in $E(r)$ for $r \gtrsim 6\,\text{mm}$. The influence of the field modification on the maximum drift time is discussed in the next section.

5.2 Changes in the maximum drift time

To simulate the effects of a high background on the electron drift process, an electric field according to (5.2) or (5.6) was implemented in GARFIELD. The maximum drift time was calculated as the average time the 25th electron from a track at $r = 14.5\,\text{mm}$ needed to reach the wire. Additional important parameters used in the simulation are summarized in table 5.1.
Figure 5.1 shows the simulation results in comparison to the experimental data; both models introduced in the previous section for the electric field lead to almost identical predictions. From the simulation one expects a linear decrease in t_{max} with increasing background rate; this agrees well with the observation. The difference in the slope of the measured and simulated relation can be explained by the large uncertainty of 20% in the average number of avalanche electrons created per event, $G \cdot \bar{N}_{e.p}$, which is needed as an input parameter for the calculation of the electric drift field. If $G \cdot \bar{N}_{e.p.}$ is tuned (dashed line in fig. 5.1), the simulation and the experimental results coincide fully.

5.3 Gain drop

The amplitude of muon signals and thus the gain is one of the dominating factors determining the tube resolution close to the wire; understanding effects leading to a loss in gain is therefore crucial when evaluating the MDT performance. From equation (5.2) it can be

Parameter	Value
Gas:	Ar:CO_2 = 93:7
Pressure:	3 bar (abs.)
Temperature:	20^{o}C
Anode wire diameter:	50 μm
Inner tube radius:	14.585 mm
Anode wire potential:	3080 V
Gas gain:	$2 \cdot 10^4$
Primary electrons per photon, $\bar{N}_{p.e.}$:	1285, see equation (4.4)
Equivalent noise charge ENC[1]:	4 primary electrons [61] (resolution simulation)
Discriminator threshold:	25-34 primary electrons (resolution simulation)

Table 5.1: Parameters used in the GARFIELD simulation of an MDT.

[1]The thermal agitation of electrons in a resistor R causes an ever present amount of noise in any electric circuit. The amplitude spectrum of thermal noise is Gaussian with an rms proportional to $\sqrt{TR}$, where T is the temperature. For a MDT the charge which, if input to the ASD, would cause a signal equal to the noise rms is known as equivalent noise charge.

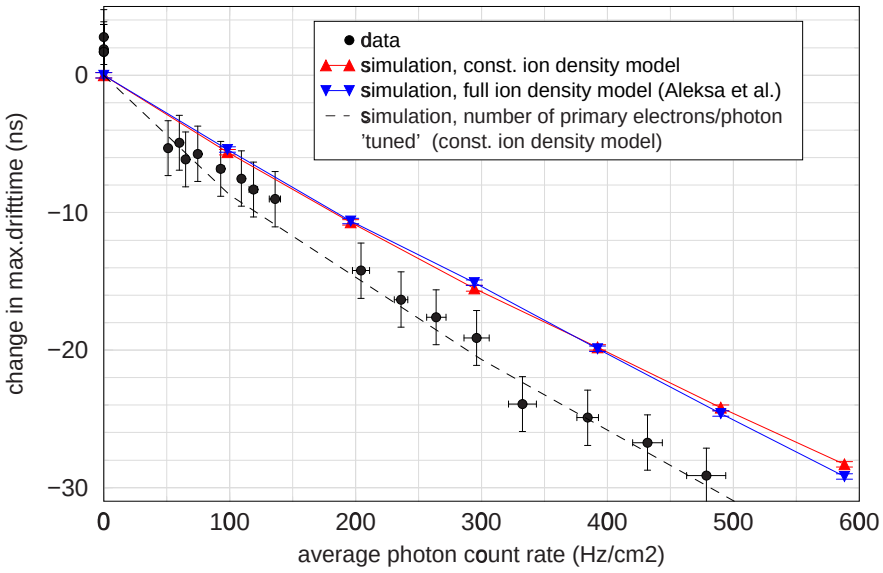

Figure 5.1: Simulation results for the change in t_{max} with background rate due to space charge effects. Both investigated models for the modified electric field yield almost identical drift times. When comparing the simulation to the experimental data one sees that the qualitative behaviour is reproduced correctly, but that the slope is too shallow. This can be explained by the large uncertainty of 20% in the average number of avalanche electrons created per event, $G \cdot \bar{N}_{e.p}$, which is needed as an input parameter for the calculation of the electric drift field.

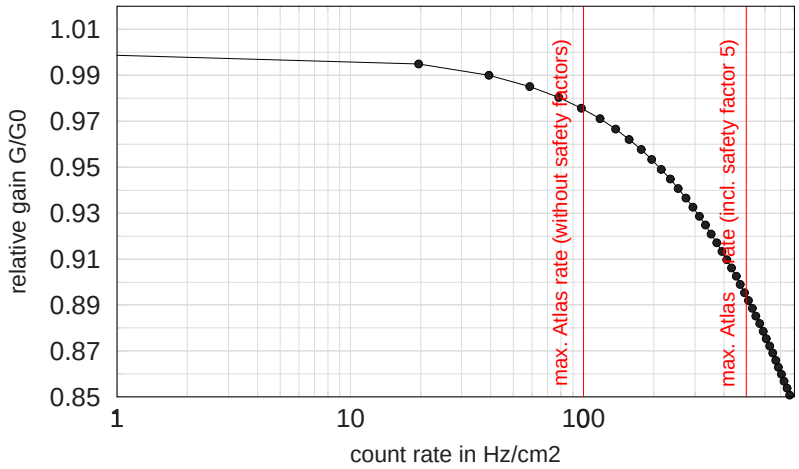

Figure 5.2: Simulation of expected gain drop with background rate. For the highest expected Atlas rates (incl. the safety factor 5) a gain reduction of $\approx 10\%$ has to be envisioned.

seen that close to the wire the space charge from drifting ions effectively reduces the anode wire potential V by an amount δV. The same can be shown to be the case for the E-field E_2 in equation (5.6) by Taylor expansion. Since the gas amplification depends strongly on the applied anode voltage, the result is a reduction in the gas gain G, which increases with background rate. Using Diethorn's formula to relate the change in voltage, δV, to a change in G, the gain drop can be predicted. Figure 5.2 shows such a simulation for Ar:CO_2=93:7 and a nominal gas gain of $2 \cdot 10^4$. For the highest rates expected at Atlas the gain is reduced by 10%. This number is still small enough not to affect the performance (resolution and efficiency) of the MDTs in a significant way, as has been shown in [5].

5.4 Resolution degradation

5.4.1 Resolution when no radiation background is present

To simulate the MDT resolution, muon tracks of 100 GeV tracks were generated in GARFIELD at several fixed distances d from the tube center. Electrons produced by ionization along the muon trajectory were traced step by step until they got to the anode wire taking into account diffusion and electron attachment. A Polya-distribution (2.15) with parameter $\theta = 0.5$ was used to describe the gas amplification process. The induced current signal $I(t)$ on the anode was calculated according to Ramo's theorem (2.16) from the movement of the ions produced in the gas amplification. The ion motion was obtained for every point $\vec{r}$ in space according to the electric field $\vec{E}(\vec{r})$ from the ion mobility data shown in section 2.2.3.
The signal propagation along the anode wire and the properties of the front end electronics (ASD) were taken into account by folding the raw current signal $I(t)$ with the response functions of an MDT and the ASD-lite amplifier-shaper circuit. The outcome of this approach, which is described in more detail in appendix A, is a voltage signal $V(t)$ as seen by the discriminator. In a last step the time t_1 at which a given threshold is crossed by the signal for the first time is calculated. Electronics noise can be included in the simulation by adding a random number to the nominal threshold for each event. After all tracks

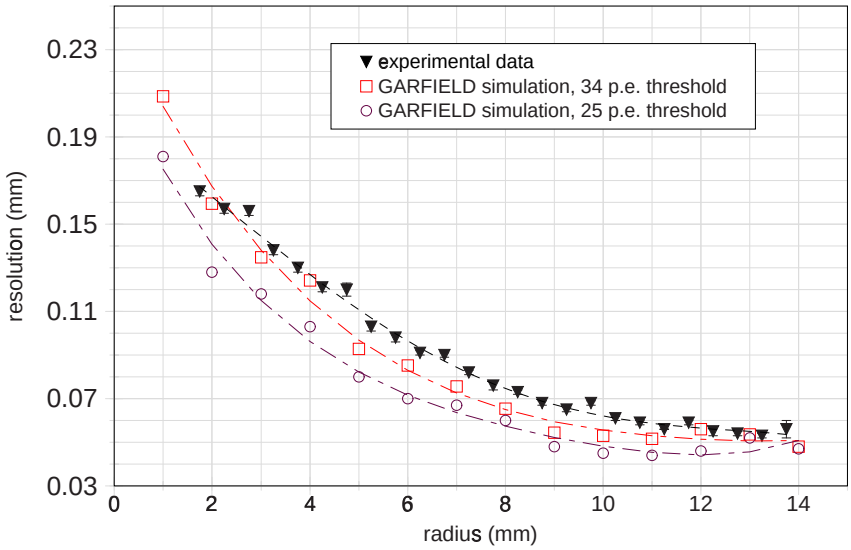

Figure 5.3: GARFIELD simulation of the MDT resolution with no radiation background present. The filled triangles correspond to the experimental data (section 4.4.3). Open symbols are simulation results for two different threshold choices (25 and 34 primary electrons).

for a given distance d from the wire have been computed, the single tube resolution $\sigma(d)$ is obtained as the product of the width σ_{t1} of the t_1 distribution (Gaussian fit) and the electron drift velocity $v_{drift}(d)$.
The resolution curve obtained with the simulation procedure described above is shown in figure 5.3 for two different thresholds together with the experimental result. At the time at which the measurements presented in chapter 4 were carried out, a threshold of 25 primary electrons (Atlas default) was believed to correspond to an ASD threshold of 60 mV which was used as the nominal setting. Only later did it turn out that this is incorrect with the true threshold in terms of primary electrons being higher than assumed. If the threshold parameter in the simulation is set to 34 primary electrons, the experimentally obtained and the simulated data agree to $\pm 10\,\mu$m.

5.4.2 Resolution change under high rates

In a high rate environment the resolution of drift tubes is affected in several ways: For a non-linear drift gas like Ar:CO_2 the dominant contribution is a space charge distribution which varies with time, different from the simple steady-state models introduced in section 5.1. The consequence are fluctuations in the electric drift field which in turn have an impact on the electron drift process. Additional effects are the gain drop discussed in section 5.3 as well as fluctuations or a shift of the amplifier baseline which imply a change in the effective discriminator threshold.
All the effects listed except for the field fluctuations lead to a worse resolution mainly for small radii, as has been confirmed by modifying the corresponding parameters in the GARFIELD simulation described in the previous paragraph. For the highest investigated rates of $\approx 400\,\mathrm{Hz/cm^2}$ the expected gain loss is 9% while for the amplifier baseline shift an upper limit of 3 primary electrons was found. The change in the expected resolution is below $5\,\mu$m, in agreement with the experimental data.

Modelling field fluctuations

Two different methods were used in the past to incorporate fluctuations of the drift field into the simulation of the MDT behaviour. G. Scherberger [66] started with a detailed numerical analysis of the spatial movement of the ion cloud produced by a single 1-hit event with time. After the shape and position of an ion cloud produced at time t_1 was known for all $t > t_1$ from this preparatory study, a Monte Carlo method was used: for a muon at time t_μ the time of the last (t_{-1}), last but one (t_{-2}), last but two (t_{-3}),.... gas amplification processes was generated from exponential distributions until $t_\mu - t_{(-i)}$ was larger than the maximum ion drift time of approximately 4 ms. For each such 'bygone' event, the position and shape of the ion cloud at time t_μ was calculated. The ion clouds were then approximated by a number of point charges and their electric field superimposed to the standard $1/r$-field. As a final step the drift of electrons created at a given distance d from the wire in the now 'frozen' field configuration ($v_{ions} \ll v_{drift,e}$) was studied by numerically integrating the drift velocity calculated beforehand with GARFIELD.
A simpler approach has been chosen by M. Aleksa et al. [4], keeping the radial-symmetric, steady-state model for the electric field introduced in section 5.1, but allowing the total amount of space charge (i.e. the constant c in equation (5.5)) to vary. This is based on the assumption that the electric field a drifting electron 'sees' is not influenced by ions located far away but only by ions in a slice of thickness Δx in wire direction. Δx was chosen as 1 cm. For each event the total charge found per unit length was taken as $n \cdot \bar{N}_{p.e.}$ with n following a Poisson-distribution with mean

$$\bar{n} = (Rate\ per\ \Delta x) \cdot (max.\ ion\ drift\ time)\,.$$

n can be interpreted as the number of ion clouds per cm; $\bar{N}_{p.e.}$ is the average number of electron-ion pairs created per photon interaction. For the maximum expected rate at Atlas, 500 Hz/cm^2, $\bar{n}$ is around 5.
There are several weak points in this model:

- While it is true that the contribution of ions far 'down' the wire to the field a drifting electron actually sees is negligible, the width Δx of the region in which ions do have an influence depends on the radial position r of the electron (r small $\rightarrow \Delta x$ small).
- Simulations with a space charge ring show that the electron drift time for a given radius depends not only on the total amount of ions, but also on their position. This additional contribution to the field and consequently to the drift time fluctuations is suppressed in the method described.
- For photons which interact by Compton-scattering, the deposited energy and thus the created space charge do not have fixed values. Fluctuations in the number of created ions per γ-hit increase the field variations, but are not taken into account in the model.

Nevertheless this second, simpler model was chosen in this thesis in order to arrive at a theoretical prediction which can be compared to the experimental results. The reason for this choice is that a detailed simulation of the spatial movement of the ion clouds, as in the method described first, only makes sense if the initial charge distribution after the ionization of the gas by a particle is known. This is relatively straight forward if the high rate environment is created by an intensive muon beam itself as in [66]; in this case the distribution of the primary electrons created by ionization along the trajectory can

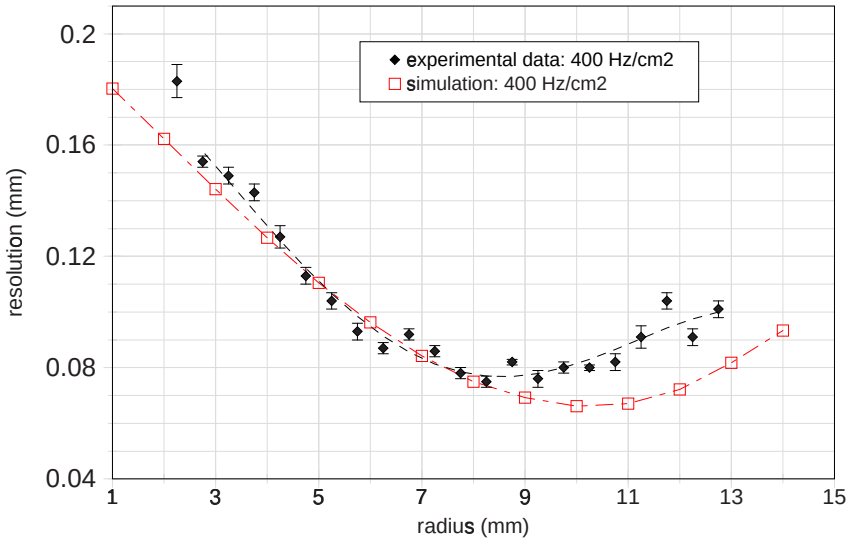

Figure 5.4: Simulated resolution degradation due to field fluctuations, according to the simplified model described in the text. The agreement with the experimental data is qualitative only.

be parametrized from the beam profile. For the measurements of chapter 4 the situation is different in so far as the high level of background was generated by the ^{137}Cs photon source of GIF; the muon beam itself had a very low intensity. As has been pointed out already in the section about ionization of chapter 2, the ^{137}Cs photons interact with an MDT mainly by Compton scattering, which makes a parametrization of the initial space charge distribution difficult.
Figure 5.4 shows the simulation results for the simple model and a background rate of 400 Hz/cm^2. Only field fluctuations have been simulated; their contribution to the resolution was then added quadratically to the experimental resolution values in case of no background. The model predicts a loss in resolution for large radii only, as is indeed found from the experimental data. The quantitative agreement with the experimental data is less good, field fluctuations in reality seem to be larger than the ones assumed in the simulation.

5.5 Efficiency loss

As has been explained in section 4.5, the 3σ-efficiency of a drift tube decreases with increasing drift radius r due to the production of δ-electrons which in some cases will mask the true muon hit. With an increasing level of background radiation the degradation in 3σ-efficiency grows, since in this case a true signal can not only be hidden by a δ-electron, but also by a photon hit. The loss in efficiency for high rates is a purely stochastic phenomenon; contrary to all other, space charge related, effects described so far it depends on the overall tube count rate and not on the rate per cm^2.

5.5.1 3σ-efficiency when no radiation background is present

Calculating the efficiency in case of a negligible amount of background requires to simulate the production of δ-electrons and their subsequent interaction with the operating gas. The

Monte Carlo program GEANT3 [42] was used for this purpose; the results presented here were obtained in collaboration with Serguei Baranov from Freiburg University. Muon tracks were generated for several fixed distances r from the anode wire. δ-ray production was taken into account by using the cross section given in formula (2.8). Each δ-electron was traced step by step to find its closest point P to the anode A. An event was counted as $n \cdot \sigma$-inefficient (with typically $n = 3$ or 5), if the distance $\overline{AP}$ was smaller than r by more than n-times the single tube resolution $\sigma(r)$. More details with respect to the method used can be found in [23].

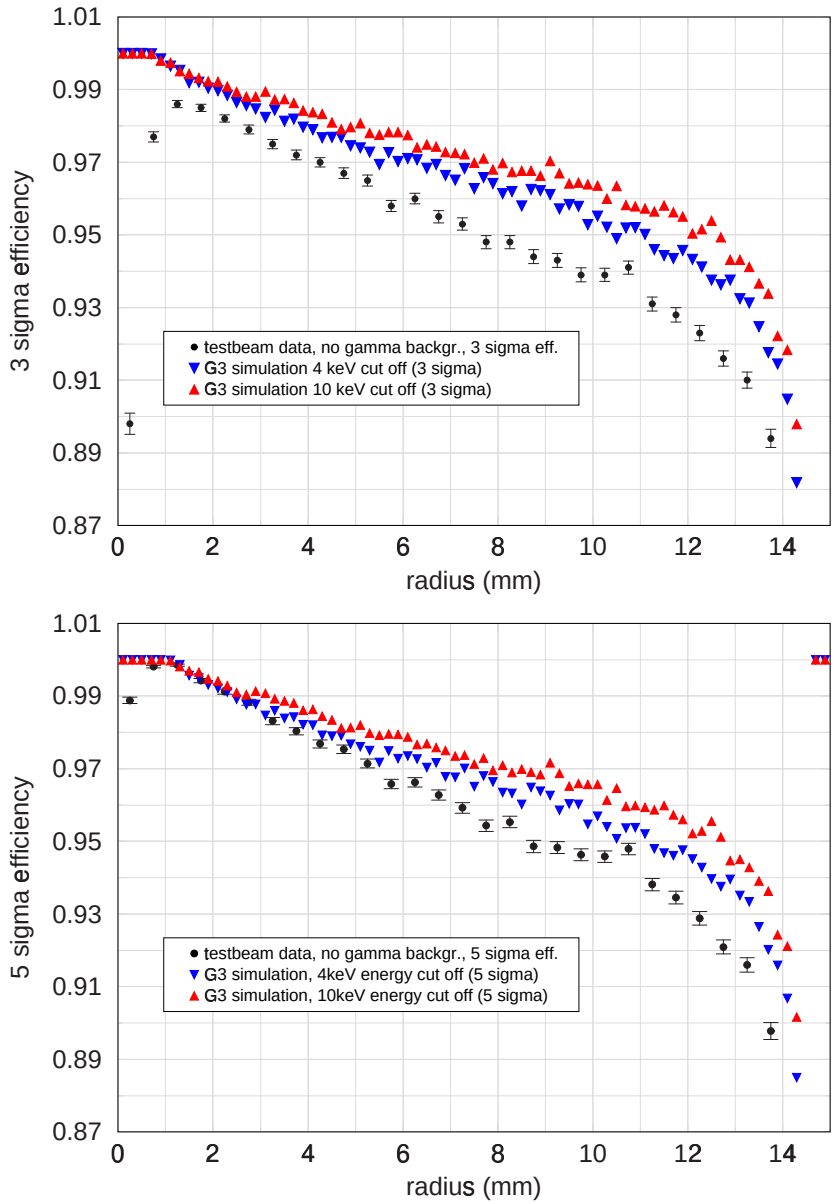

Figure 5.5: GEANT3 simulation results for 3σ-efficiencies (top) and 5σ-efficiencies (bottom) in the case of no photon background. One clearly sees that the Monte Carlo results depend on the energy cut-off value to which δ-electrons are traced. The agreement of the simulation done with an energy cut off of 4 keV and the experimental results is on the 0.5-1% level.

The simulation results together with the efficiency curve obtained from the X5 data are shown in figure 5.5 for both 3σ and 5σ efficiency definitions. The simulation results depend on the energy cut-off value used for tracing the produced δ-electrons in GEANT3. This is understandable if one takes into account that an electron energy of 10 keV in argon at 3 bar absolute pressure corresponds to a range of approximately 900 μm [54], which is far larger than the tube resolution. Using a 10 keV cut-off some MDT hits with an associated δ-electron will be classified wrongly as 'efficient' only because the electron was not traced far enough. In this case the calculated residual stays below the 3σ (5σ) threshold in the simulation, but may not do so in reality. After this was realized, the energy cut-off was reduced to a more appropriate value of 4 keV.
The simulation results further reproduce the data better for a 5σ than for a 3σ efficiency definition. One possible explanation for this is that the Monte Carlo does not take into account the intrinsic tube resolution. In total it can be said that the simulation predicts the same qualitative behaviour as found experimentally; the quantitative agreement is on the level of 0.005-0.01, which is acceptable compared to the estimated uncertainty of 0.01 (1%) in the experimental results.

5.5.2 3σ-efficiencies under high rates

For the simulation of the 3σ-efficiency $\varepsilon(r)$ expected for a given rate, the inefficiency due to δ-electrons was taken as the experimentally obtained curve for no radiation background. If the probabilities for a muon hit to be masked by a δ-electron and a photon are $\bar{\varepsilon}_\delta$ and $\bar{\varepsilon}_\gamma$ respectively, then the overall inefficiency $\bar{\varepsilon}$ can be calculated from

$$\bar{\varepsilon} = \bar{\varepsilon}_\delta + \bar{\varepsilon}_\gamma - \bar{\varepsilon}_\delta \cdot \bar{\varepsilon}_\gamma \,. \tag{5.7}$$

To be fully correct a third type of inefficiency has to be included, namely the case in which a muon hit is masked by a secondary threshold crossing of a photon event occurring shortly before the start of the AMT match window (fig. 5.6). If the probability for this to happen is $\bar{\varepsilon}_m$, then (5.7) becomes

$$\bar{\varepsilon} = \bar{\varepsilon}_\delta + \bar{\varepsilon}_\gamma + \bar{\varepsilon}_m - \bar{\varepsilon}_\delta \cdot \bar{\varepsilon}_\gamma \; - \bar{\varepsilon}_\delta \cdot \bar{\varepsilon}_m - \bar{\varepsilon}_\gamma \cdot \bar{\varepsilon}_m + \bar{\varepsilon}_\delta \cdot \bar{\varepsilon}_\gamma \cdot \bar{\varepsilon}_m \,. \tag{5.8}$$

Obtaining $\bar{\varepsilon}_\gamma$: Assume the background count rate is R_γ. For a distance r of a muon track from the wire the 3σ-inefficiency due to a photon hit masking the muon signal is given by

$$\bar{\varepsilon}_\gamma(r) = 1 - e^{-\lambda} \quad \text{with} \tag{5.9}$$

$$\lambda = (t_{drift}(r - 3 \cdot \sigma(r)) + t_0) \cdot R_\gamma \,. \tag{5.10}$$

t_{drift} is the drift time corresponding to a radius of $r - 3 \cdot \sigma(r)$, σ is the single tube resolution and t_0 is the leading edge of the TDC spectrum with respect to the start of the AMT match window, t_{start}. λ can be interpreted as the average number of photon hits in the time interval $[t_{start}, t_{drift}]$.

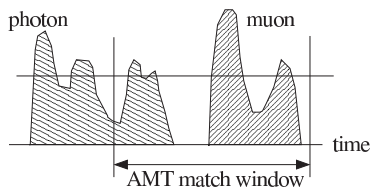

Figure 5.6:
Inefficiencies introduced by secondary threshold crossings. The photon event occurring shortly before the start of the AMT match window 'spills over' into the match window and masks the later muon hit.

Obtaining $\bar{\varepsilon}_m$: The inefficiency due to multiple threshold crossings is obtained in a separate Monte Carlo simulation in the following way:

1. From a calibration data run get the probability distribution for the number of threshold crossings for photon events, P_n (fig. 5.8).
2. From the same data get the conditional probability distributions $P(t_k|n)$, $k \leq n$ for the arrival time of the k-th threshold crossing if the total number of threshold crossings was n (fig. 5.9).
3. For the $t_{max} \approx 700\,\text{ns}$ long interval $[t_{start} - 700\,\text{ns}, t_{start}]$ throw a dice on the number of photon events using a Poisson-distribution with mean $\lambda = R_\gamma \cdot 700\,\text{ns}$.
4. For each such event determine its time in the interval $[t_{start} - 700\,\text{ns}, t_{start}]$ from a uniform distribution.
5. For each photon event determine the number of threshold crossings n as a random number drawn from the P_n distribution.
6. For each of the n threshold crossings get its arrival time as a random number following the $P(t_k|n)$ distribution introduced above.
7. Check if at least one of the threshold crossings lies in the interval $[0, t(r - 3\sigma(r))]$; if so, count the event as inefficient.
8. Calculate $\bar{\varepsilon}$, as the ratio between the number of inefficient events and the number of events simulated in total.

Figure 5.7 shows the 3σ-efficiency curves calculated according to this method for different background rates. The agreement with the experimental data is good for photon rates of

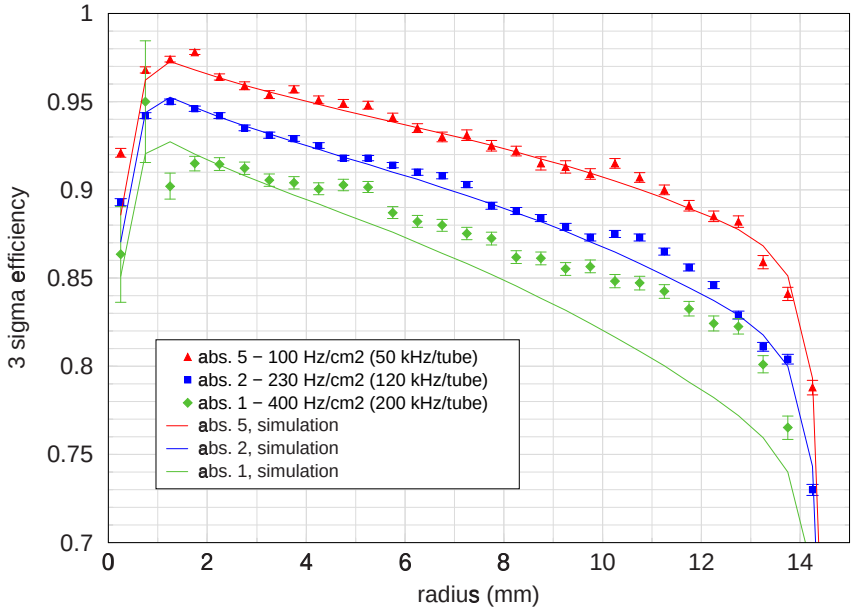

Figure 5.7: 3σ-efficiency obtained with the simulation procedure described in the text. The agreement with the experimental data is good for photon rates of 100 Hz/cm^2 and 230 Hz/cm^2; it is less good for the highest investigated average photon flux of 400 Hz/cm^2.

100 Hz/cm^2 and 230 Hz/cm^2; it is less good for the highest investigated average photon flux of 400 Hz/cm^2, where the measured efficiency is higher than the predicted one. The most likely reason for this behaviour is a slightly wrong assumed photon count rate. The definition of the exact count rate to be used in the simulation is problematic due to the non-uniformity in the γ-background described in section 4.1, and the fact that the experimental efficiency curves are averaged over 17 tubes for better statistics.

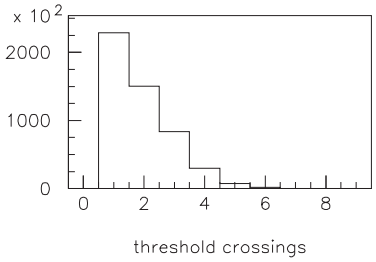

Figure 5.8:
Probability distribution P_n for the number of threshold crossings for a photon event with the ASD-lite electronics, as found in a special calibration run.

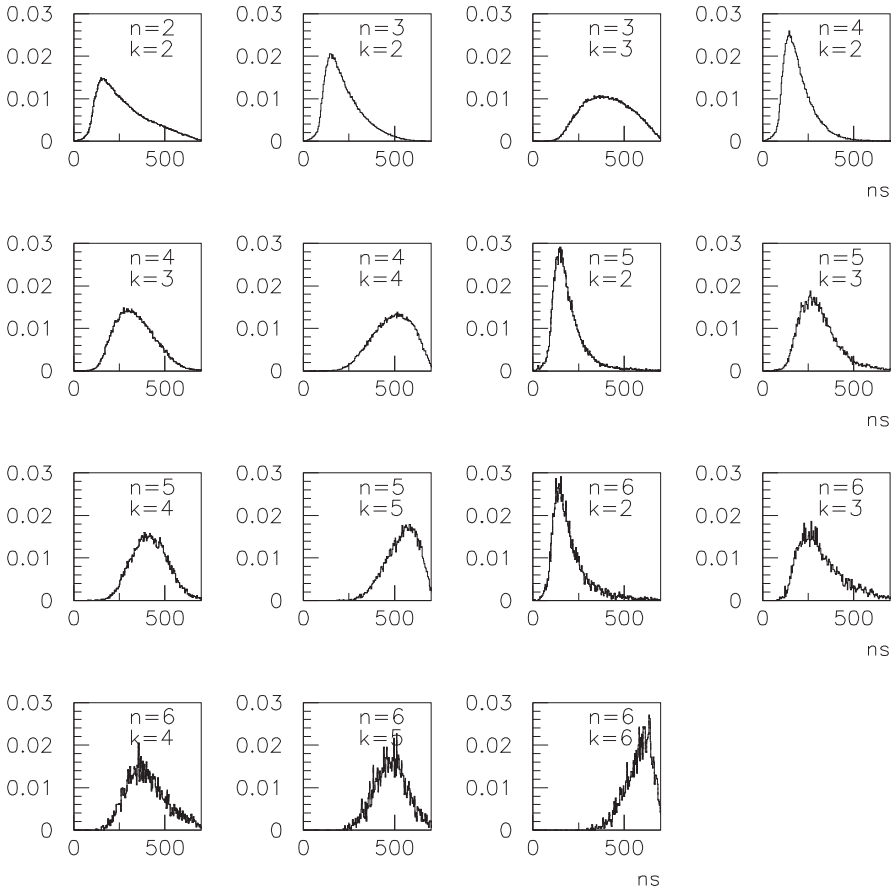

Figure 5.9: Distributions $P(t_k|n)$ for the timing of the k-th threshold crossing relative to the first one for a photon event with a total of n threshold crossings. One can see that for fixed n the distributions are shifted to later times with increasing k; on the other hand the distributions are shifted towards earlier times for fixed k and increasing n.

'By three methods we may learn wisdom: First by reflection, which is noblest; second, by imitation, which is easiest; and third by experience which is bitterest.'

Confucius, 551 – 479 B.C.

Chapter 6

Ageing studies

Due to the complexity of the Atlas detector design, exchanging muon chambers after some years of operation in case of a failure will be impossible, or at the very least, extremely time consuming and difficult. A careful study of the factors limiting their lifetime is therefore essential. For drift tubes typical symptoms of a performance degradation with time are losses in gas gain, a decrease of resolution or efficiency, excessive currents and the formation of sparks. The various effects are often summed up in the expression 'ageing'; in a stricter sense ageing refers to changes in a drift tube that are

- radiation induced,
- not reversible by a simple gas exchange,
- affecting the tube operation.

This chapter discusses the results of ageing studies carried out at GIF with the same MDT chamber as used for the high rate performance measurements presented in chapter 4. The focus was on the test of a full MDT chamber, built from final Atlas components, and operated with gas recirculation; in this the conditions differed significantly from previous ageing studies which were typically performed with single tubes in a dedicated laboratory setup and with a simple flushing gas system.
Section 6.1 gives an overview over different mechanisms of wire chamber ageing while 6.2 summarizes the conditions during the study presented here, which had to be split into two periods, 'Age1' and 'Age2', as already pointed out in chapter 3. Section 6.3 reviews the methods used in the analysis of the data while 6.4 is dedicated to a discussion of systematic uncertainties and errors. The results for MDTs operated with and without gas recirculation (BIS multilayers 1 and 2) are presented in sections 6.6 and 6.5 respectively. The chapter closes with results from various chemical and surface analyses performed on samples taken both from the MDTs and from the gas system (section 6.7).

6.1 Mechanisms of wire chamber ageing

Ageing effects observed in wire chambers are normally due to deposits on either the anode or the cathode surfaces. Already thin coatings on the anode wire, which can be either electrically insulating or not, lead to a loss in gas gain. As an example, consider an MDT wire with an original diameter of 50 μm which is increased by 2 μm due to the deposition of a conducting film of material; by substituting the different radii into Diethorn's formula (2.13) and using the Diethorn parameters for Ar:CO_2=93:7, as specified in equation (2.14),

one finds a corresponding gain reduction of 23%. More detailed calculations, also for the case of non-conducting layers, can be found in [50].
Deposits on the cathode have no direct impact on the gas gain; they can however be the cause for spontaneous discharges and self-sustained currents via a mechanism known as the Malter effect [52]: If the cathode is coated by a thin film of insulating material, the neutralization of positively charged ions, produced either by a traversing particle or in the gas amplification process, is impeded. A positive space charge builds up at the boundary between the insulating layer and the operating gas of the drift tube; the consequence is an electric field perpendicular to the cathode surface which can be strong enough for electrons to be liberated from the cathode material by field emission. These electrons then drift to the anode wire where they undergo gas amplification, producing more ions which in turn move towards the cathode, contribute to the space charge and close the cycle. The result is a self-sustained current; once the Malter effect manifests itself in a drift tube, its use for particle detection is very limited due to the large number of (fake) pulses and the degradation of the electric drift field caused by the large number of drifting ions.
Deposits, especially on the anode, can take the form of whiskers, droplets or a uniform coating; they can be both solid or liquid, brittle or viscous [47]. One generally assumes that their formation is a polymerization process which involves either the molecules of the operating gas itself or a contaminant. In both cases the deposition of material on the wire surface competes with etching or ablation effects [72]. Etching in this context is the process in which molecules are transferred from a solid phase (wire deposit) into the gas phase by a bombardment with electrons (from the gas amplification). In particular mixtures containing fluorine, e.g. in the form of CF_4, are known for their large potential for removing material from the anode wire of drift tubes; they are therefore sometimes deliberately used to prevent chamber ageing [57] or as a cleaning gas [30]. Ageing effects can in some cases also be avoided by adding water or an alcohol to the gas mixture [70]. The mechanism by which these additives work is not yet fully understood. Since the ionization potential of most alcohols A is relatively low, one may speculate that charge transfer reactions $X^+ + A \rightarrow A^+ + X$ play a role by neutralizing a molecular ion X^+ in a more 'gentle' way than by the recombination process $X^+ + e^- \rightarrow X$ taking place at the cathode, with the result that the molecule is prevented from breaking up. Water on the other hand might produce radicals of the form H–O·, which can saturate the polymerization process before chains become so long that they are no longer volatile and attach themselves to the cathode or, with greater harm, to the anode.

Ageing due to polymerization of the operating gas

Most drift detector gases containing hydrocarbons tend to polymerize under high irradiation. A hypothetical polymerization reaction, showing the involved processes and starting from methane, is

$$CH_4 + e^- \rightarrow CH_3\cdot + H\cdot + e^- \quad (1a)$$

$$CH_4 + e^- \rightarrow CH_2\!: + H_2 + e^- \quad (1b)$$

$$CH_2\!: + CH_2\!: \rightarrow C_2H_4 + 2\,H_2 \quad (2)$$

$$CH_3\cdot + C_2H_4 \rightarrow C_3H_7\cdot \quad (3a)$$

$$C_3H_7\cdot + C_2H_4 \rightarrow C_5H_{11}\cdot \quad (3b)$$

$$\vdots$$

$$C_nH_{2n+1}\cdot + H\cdot \rightarrow C_nH_{2n+2} \quad (4a)$$

$$C_nH_{2n+1}\cdot + C_mH_{2m+1}\cdot \rightarrow C_{n+m}H_{2(n+m)+2}\ . \quad (4b)$$

In (1) a methane molecule loses one or two of its hydrogen atoms due to the bombardment with electrons. The result is a radical with at least one unpaired electron, denoted by the '·', in the shell of the C-atom. Radicals are a very reactive species; they try to reach a stable, i.e. saturated, electron configuration by forming chemical bonds. The product of reaction (2) is the chemical compound ethylene, C_2H_4, in which two carbon atoms are connected by a double bond (C=C). Both free radicals and molecules with a double (or triple) bond are needed for the actual polymerization process (3): The unpaired electron of the radical and one of the electrons from the C=C double bond form a new single bond; the radical gets attached to the molecule which grows in size. The result of many such reactions is a hydrocarbon chain whose overall length is determined by the frequency with which one of the termination processes (4) occurs. Hydrocarbons above a certain size are normally non-volatile; if this size is reached in a drift detector, they will condense on the available surfaces which leads to the deposits responsible for ageing.

Scaling laws: Laboratory ageing studies are normally performed on a time scale far smaller than the lifetime one requires of a detector. This immediately raises the question how to extrapolate ageing rates from one set of conditions ('ageing test') to another ('LHC'). From reaction (1) in the above example it is clear that the start of the polymerization process depends on the creation of free radicals from gas molecules via electron bombardment. One therefore expects that the degradation of a chamber is a function of the amount of irradiation it was exposed to rather than the time of operation.
The most common way to specify detector ageing is as gain loss per accumulated charge, independent of the actual irradiation time t_{irrad}; this implies that the formation of deposits is proportional to $\dot{Q} \cdot t_{irrad} \equiv \lambda \cdot G \cdot \bar{N}_{p.e.} \cdot t_{irrad}$, where λ is the tube count rate per cm wire length, G is the gas gain and $\bar{N}_{p.e.}$ is the average number of primary electrons per interaction. This assumption is not without weaknesses: While the concentration of monomer radicals ($CH_3\cdot$ in the above example) should indeed be proportional to $\dot{Q}$, the actual polymerization reactions (3) involve more than one species of molecules or radicals, which first have to be produced in the gas by the gas amplification process. The reaction rate is thus not necessarily linear in $\dot{Q}$, in particular if recombination and etching effects are additionally taken into account.
Another important point is how the ageing of a drift tube scales with the gas flow, which can often be adjusted over some range. Here one usually assumes that the ageing rate is lower for a higher flux. This is however only true if the formation of deposits involves long-lived or stable molecules as interim stages, like ethylene in the methane example, with a lifetime comparable to the time they stay in the detector volume.
Both with respect to scaling for a faster charge accumulation rate or for different gas flows one can state as a general rule: 'The more different the conditions during an ageing test, the larger the uncertainty in the interpretation of its outcome'.

MDT ageing studies performed in the past: Many attempts were made to find an MDT operating gas on the basis of argon and methane or ethane [41],[59],[73]. Such mixtures have the advantage of a linear rt-relation, i.e. an electron drift velocity that is independent of the electric field, gas pressure and temperature; in this case field fluctuations

caused by a high radiation background do not affect the tube resolution, as pointed out in section 5.4.2. Methane is moreover a very effective quenching gas without the drawback of a considerable increase in the maximum drift time, as encountered for CO_2.
For a long time the mixture Ar:CH_4:N_2=91:5:4 was the baseline gas for Atlas [13], until ageing studies showed that an MDT lifetime of 10 years under LHC conditions could not be reached with this composition [49],[69]. The modified mixture Ar:CH_4:N_2:CO_2=94:3:2:1 was more promising; in the end it was however equally discarded as a choice for Atlas since in this case the appearance or non-appearance of ageing strongly depended on the exact operating conditions like the gas flow or the size of the irradiation zone [60], [50].
Ar:CO_2=93:7 was extensively tested for ageing in different laboratory setups using single drift tubes. It proved to be very radiation resistant; no degradation in MDT performance was observed up to charges well above the 0.6 C/cm required for Atlas [48]. The absence of polymerization processes was the main factor in it becoming the final MDT operating gas, despite a non-linear rt-relation and the relatively large maximum drift time of 700 ns.

Ageing due to contaminants

Practically every drift detector contains non-metallic components which harbour the risk of polluting the operating gas. The main mechanisms by which contaminants are produced are

- Outgassing: Plastic materials often contain traces of non-polymerized monomers left from their production. Since these are not firmly bound to other molecules they can over time evaporate from the material. Outgassing can be particularly severe in glues, if they are not cured properly, and in plastics containing softeners.

- Dissociation and material breakdown under irradiation: Chemical substances that are very stable under normal conditions can rapidly deteriorate if they are exposed to ultraviolet or ionizing radiation. In the case of organic compounds, this will mainly lead to the outgassing of H_2, though a substantial amount of heavier and more deadly molecules can also be produced. Certain chemical groups increase the radiation resistance of a material. Among them are aromatics[1] like the phenyl group -C_6H_5. These groups can absorb large excitation energies and hence prevent a molecule from breaking up; the yield for the production of radicals is low. Examples for plastic materials suitable for use in a high radiation environment are polyimide (Kapton®) and polyether-ether-ketone, PEEK [64].

- Evaporation: Valves in a detector gas system are often greased to prevent them from getting stuck. Soft sealants are used to achieve gas tightness and oils may be present in bubblers to monitor the gas flow. In each of these cases molecules will evaporate from the surface of the liquid or (semi)solid material until the concentration in the gas phase equals the vapour pressure of the given substance.

- Improper cleaning: A variety of oils, lubricants and cooling fluids is used in the production and machining of both plastics and metals. They have to be thoroughly removed from the components of a drift detector before its assembly in order to avoid uncontrolled contamination of the operating gas.

[1] Aromatics are chemical compounds containing one or more benzene rings.

From the above list it is evident that materials used in the construction of gaseous detectors to be operated under high rates need to be carefully chosen in order to guarantee an adequate lifetime. The mechanism by which contaminants cause ageing in a wire chamber is, as in the case of ageing due to the operating gas, the formation of deposits either on the anode or the cathode. Molecules with a large dipole moment are attracted to the anode wire by the inhomogeneous electric drift field. If they are heavy, they can stick to the wire surface and gradually build up an insulating or conducting layer of material. Once attached to the wire they are exposed to an intense bombardment with electrons from the gas amplification process. In many cases they will therefore polymerize and form heavily crosslinked macro-molecules.
If ageing is caused by a pollutant, it is not guaranteed that a higher gas flux will reduce the effect. On the contrary, the growth rate of a deposit will increase with the gas flow if the probability for impurities to be captured by the anode wire is high, since in this case a larger number of molecules is transported into the detector volume in a given time [30].
An element found as a deposit on the anode wire in numerous ageing studies is silicon (Si). Silicon belongs to the same group of the periodic table as carbon. Their chemical reactions are therefore similar; Si however rarely forms double or triple bonds. Silicon can polymerize both with carbon and with oxygen. The result are macro-molecules with either

$$\begin{array}{ccccccccc} & | & & | & & | & & & \\ -\,\mathrm{Si}\,- & \mathrm{O} & -\,\mathrm{Si}\,- & \mathrm{O} & -\,\mathrm{Si}\,- & & \text{or} & & \\ & | & & | & & | & & & \end{array} \qquad \begin{array}{ccccccccccc} & | & & | & & | & & | & & | & \\ -\,\mathrm{Si}\,- & \mathrm{C} & -\,\mathrm{Si}\,- & \mathrm{C} & -\,\mathrm{Si}\,- & & & & & & \\ & | & & | & & | & & | & & | & \end{array}$$

as their backbone. A 3-dimensional cross-linking is also possible. The simplest, purely inorganic structure in this case is $(SiO_2)_n$, which has a crystalline consistency and is found in silica glass and sand.
Silicon has a very high affinity for deposition on the anode of a drift chamber [31]. In [44] on average 0.008 Si-atoms were found on a 20 μm thick wire for every electron produced in the gas amplification process. Other studies showed that for a setup in which two drift tubes were connected in series, the first totally absorbed a low level silicon contamination; no ageing was observed in the second one [3].
Silicon atoms found in a drift chamber usually stem from silicone materials, which are either used in its construction or present in the gas system. Silicones are chemical substances in which organic compounds are attached to a $(\text{–Si–O–})_n$ chain. The most basic silicone is poly-dimethyl-siloxane $(Si(CH_3)_2O)_n$,

$$\begin{array}{ccccccccccc} & & \mathrm{CH_3} & & \mathrm{CH_3} & & \mathrm{CH_3} & & \\ & & | & & | & & | & & \\ -\,\mathrm{O}\,- & \mathrm{Si} & -\,\mathrm{O}\,- & \mathrm{Si} & -\,\mathrm{O}\,- & \mathrm{Si} & -\,\mathrm{O}\,- & & \\ & & | & & | & & | & & \\ & & \mathrm{CH_3} & & \mathrm{CH_3} & & \mathrm{CH_3} & & \end{array}$$

from which all others are derived by replacing some of the methyl groups. Silicones are common sealants, e.g. as RTV (room temperature vulcanization) resins; they are also used as O-rings (silicone rubber), mould release agents and for lubrication.

6.2 Integrated charge

The run conditions during the different phases of the ageing study are summarized in table 6.1 while the experimental setup itself has been described in detail in chapter 3. Of the

Parameter	BIS multilayer 1 (MDTs under gas recirculation)	BIS multilayer 2 (no gas recirculation)
gas pressure	3 bar (abs.)	3 bar (abs.)
volume	150 l	150 l
irradiated area	170×90 cm^2	170×90 cm^2
irradiated tubes	114	114
reference tubes	6	6
5.1.2002 – 15.3.2002, no irradiation		
fresh gas flow	20 Nl/h (1 Vol./day)	20 Nl/h (1 Vol./day)
circulated gas flow	—	—
high voltage	3080 V	3080 V
gas gain	$2 \cdot 10^4$	$2 \cdot 10^4$
mean current density	< 0.01 nA/cm	< 0.01 nA/cm
tube count rate	30 Hz (cosmics)	30 Hz (cosmics)
15.3.2002 – 10.5.2002, period 'Age1'		
fresh gas flow	2 Nl/h	20 Nl/h
circulated gas flow	18 Nl/h	—
high voltage	3160 V	3160 V
gas gain	$4 \cdot 10^4$	$4 \cdot 10^4$
mean current density	0.01 μA/cm	0.01 μA/cm
tube count rate	1400 Hz/cm	1400 Hz/cm
27.9.2002 – 5.3.2003, period 'Age2'		
fresh gas flow	4 (2)* Nl/h	20 Nl/h
circulated gas flow	36 (18) Nl/h	—
high voltage	3420 (3080) V	3420 (3080) V
gas gain	10^5 ($2 \cdot 10^4$)	10^5($2 \cdot 10^4$)
mean current density	0.025 (0.005) μA/cm	0.025 (0.005) μA/cm
tube count rate	1200 Hz/cm	1200 Hz/cm
5.3.2003 – 8.5.2003, period 'Age2', multilayers 1+2 in series		
fresh gas flow	4 Nl/h**	4 Nl/h**
circulated gas flow	36 Nl/h**	36 Nl/h**
high voltage	3420 V	3420 V
gas gain	10^5	10^5
mean current density	0.025 μA/cm	0.025 μA/cm
tube count rate	1200 Hz/cm	1200 Hz/cm

*Values given in brackets correspond to the condition during the first four weeks after restarting the system.

**for the combination of BIS multilayer 1 and 2

Table 6.1: Run conditions during different phases of the BIS ageing study.

240 BIS drift tubes 120 were connected to the gas recirculation system (BIS multilayer 1); the remaining were operated in the classical flushing mode for comparison (multilayer 2). During irradiation, the tube count rate was limited to ≈1400 Hz/cm by the photon flux at GIF and the distance of the setup from the radioactive source. The gas gain was varied from the nominal $2 \cdot 10^4$ (3080 V) at the beginning of the measurements to $\approx 10^5$ (3420 V, taking into account the gain loss due to space charge) during most of phase 'Age2'. Figure 6.1 shows the integrated charge versus time, with the changes in gain clearly visible in the slope of the graph. On average a charge of ≈240 mC/cm was collected per tube and centimeter wire length until the end of the measurements in May 2003. This corresponds to 40% of the Atlas requirement specified in equation (2.20). Due to the inclined geometry of the chamber with respect to a vertical orientation MDTs at one side of the chamber had a larger distance to the source than tubes on the other side (fig. 3.13). The least irradiated MDT accumulated a charge of 160 mC/cm while the tube with the highest count rate accumulated 320 mC/cm.
During data taking with nominal or slightly increased gain (3160 V) the gas flow through the MDTs was adjusted to one volume exchange per day, which corresponds to the Atlas specification given in table 3.1. For tubes on multilayer 1 90% of the gas flow was recirculated with the remaining 10% being injected as 'fresh gas' from the premix supply. In the part of period 'Age2' in which the BIS chamber was operated at a gain of 10^5 the gas flow was doubled in multilayer 1.
Ageing investigations with the 120 tubes of multilayer 2 operated in flushing mode ended on March 5th, 2003. At that point the two multilayers were connected in series for the remaining two months of irradiation and operated together under gas recirculation.

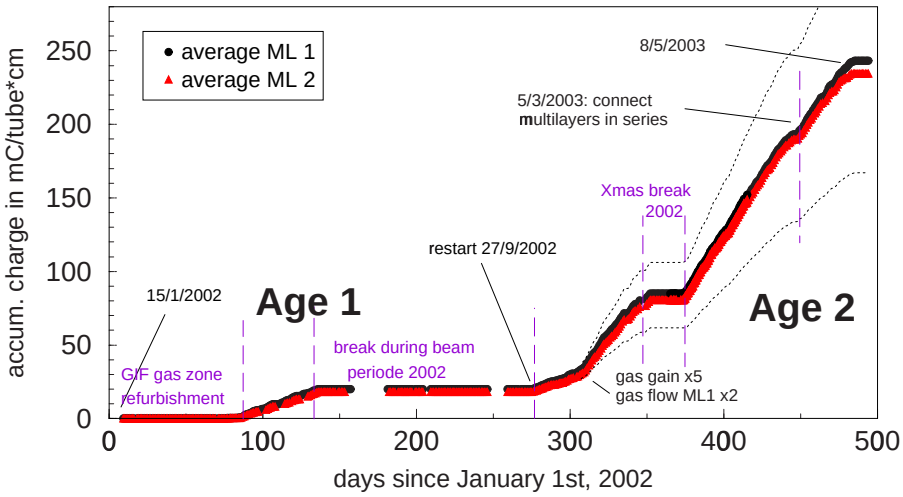

Figure 6.1: Integrated charge versus time during the ageing study at GIF. The average charge collected per centimeter wire length by May 2003 (end of the measurements) is 240 mC/cm for tubes in BIS multilayer 1 and 230 mC/cm for tubes in multilayer 2. Count rates in the BIS chamber varied by a factor 2 over the chamber width in period 'Age2', due to the inclined chamber geometry (fig. 3.13); the maximum and minimum accumulated charge is indicated by the dotted lines.

6.3 Methods of analysis

During the ageing study the BIS chamber performance was monitored with cosmic muons. Weekly reference runs were taken for this purpose with the GIF radioactive source 'switched off', i.e. retracted into its lead housing. During these runs the 12 reference tubes, 6 in each multilayer and disconnected from HV during irradiation, were powered and read out in the same way as all other MDTs. The scintillator hodoscope described in section 3.5 was used to provide a trigger signal and to start the gate for the Camac ADCs connected to every third MDT (see section 3.6.4 for details). For each event the following information was recorded:

- drift time t_{drift} for all tubes traversed by the muon track,
- pulse charge integrated over a gate of 1 μs for all tubes with ADC readout,
- hit and timing information from the scintillator hodoscope.

Each data run, comprising typically between 250 000 and 400 000 events, was processed three times. In the first iteration, the position t_0 of the leading edge of the drift time spectrum was obtained for all tubes according to the method described in 4.2. Iteration 2 was dedicated to determining the ADC pedestals, Q_{ped}; the last pass over the data used t_0 and Q_{ped} as input and produced the actual pulse height spectra of the individual MDTs. Steps 1 and 2 could have been combined into a single one which was however not done for technical (programming) reasons.
During all ADC data analysis and separately for each MDT, events were classified into two classes, namely

- **Class A**: Events where the data for the tube under study contained an AMT reading, i.e. events where an ASD threshold crossing occured, implying that the tube 'saw' a muon or a noise hit;
- **Class B**: Events where no ASD threshold crossing occurred, i.e. no AMT data word was present in the data for the tube under study.

Class B events were used to determine the ADC pedestal, Q_{ped}. A Gaussian was fitted to the pulse height spectrum (fig. 6.2) for this purpose; Q_{ped} was then defined as the centre of the Gaussian distribution.

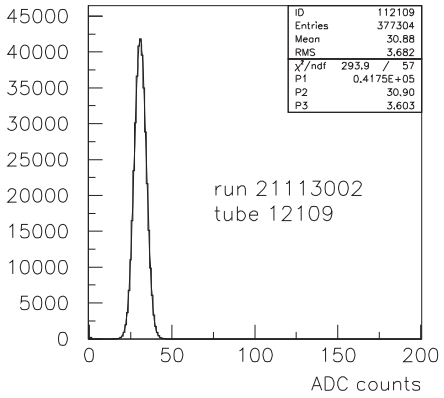

Figure 6.2:
ADC spectrum for class B events. A Gaussian is fitted to the histogram to obtain the ADC pedestal.

Analysis of class A events

The left column of figure 6.3 shows typical ADC spectra measured during test beam data taking and during the two ageing periods; the ADC pedestal has already been subtracted in all cases. All three histograms show a tail towards large pulse charges Q, which is typical for a Landau distribution (equation (2.3) and fig. 2.3); they however significantly deviate from the Landau shape for small values of Q in so far as the rising edge of the distribution is less sharp. The reason for this behaviour is the fact that muons traversing an MDT travel different distances in the operating gas, depending on the drift radius r_{drift} and the track angle φ with respect to the tube axis, and consequently produce a different amount of ionization. All pulse height data has therefore been corrected on an event-by-event basis for the actual ionization path length l_{ion} according to

$$Q_{corr} = (Q_{counts} - Q_{ped}) \cdot c_{adc} \cdot \frac{30\,\mathrm{mm}}{l_{ion}} \tag{6.1}$$

with

$$l_{ion} = 2 \cdot \frac{\sqrt{b^2 - r_{drift}^2}}{\sin\varphi}, \qquad 1\,\mathrm{mm} \leq r_{drift} \leq 13\,\mathrm{mm}; \tag{6.2}$$

Q_{counts} is the ADC reading, c_{adc} is a channel specific constant ('ADC gain') for the conversion of ADC counts into a charge and b is the inner tube radius. The drift radius r_{drift} was calculated from the measured drift time using an appropriate rt-relation while the angle φ was obtained by performing a crude track reconstruction based on the hodoscope data, as discussed in more detail in appendix B.
The right column of figure 6.3 shows pulse height spectra for the different run periods after the above corrections were applied; the inlay in the two lower plots is the spectrum one obtains correcting for r_{drift}, but not for the track angle φ. A Landau distribution in the Moyal approximation

$$f(\lambda) = A \cdot \sqrt{\frac{e^{-(\lambda + e^{-\lambda})}}{2\pi}} \qquad \text{with} \qquad \lambda := \frac{Q - Q_p}{\xi}\,, \tag{2.4}$$

was fitted to the histograms for all cosmics data; the most likely charge Q_p was then defined as 'the' pulse height for a given tube and run. Test beam spectra were fitted with the correct Landau function

$$f(\lambda) = \frac{1}{\pi} \cdot \int_0^\infty e^{-s\ln s - s\cdot\lambda} \cdot \sin(\pi s)\, ds\,, \tag{2.3}$$

in order to better reproduce the sharp rising edge. The larger width of ADC spectra measured in periods 'Age1' and 'Age2' compared to the ones found from test beam data is explained by the fact that mono-energetic muons were used in the latter case, but not in the former.

Relative pulse height definition: Since changes in temperature, operating gas composition or anode voltage all affect the gas gain, in addition to Q_p a relative pulse height Q_{rel} was defined as

$$Q_{rel} := \frac{Q_p(\text{tube } xxx)}{Q_p(\text{reference tube})}\,, \tag{6.3}$$

in order to help disentangle such effects from true ageing. Reference tubes[2] were disconnected from HV during irradiation, as pointed out in section 3.6.4.

[2] MDTs 11101 and 11106 in multilayer 1, 12403 and 12404 in multilayer 2

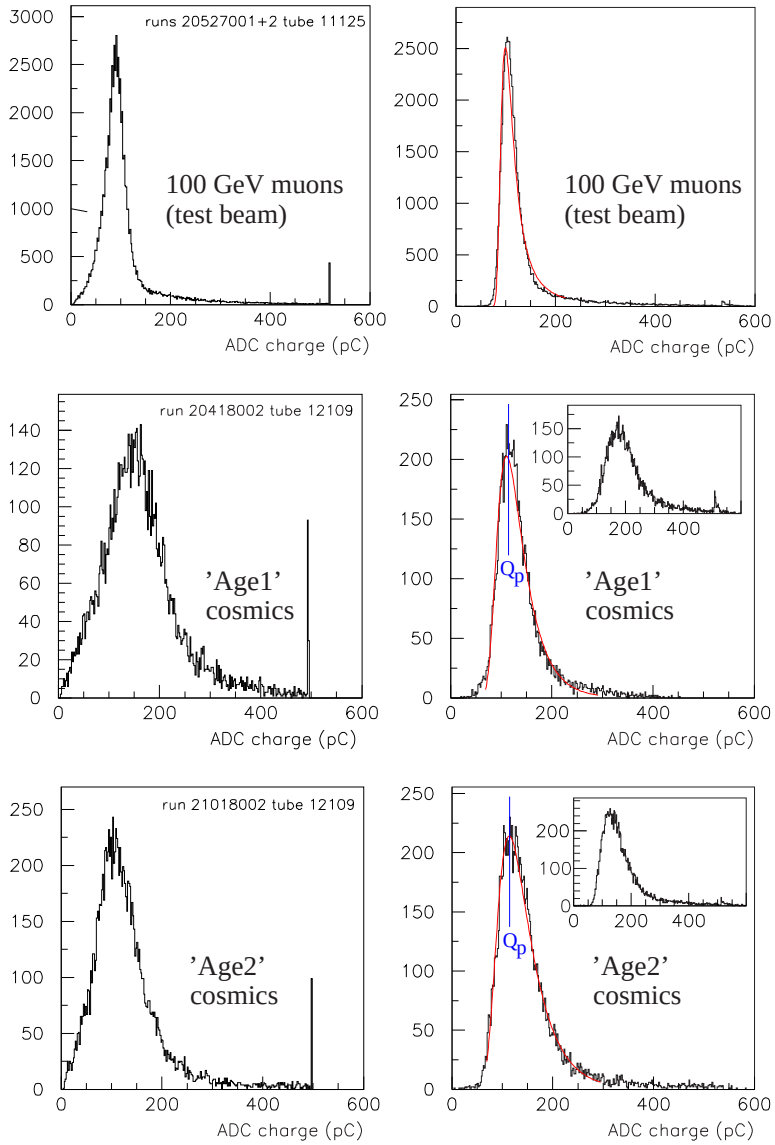

Figure 6.3: ADC spectra for cosmic and test beam muons. The left column shows raw pulse charge distributions, as measured by the ADC and before the ionization path length correction described in the text. Plots in the right column show the pulse charge distribution after all corrections have been applied. The red lines are the result of a Landau- (test beam data) or Landau-Moyal (ageing data) fit. The plots also show the definition of Q_p, which was used as 'the' pulse height for a given MDT and run. The inlay in the two lower-right plots is the ADC spectra after correcting for different drift radii, but not for the track angle φ with respect to the tube axis. The latter correction is more important for ageing period 'Age1' than for 'Age2', due to the changed geometry.

6.4 Accuracy and systematic errors

The relative error estimate on the parameter Q_p returned from the Landau fit ranges from 0.3% to 1%, depending on the number of events for a particular run and tube. Comparing

pulse heights from different runs, as is the normal way in checking for chamber ageing, the accuracy of the measurement is however dominated by several systematic effects which will be discussed in the following.

Temperature dependence: As can be seen from Diethorn's formula (2.13), the gas gain of a drift tube is highly dependent on the density and thus the temperature T of the operating gas. Rearranging (2.13) one finds

$$G(T+\Delta T) = G(T)\cdot\left(1+\frac{\Delta T}{T}\right)^{x} \underset{\Delta T \ll T}{\approx} G(T)\cdot\left(1+x\cdot\frac{\Delta T}{T}\right) \tag{6.4}$$

where T is the absolute temperature in Kelvin and $x \approx 9.857$ for Ar:CO_2=93:7 at 3 bar absolute pressure. For the purpose of the measurements presented in this chapter, the temperature dependence of G was determined experimentally from data taken during the test beam running (fig. 6.4). The relation

$$Q_{p,20} = \frac{Q_p(T)}{1+(0.022\pm 0.003)\cdot[T-20°\mathrm{C}]} \tag{6.5}$$

was then used to correct all pulse height data to 20 °C. The experimentally found value of 2.2% change in gas gain per degree Celsius is considerably smaller than what one expects from formula (6.4), namely $x/T = 3.4\%$ for an average T of 293 K. This can in part be explained by the fact that for muons the pulse height does not only depend on the gas gain G but also on the primary ionization produced in the operating gas; the latter is proportional to the gas density and thus decreases with temperature. Nevertheless this effect is not large enough to account for the full difference in the obtained values so that a question mark has to be put to the accuracy of the Diethorn parameters (2.14).

Temperature non-uniformity: While temperature changes between different data runs can be taken into account by using equation (6.5), temperature non-uniformities and (sudden) variations during a run are more difficult to deal with. During both ageing periods the temperature was measured in 10 locations on the BIS chamber; the obtained temperature values had a typical spread of 1 to 1.5 °C. The measurements in particular showed the presence of a temperature gradient from the chamber readout side towards the HV side, due to the heat dissipated by the front end electronics.
A stable and small temperature non-uniformity does not affect the ageing measurements; the same is true for a slow variation in temperature during the typically 3 to 4 hours

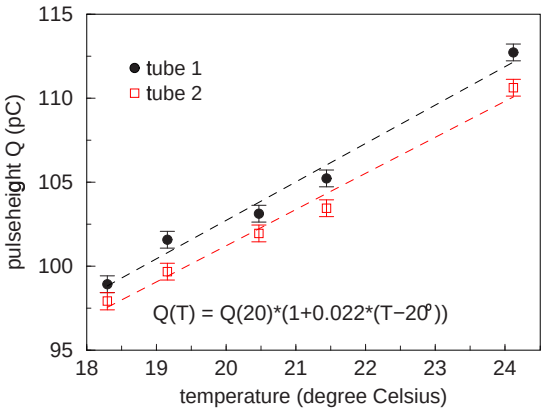

Figure 6.4:
Pulse height versus temperature for data acquired during the test beam period. A straight line $Q(T) = Q_{20}\cdot(1+0.022\cdot(T-20°C))$ was fitted to the data and used as a correction for the ageing measurements.

of a data run. In both cases the pulse height spectrum is slightly broadened, with the maximum of the Landau distribution, Q_p, corresponding to the mean temperature which consequently has to be used when applying the above corrections. More problematic are sudden changes in temperature during a run; such changes occurred frequently between January and March 2003, when large quantities of material were removed from the hall GIF is located in and consequently the building's doors were repeatedly opened and closed. The difficulty with sudden temperature changes stems from the fact that in this case the system is not in thermal equilibrium; the temperature values measured on the outside of the BIS chamber may not agree with the temperature in the operating gas, which causes a rather large uncertainty in the correction according to formula (6.5).
The total error in $Q_{p,20}$ due to (remaining) temperature effects is estimated to be approximately 3%, excluding runs with large ($\geq 3°$C) sudden changes in temperature on the basis of the slowcontrol data. The error in the relative pulse height Q_{rel} is smaller; no temperature correction is needed in this case, since a change in gain due to a change in temperature will affect numerator and denominator of equation (6.3) in the same way.

Changes in anode voltage: Variations in the MDT anode voltage V affect the gas gain almost as strongly as temperature changes; from Diethorn's formula (2.13) one obtains the relation

$$\Delta G = 0.5\% \cdot G \cdot \Delta V \qquad \text{for } G \approx 2 \cdot 10^4 \text{ and } \Delta V \ll V \approx 3080\,\text{Volt}. \tag{6.6}$$

During phase 'Age2' the applied chamber high voltage was calibrated before each reference run with the help of a precise voltage divider and a high precision voltmeter[3]; the uncertainty in V in this period was less than 1 V, corresponding to an error of 0.5% in the absolute pulse height Q_p. Q_{rel} is unaffected by changes in the high voltage.
For the phase 'Age1' the error in V is estimated to be of the order of 5 V, mainly due to a possible drift in the calibration of the power supply used.

Changes in the operating gas mixture: Changes in the composition of the operating gas affect the absolute pulse height Q_p, but not the relative one, Q_{rel}. Using a pre-mixed gas delivered in several batches, the most likely change to happen is a variation in the exact ratio between argon (Ar) and carbon dioxide (CO_2). Since the maximum drift time t_{max}, which strongly depends on the CO_2 content, for BIS multilayer 2 did not show any change with time, this could be excluded from having happened at any point during the ageing study.
For MDTs operated under gas recirculation (multilayer 1) a change in t_{max} was observed over the course of the study and proven to be caused by a changing water concentration in the gas (figures 3.20, 3.21). Since water concentrations up to 1500 ppm have no influence on the gas gain, as discussed in section 3.9.4 (fig. 2.10), this was however of no importance for the ageing analysis.

Accuracy of the ADC pedestal fit: The ADC pedestal is determined from the Gaussian fit described above to better than 0.5% of its value; since for all channels the pedestal amounts to no more than 10% of the number of ADC counts corresponding to Q_p, the effect of its error on the uncertainty of the pulse height is negligible. A drift of the pedestal was observed for most channels with time; since the pedestal is however determined anew for each reference run, this has no impact on the accuracy of the ageing results.

[3]Model HP 34970A, Hewlett Packard Co, Loveland ,US

Impact of a wrong rt-relation: A wrong rt-relation will result in a wrong ionization path length correction according to formula (6.1); l_{ion} and consequently Q_{corr} may be either too small or too large. The rt-relations utilized in the ageing study were either taken from the test beam measurements or obtained with the integration method described in section 4.3.1 directly from the reference run data. In both cases they were accurate to better than $\pm 0.5\,\mathrm{mm}$; by adding or subtracting this number from an approximate rt-relation is was verified that the impact of this uncertainty on the value of Q_p is negligible, if events used are restricted to the range $r_{drift} \leq 13\,\mathrm{mm}$. This was done in all analyses.

Impact of noise hits: Since no pattern reconstruction or selection of hits belonging to tracks was performed in the ageing analysis, noise hits lead to additional entries in the ADC spectrum. In the case of the BIS chamber almost all recorded noise signals were due to the gas recirculator ATC, as stated in section 3.9.4. These signals had a bipolar shape; their charge integrated to zero over the ADC gate length of $1\,\mu\mathrm{s}$. They therefore did not contribute directly to the ADC spectrum.
Noise hits however had – in the same way as a bad rt-relation – the potential to cause a wrong ionization path length correction l_{ion}; this was the case if a noise hit masked a muon signal, i.e. if it was recorded by the AMT at an earlier time than the first threshold crossing of the muon pulse. A too small drift time and thus radius was then attributed to the event which resulted in a too large value of l_{ion}, a too small corrected charge Q_{corr} and eventually a distortion of the ADC spectrum. To exclude such a bias, the pulse height Q_p was studied as a function of the drift radius. A given data run or tube was included in the final analysis if Q_p was independent of r_{drift}; this is only the case if noise does not play a role.

Pulse height versus track position in wire direction: The voltage signal at the output of an MDT has its origin in the current $I(t)$ induced in the anode wire by the drifting ions produced in the gas amplification process, as discussed in section 2.2.5. The MDT passive electronics circuitry includes a $380\,\Omega$ termination resistor on the HV side (fig. A.1); this implies that only a part $I_1(t)$ of the current $I(t)$ is collected by the amplifier-discriminator-shaper (ASD) combination on the readout side. Since the anode wire has a non-negligible electric resistance of $44\,\Omega/\mathrm{m}$, it effectively functions as a voltage divider; $I_1(t)$ and thus any pulse charge measured with the help of an ADC therefore depend on the position along the tube.
To arrive at a prediction for the size of this dependence, signals were simulated with the program GARFIELD; the signal propagation along the wire was taken into account by describing an MDT through its transfer function given in appendix A, formula (A.5). Figure 6.5 summarizes the results of the simulation: Plot (a) shows the integrated charge for single electrons; the induced current in this case is

$$I(t) = -\frac{q}{2 \cdot \ln(b/a)} \cdot \frac{1}{t + t_0}\,,$$

as stated in formula (2.17). The fraction of charge collected by the amplifier depends on the integration time T_{int}; for a short interval (200 ns) the measured pulse charge decreases by up to 10% when moving from the readout to the HV side of the drift tube, while for larger integration times the effect becomes less distinctive. This is in agreement with the results presented in [38].
In the studies of this thesis the ADC gate for muon pulse charge measurements was generated by the scintillator hodoscope, not by the MDT signals themselves. This implies

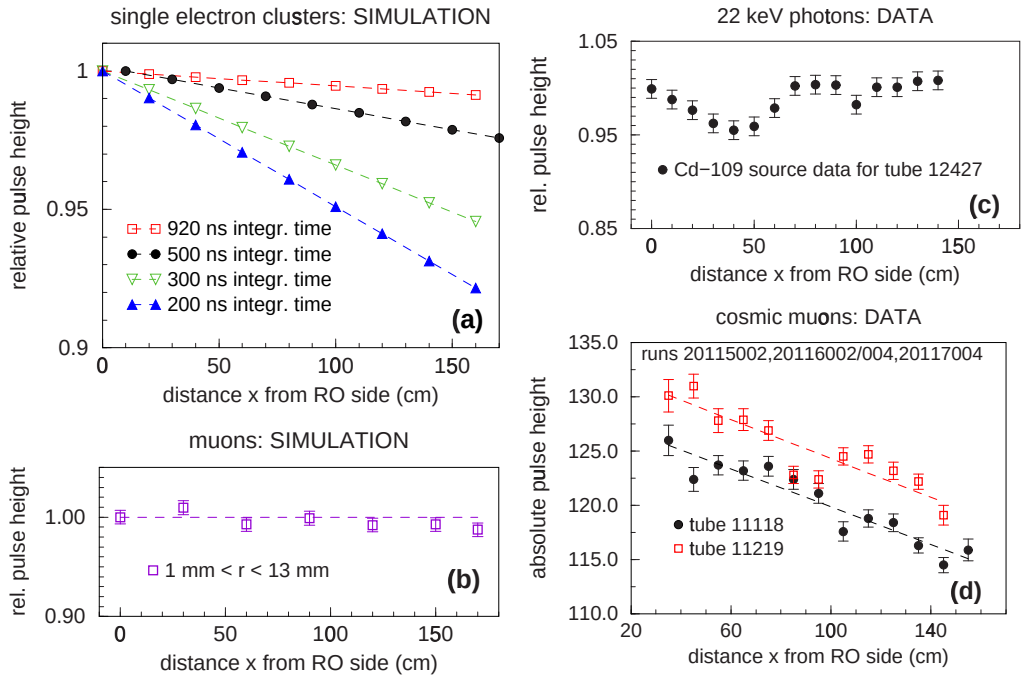

Figure 6.5: Collected pulse charge Q versus distance x from the readout side of an MDT. Plot (a) shows simulation results obtained with the program GARFIELD for single electrons; $Q(x)$ in this case is strongly influenced by the time over which the pulse is integrated. (b) shows the simulation results for muons and a uniform tube illumination; no dependence of the collected pulse charge on x is discernible in this case. (c) and (d) are experimental findings, both for a ^{109}Cd source moved along the tubes and for cosmics. Graph (c) does not show a systematic change in the collected charge with the distance from the readout side; the minimum at ≈ 40 cm is possibly due to a local deviation of the wire diameter from its nominal value. In contrast to (c) plot (d) gives evidence for a decrease in pulse height with x.

that the time $T_{int} - t_0$ over which the current signal $I(t)$ is integrated depends on the drift radius. Plot (b) shows the result of the GARFIELD simulation for a uniform MDT illumination and an ADC gate length of 1 μs, as used in the ageing measurements. No pulse height dependence on the track position can be seen. Such a behaviour was experimentally found when moving a small radioactive ^{109}Cd-source along the MDTs (plot (c), the minimum at 40 cm is possibly due to a local deviation of the anode wire diameter from its nominal value); it however disagrees with a direct cosmics measurement performed during the pre-phase of period 'Age1' (Jan./Feb. 2002), in which the hodoscope was used to reconstruct the muon track position along the MDT axis (plot (d)). Some of the disagreement can be explained by a temperature gradient of the BIS chamber, but not all of it. One may speculate whether the remaining decrease in pulse height is faked by a slightly wrong hodoscope track reconstruction (angle φ depending on the track position or similar); since this could neither be excluded nor confirmed with any certainty, all that can be concluded is that if a pulse height dependence on the position in wire direction exists, then it is at maximum of the order of 10% over the full 170 cm of the BIS tubes.

Overall accuracy and detection limit for ageing phenomena: The detection limit for ageing phenomena in the study presented in this thesis is estimated to be 3% based on

the above discussion of possible systematic effects and under the assumption that ageing occurs in more than one tube. Absolute pulse heights $Q_{p,20}$ are assumed to be accurate to between 5 and 7%; they have larger uncertainties than the relative measurements Q_{rel} due to the temperature correction, which is necessary in the former case but not in the latter. Regarding gain variations in wire direction, any effect below the level of 5% can be

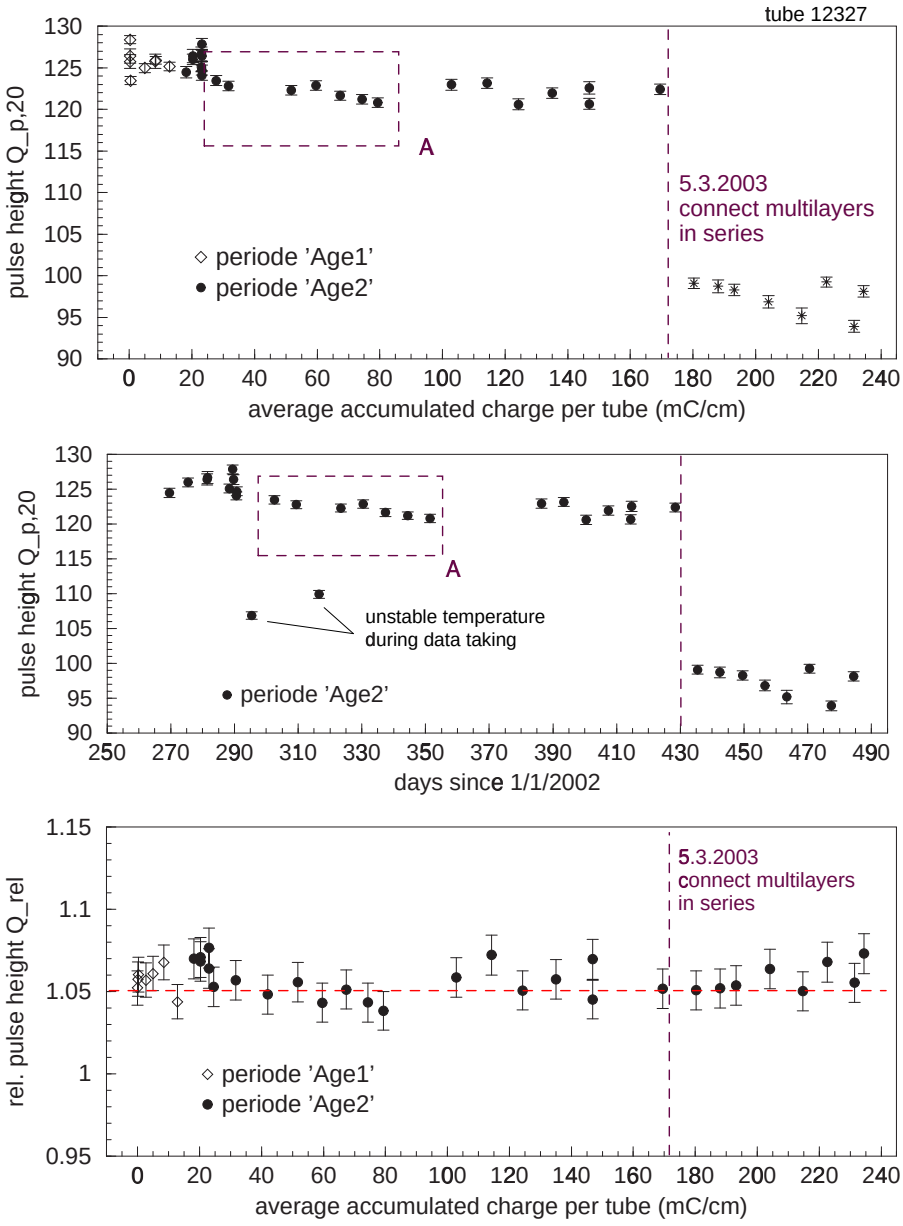

Figure 6.6: Ageing results for tubes operated without gas recirculation (BIS multilayer 2). The top two graphs show the absolute pulse height $Q_{p,20}$ as a function of time and the average accumulated charge. Only statistical errors are shown. On the 5th of March 2003 multilayer 2 was connected in series with multilayer 1; this caused a shift in $Q_{p,20}$ values due to a modified pressure regulation. The bottom plot shows the relative pulse height Q_{rel} as a function of the integrated charge; the results are consistent with a straight line of zero slope, i.e. no evidence for ageing is present in the data.

due to temperature variations; a decrease in pulse height of a few percent when moving from the chamber readout to the HV side might furthermore be due to the non-negligible ohmic resistance of the anode wire.

6.5 Ageing results for BIS multilayer 2 — vented gas system

The results of the ageing study for a typical MDT in multilayer 2 are shown in figure 6.6. The shape of the relative pulse height Q_{rel} as a function of either the accumulated charge or the time is consistent with a straight line with zero slope; the data therefore excludes ageing effects or a loss in gas gain exceeding the detection limit of 3% given in the previous section. The slight decrease in the absolute pulse height $Q_{p,20}$ in the region marked as 'A' is thought to be due to the temperature correction (formula (6.5)) being slightly wrong. This is well conceivable, since (6.5) was derived from test beam data taken at temperatures between 18.5 and 24.5 °C, and thus had to be extrapolated to the lower temperature values during ageing periode 'Age2' (14.5 to 21 °C). None of the 38 monitored MDTs showed any distortion in the ADC spectrum.
The measurements confirmed Ar:CO_2=93:7 as an ageing-free operating gas for the Atlas drift tubes; they further (re)validated all materials and components used in the construction of an MDT chamber.

6.6 Ageing results for BIS multilayer 1 — gas recirculation

In contrast to the results presented in the previous section, ADC spectra for MDTs operated with gas recirculation (BIS multilayer 1) started to show a distortion from an accumulated charge of a few tens of mC/cm onwards (fig. 6.7). The distortion progressed with time, with a clear double peak structure visible at the end of period 'Age2'. By using the hodoscope data to reconstruct the muon track position, a massive loss in pulse height in the first 30 to 40 cm from the readout, i.e. gas input side of the chamber was established as the cause for this behaviour, as can be seen from figure 6.8; the same figure also shows the result of a cross check done by moving a small radioactive source along the MDTs. In addition the following was established:

- All 33 MDTs of multilayer 1 kept under high voltage during irradiation and equipped with a (functioning) ADC readout show a decreased pulse height close to the gas inlet side, while the two reference tubes 11101 and 11106 do not exhibit such a gain loss.
- A distortion of the ADC spectrum is visible from the first run of period 'Age2' (≈20 mC/cm integrated charge); no spectrum distortion can be found for any 'Age1' run.
- The gain reduction and the spectrum distortion are progressing with time (fig. 6.10, left graph).
- For a distance greater than ≈ 50 cm from the MDT gas inlet side no gain drop is observable over the full duration of the ageing study (fig. 6.9).
- The fraction by which the pulse height is reduced close to the gas inlet with respect to the opposite tube end does not depend on the level of irradiation, which varied by a factor 2 over the width of the BIS chamber, as described in section 6.2.

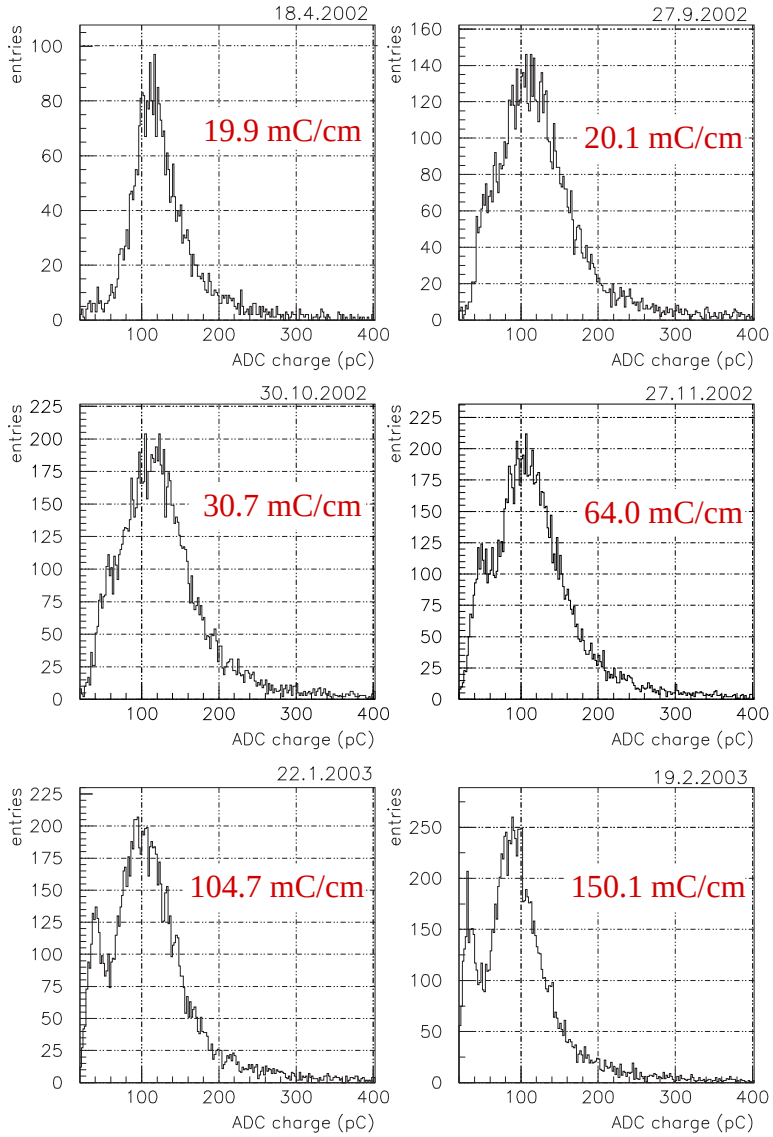

Figure 6.7: ADC spectrum development for tube 11113 in BIS multilayer 1 between April 2002 and February 2003. The data shown is not corrected for temperature effects, so only changes in the shape of the spectrum but not in the position of the maximum should be considered. A distortion of the usual Landau distribution is clearly visible for small charges; the distortion is progressing with time.

- The gain loss is significantly more pronounced for MDTs in layers 3 and 4 than for tubes in layers 1 and 2 (fig. 6.10, right graph).

Discussion of results: The observation of a gain loss solely in the region close to the gas inlet side of the MDTs strongly points to a contaminant in the operating gas rather than to a polymerization of the gas components themselves. A chemical analysis performed after the completion of the tests at GIF confirmed this suspicion, as discussed in the next section.

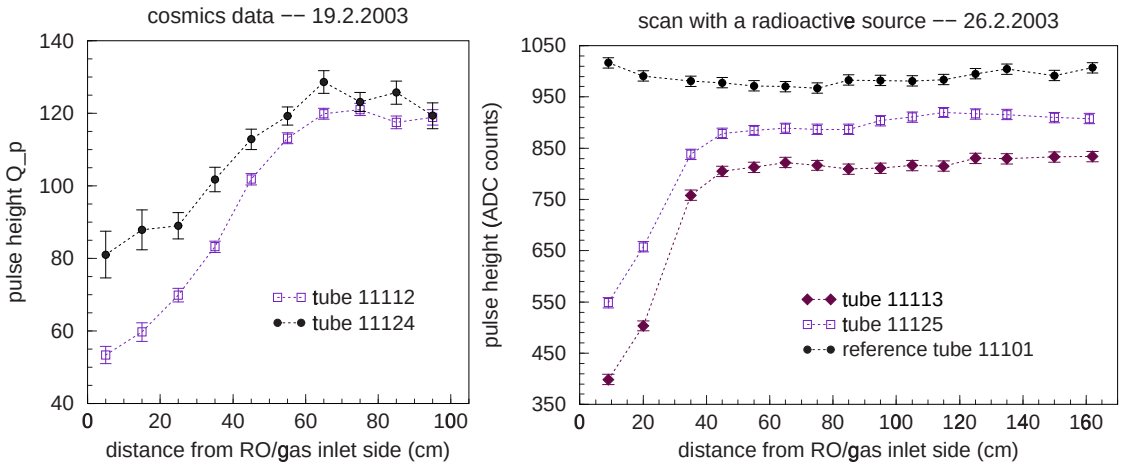

Figure 6.8: Pulse height versus position in wire direction for MDTs in BIS multilayer 1. The left plot shows results obtained during normal reference data taking by reconstructing the muon track position from the hodoscope information; the right graph shows the result of a cross check performed with a small, movable radioactive source. The data for reference tube 11101 is consistent with a constant pulse height over the full tube length, while the remaining four tubes exhibit a reduced pulse height close to the MDT gas inlet side. The absolute pulse height differs from tube to tube, most likely due to a slightly different gain of the front end electronics.

For ageing effects to be absent after the first few tens of cm, the contaminant has to attach itself very effectively to the wire, so that it is totally removed from the gas mixture after this distance. Alternatively one can speculate that in irradiating the drift gas and in the gas amplification process certain chemical substances ('active species') are formed, which catalyze etching effects and thus prevent the formation of wire deposits further downstream of the tubes. Such substances will typically be short-lived. In the MDT case they indeed cannot have an infinite lifetime; otherwise they would be re-introduced into the MDT gas stream by the recirculation system and no ageing should occur anywhere along the wire. If their lifetime on the other hand is finite, one expects ageing to re-appear when connecting

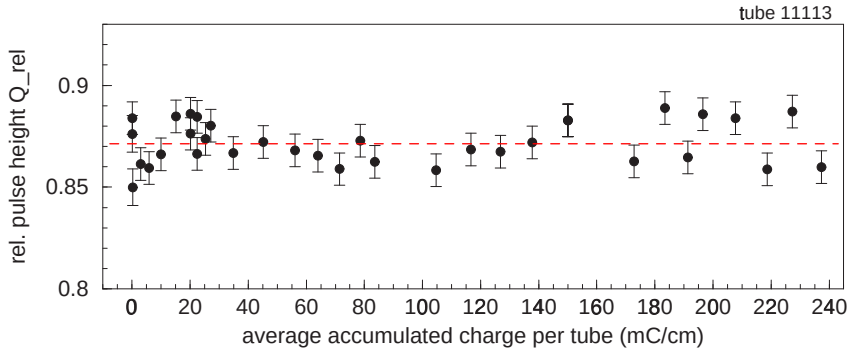

Figure 6.9: Pulse height for tube 11113 in multilayer 1, using tracks with a distance greater than 50 cm from the readout side only. No loss in gain is observable over the duration of ageing period 'Age2'.

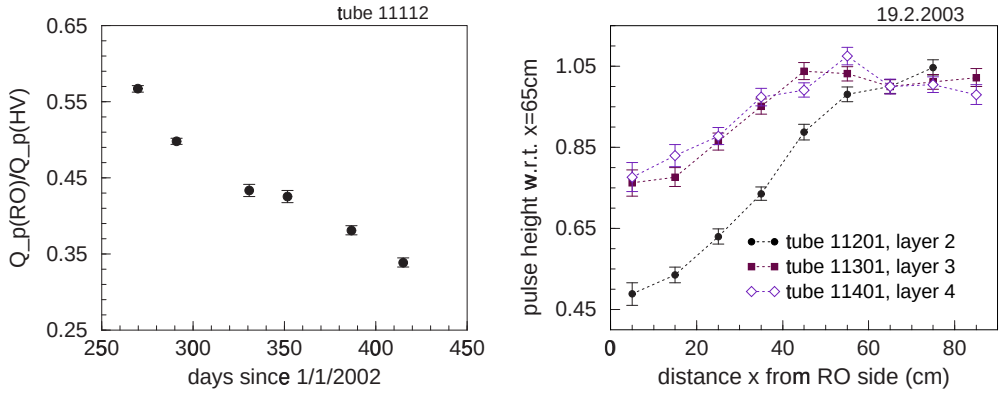

Figure 6.10: Left: Ratio between the pulse height close to the readout side and close to the HV side for tube 11112 in multilayer 1. The progressive behaviour of the pulse height loss close to the readout/gas inlet side with time is clearly visible. Right: Gain loss for tubes in different layers of the BIS chamber. The pulse height reduction is significantly larger in layers 1 and 2 than in layers 3 and 4.

a second set of drift tubes in series with the first one, with the gas flowing from the first to the second passing a region in which no gas amplification processes take place. To check for this possibility, BIS multilayer 2 was connected in series with multilayer 1 on the 5th of March 2003, 2 months before the end of ageing period 'Age2'. As can be seen from figure 6.6, no loss in pulse height was observed for the on average 50 mC/cm charge collected per tube in this configuration. It was thus concluded that etching or screening effects by active species did not play a role in the measurements presented in this thesis.
The reason why no distortion in the pulse height spectrum is visible for any 'Age1' run is the fact that in this period the first ≈ 30 cm of the tubes, measured from the gas inlet side, were not covered by the trigger acceptance of the hodoscope (section 3.7). The cause for tubes in BIS layers 1 and 2 showing distinctly more pronounced ageing than tubes in layers 3 and 4 is unclear; the only significant difference between them is the different length (and inner diameter) of the metal tubelets supplying gas to the MDTs (section 3.4). It was at first believed that this might have caused different gas flows in the various BIS layers and thus a different amount of contamination introduced into the individual tubes and deposited on the wire; a direct measurement of the tubelet impedances however ruled out this hypothesis.

6.7 Chemical and surface analysis

After irradiating the BIS chamber at GIF ended, several MDTs of multilayer 1 were opened and samples both from the anode wire and from the cathode were removed. In order to confirm (or discard) the suspicion of a contaminant being responsible for the observed ageing effects and to find its source, various chemical and surface analysis methods have been used; they will be shortly summarized in the following:

Scanning Electron Microscopy: Scanning Electron Microscopy or SEM makes it possible to resolve sub-micrometer details on the wire surface. This is done by moving a thin electron beam in a controlled way over the material under study and recording the number

of electrons reflected. From the contrast of the SEM picture it is also possible to deduce whether a material is electrically conducting or not.

Energy Dispersive X-ray analysis: Energy Dispersive X-ray (EDX) analysis is a method usually combined with SEM. When hit by the scanning electron beam, atoms are left in an excited state with energy E_i; they return to their ground state E_0 or a lower intermediate state E_j by emitting X-rays with a frequency proportional to the energy difference $E_i - E_j =: \Delta E_{ij}$. Since the values of ΔE_{ij} are characteristic for each chemical element, the chemical composition of a material can be identified by recording the X-ray spectrum; this is usually done with the help of a semi-conductor detector. EDX is sensitive to all elements except hydrogen; the volume of material probed is usually of the order $1\,\mu\text{m}^3$. With the instrument used for this thesis a volume of $0.5 \times 0.5 \times 0.5\,\mu\text{m}^3$ was analysed; material on the surface of another substance could be detected if its thickness exceeded $0.2\,\mu$m.

Ultraviolet Spectroscopy: Ultraviolet (UV) spectroscopy is usually performed as absorption spectroscopy on a liquid sample, as can e.g. be obtained by performing a hexane-extraction of a suspicious gas system component. The spectrum of a UV lamp is recorded with a frequency sensitive receiver, once with the light passing the sample and once without; from the difference in the spectra the presence of substances other than the sample liquid itself can then be deduced. UV spectroscopy does not give direct information about the chemical composition of a contaminant; it is most useful to determine the overall cleanliness of a system.

Infrared Spectroscopy: Infrared or IR-spectroscopy has the advantage of being sensitive to certain chemical groups; this is due to the larger wavelength used, which excites mainly vibrational degrees of freedom in the molecules studied. With the instruments used in this thesis samples had to be solid; it was however possible to perform an extraction with hexane on a component under study and evaporate the solvent afterwards. IR-spectroscopy is the most reliable method in identifying silicone compounds through the very characteristic signature of their $(\text{Si–C–})_n$ backbone.

Gas Chromatography: Gas Chromatography (GC) is a method which separates the different components of a gas mixture according to the (retention) time they need to pass a typically several meter long column holding a special material, the so-called stationary phase. At the column output substances are detected e.g. by a change in the heat capacity of the gas. Gas chromatography is well suited to isolate the individual components of a complicated mixture; it is less capable of identifying the different chemical compounds, which is only possible by comparing the obtained retention times to tabulated data.

Mass Spectrometry: Mass Spectrometry (MS) is a method in which the sample under study is bombarded under vacuum with electrons of typically 70 eV. This will ionize some of the molecules as well as break up others. All such ions are detected by a charge sensitive sensor located behind a sequence of electric or magnetic fields which allow for determining the ions' mass. From the mass distribution the stoichiometric formula of a chemical compound can be obtained.
Mass spectrometry is a very powerful method, which suffers however if the resulting mass spectrum is a superposition of too many different substances, all breaking up according to their own fragmentation pattern during the electron bombardment. This drawback can be overcome if MS is coupled with gas chromatography in order to first split a mixture

into its individual components and then analyse them separately. The combination of the two methods is known as GC-MS.

MDT anode and cathode results

Figure 6.11 shows micrographs obtained with the SEM method for different sections of the anode wire of MDT 11112. Pictures (a) and (b) were taken close to the gas inlet of the tube. A needle-like growth perpendicular to the wire surface is clearly visible, with individual whiskers having a length between 5 and 7 μm. The needles become shorter when moving further along the tube, as can be seen from graph (c), which shows the wire surface approximately 40 cm from the gas inlet. Close to the gas outlet side of the MDT no deposits on the wire were found (plot (d)).
The SEM results agree well with the pulse height behaviour discussed in section 6.6. An EDX analysis identified the whiskers as consisting of silicon, oxygen and possibly hydrogen (plot (e)). Since silicon atoms are not part of any of the gases making up the operating mixture, the observed ageing effects are clearly due to a contaminant. Since pure silicon oxides are non-volatile and can thus not be transported by the gas, the contaminant almost certainly is a silicone with a $(\text{Si–C–})_n$ backbone chain. On the other hand no carbon was detected; this is a clear indication that a complicated chemical reaction has to take place near or on the wire surface.
In several locations on the wire, structures in the shape of a perfect sphere with a diameter of 2 to 3 μm were observed (framed region in plot (b)); the EDX analysis revealed them as consisting of pure carbon. Since their number is small, they do not have any impact on the MDT performance. Samples of the cathode were also analysed; the results were unremarkable with mainly aluminium and oxygen being found by the EDX method, consistent with the tube material.

Direct analysis of the operating gas

When a loss in gas gain became visible in the pulse height data for the first time, gas samples both from the input and from the output lines of the chamber were analysed by gas chromatography and by GC-MS. In both cases only argon, carbon dioxide and some traces of water were detected, but no foreign substances. From this an upper limit of a few tens of ppm was derived for the concentration of the pollutant in the gas.

Results for gas system components

After the deposits on the anode wire were identified as a form of silicon oxide, efforts were made to locate the source of silicon(e) in the system. Since the gas used by the MDTs of multilayer 2 came from the same premix supply as the one for tubes in multilayer 1, the gas mixture itself could not be the origin of the contamination. Based on the same argument the components (endplugs, Al-tube, O-rings) making up an individual MDT were excluded from the list of potential Si-sources. The search concentrated on the components of the gas system, which was totally dismantled after the measurements at GIF ended. The following was found:

Sources of silicone: Silicone materials in contact with the operating gas were identified by IR-spectroscopy in one seal of the dew point hygrometer model 2000 Series DewPrime, used to monitor the water content in BIS multilayer 1, and in the three large diameter

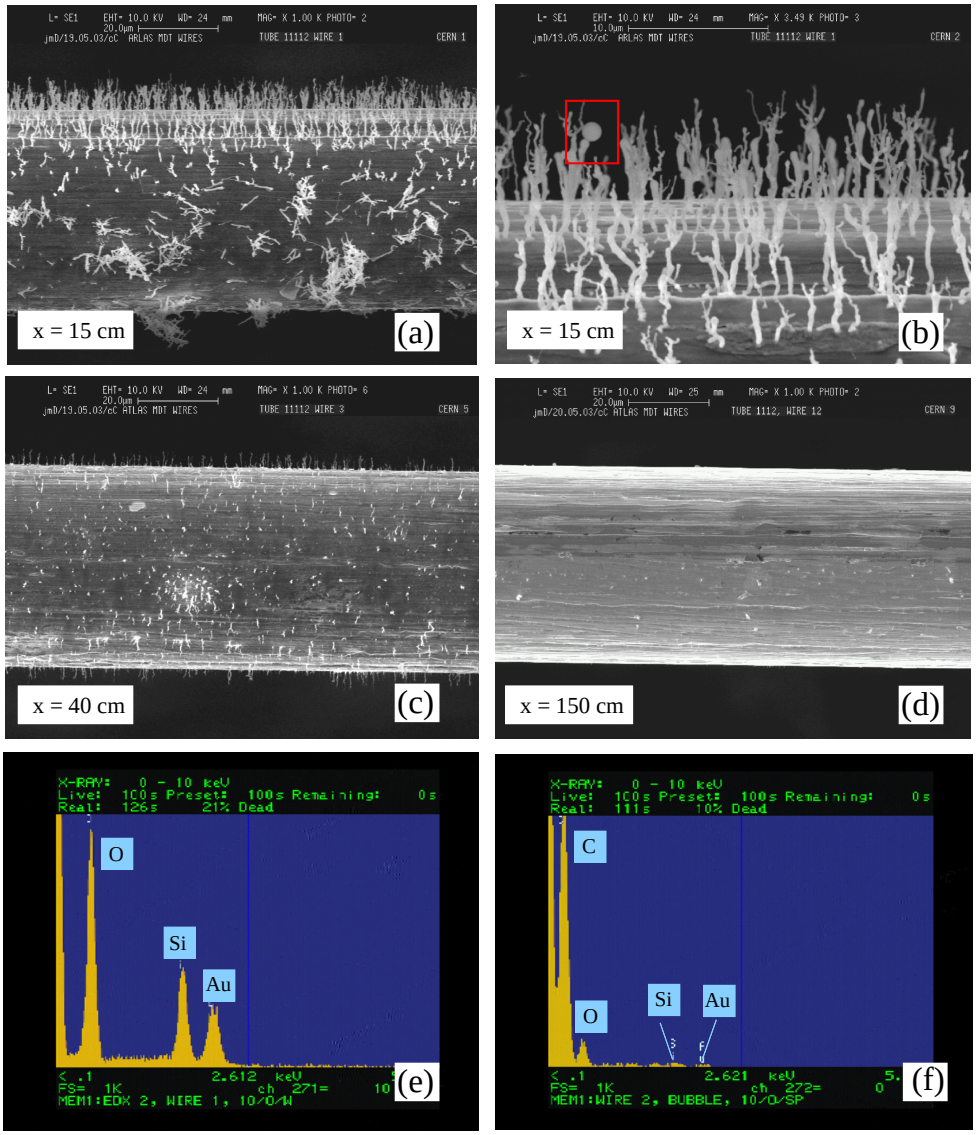

Figure 6.11: Micrographs and EDX analysis of the anode wire for tube 11112 which showed ageing. The pictures were taken at a distance of approximately 15 cm (plots (a) and (b)), 40 cm (graph (c)) and 150 cm (graph (d)) from the gas inlet of the MDT. Plot (e) shows the result of an EDX analysis performed to establish the chemical composition of the needle-like growths visible in (a) to (c). Only silicon and oxygen were found; the gold (Au) peak is due to the gold plating of the anode wire.
In several locations on the wire, structures in the shape of a perfect sphere with a diameter of 2 to 3 µm were observed. One such sphere is marked by the red rectangle in graph (b); its EDX analysis is shown in plot (e) and reveals it as consisting of pure carbon.

valves of the bypass loop. The latter are believed to be the main cause for the observed ageing effects, since the dew point hygrometer was present in the setup for phase 'Age2' only, while a pulse height loss is visible already for the very first run of this data taking period. The valves were recuperated from the Time Projection Chamber of the Aleph

experiment at LEP, where they did not cause any problems during 10 years of operation and therefore were unfortunately considered as 'clean'.

Off-chamber gas system cleanliness: During dismantling the gas system grease was found on 15 O-ring seals. An inquiry with the technician assembling the setup in 2001 yielded the answer that – against specification – the silicone-free vacuum grease Apiezon® had been used in some locations to achieve gas tightness. IR spectroscopy confirmed the lubricant to be hydrocarbon and not silicone based; the added lubricant is therefore not responsible for the observed silicon oxide deposits on the anode wires of multilayer 1 MDTs. The obtained IR-spectra were however also not compatible with the substance Apiezon but rather had the characteristics of a (cheap) ester-oil.

Internal state of the Argon Turbo Circulator ATC: The ATC was completely dismantled after the ageing test was finished in order to inspect its interior surfaces. A large quantity of graphite dust was discovered, with particles having an irregular shape and sizes well above the 5 μm mesh width of the filter which was part of the gas recirculation loop. The dust comes from the mechanical bearings supporting the ATC rotor shaft during the start-up and run-down phase (section 3.9.1); it is produced by abrasion while the turbine speed is not yet high enough for the dynamic gas bearings to provide a frictionless support. An EDX analysis of the dust particles revealed the presence of silicon (Si) besides the main components carbon (C) and antimony (Sb)[4]. A second analysis on a freshly cut surface of one of the bearings showed however that Si is – as expected – not part of the graphite material itself.
One of the Viton O-rings sealing the ATC stator volume from the part in contact with the pumped gas was found to be damaged, probably due to improper handling during its installation. This is problematic since the stator coil assembly contains various insulating materials, with unknown outgassing and ageing properties, and furthermore gets rather hot during operation. With regard to cleanliness, traces of oil were found around several tap holes, which again shows that quality control has to be improved during the assembly.

On-chamber gas system tubelets: While the brass tubelets supplying the individual MDTs with gas could be excluded as a component causing ageing since they were identical for the two BIS multilayers, the question why the observed pulse height loss is larger in tube layers 1 and 2 than in layer 3 and 4 remains unanswered. Tubelets of the 4 different types were therefore removed from the BIS chamber after the end of the irradiation and opened. The visual inspection showed the presence of a dark patina, probably due to oxidation effects, mainly for the two short types. For the same types, some inner tubelet surfaces were found covered with an oil film (fig. 6.12). EDX analysis identified the oil as a hydrocarbon compound; sulfur was also present in the EDX spectrum, while no silicon could be detected. One can speculate that the differences in cleanliness for the various tubelet types and the different gain reductions observed in the individual BIS tube layers are correlated. This could e.g. be the case if a certain amount of a silicone contaminant transported by the gas is adsorbed by a clean brass surface, but not by a surface already oxidized or saturated with oil. The fact that no silicon was found in the EDX analysis for any of the tubelets does not rule out this possibility, if the thickness of the adsorbed material is below the minimum of 0.2 μm needed for a detection by EDX.

[4]The antimony is part of the bearing material Electrografit GU 118, as explained in 3.9.1.

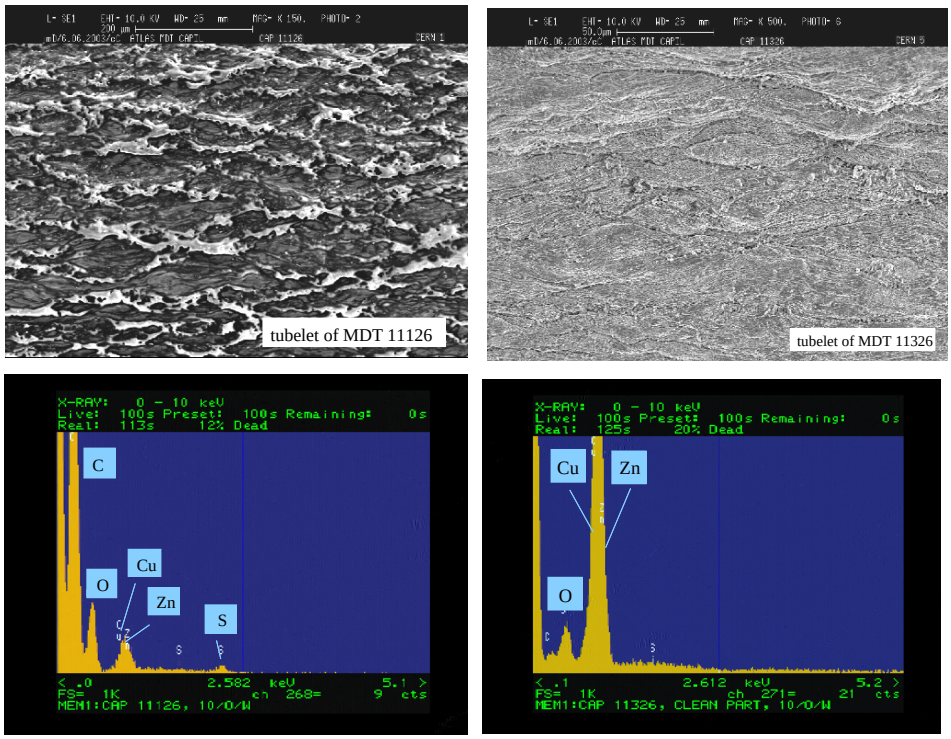

Figure 6.12: Micrographs and EDX results for two brass tubelets of the on-chamber gas system. Tubelet 11126 (left column) showed a clear oil film on the inner surface; the oil was identified as a hydrocarbon compound containing an admixture of sulphur, but no silicon. Tubelet 11326 (right column) appeared clean under visual and electron-microscopic examination. The EDX spectrum in this case shows peaks for copper (Cu), zinc (Zn) and oxygen (O) only, as expected for a brass alloy.

Conclusions from the chemical analysis

The chemical and surface analysis results for MDTs connected to the gas recirculation system confirmed a silicone contaminant as the cause of the observed ageing effects. The three valves identified as the source of the pollutant show that the absence of ageing in a low background environment (LEP) is no guarantee for a component's suitability for use at the LHC. The fact that only a silicon oxide, but no carbon was detected on the anode wire is evidence that contaminant molecules are not purely attracted to the anode by their dipole moment and condense there; a more complicated reaction must take place, causing the molecules to break up. This process almost certainly depends on the rather violent conditions in the gas amplification process and thus on the presence of a certain level of ionizing radiation.

The study proved that cleaning procedures, especially in the hand of commercial manufacturers, are not yet well controlled. The discovery of grease on a number of O-rings in the gas system showed that drawing up a set of technical specifications alone is not sufficient; more work is needed in implementing an efficient quality assurance scheme before the assembly of the final Atlas system can start.

Chapter 7

Summary

The muon spectrometer of the Atlas experiment, which is currently under construction at the European Laboratory for Particle Physics CERN, relies on Monitored Drift Tubes (MDTs) for precision track reconstruction in most of its regions. The purpose of this thesis was to study the MDT high rate and ageing behaviour in a radiation environment similar to the one expected at the LHC, where individual tube count rates reach up to $500\,\mathrm{Hz/cm^2}$ and a charge of up to $0.6\,\mathrm{C/cm}$ will be accumulated in 10 years of operation. Measurements were carried out at CERN's Gamma Irradiation Facility GIF, using for the first time a full series production chamber and an almost final version of the Atlas front end electronics. The drift tubes were irradiated over their full length with the help of a $740\,\mathrm{GBq}$ $^{137}\mathrm{Cs}$ source. During the longterm ageing study, lasting in total approximately 9 months, the chamber performance was monitored with cosmic muons in weekly reference runs. Data was also taken with muons produced by CERN's SPS accelerator complex; the muon energy in this case was $100\,\mathrm{GeV}$.

The analysis of the test beam data, acquired with the GIF radioactive source switched on, showed a change in the maximum drift time t_{max} and a resolution degradation at large drift radii r. Both are caused by the presence of space charge. Simulations were carried out with the program GARFIELD in order to better understand the observed behaviour; it was found that a simple steady state model is sufficient to correctly reproduce the changes in t_{max} while space charge and consequently electric drift field fluctuations have to be taken into account to explain the loss in resolution.

The probability of an MDT to detect a passing muon at all (hit efficiency) and to record it with a proper drift radius (3σ-efficiency) were also investigated; the hit efficiency was virtually unaffected by the background rate while the 3σ-efficiency showed a decrease due to background hits masking the true muon signal. No evidence for any hits being lost by the electronics or in the readout chain was found up to rates of $1500\,\mathrm{Hz/cm}$, which is an important validation of the electronics components.

A major goal of the longterm study was the implementation and first test of a gas recirculation system, which is needed in Atlas due to the large detector volume. The same high speed turbine (Argon Turbo Circulator ATC) as chosen for the final experiment was used; the recirculation flow was 1 to 2 volume exchanges per day, with 10% of the gas being replaced by fresh gas in each cycle. The ATC was found to operate stably; care is however needed in its grounding and shielding configuration in order to prevent the pump from causing a large amount of electromagnetic interference. Only half of the 240 MDTs of the muon chamber utilized in the ageing measurements were connected to the gas recirculation system. The remaining tubes were operated in a classical flushing mode with the gas passing them only once. The operating mixture in both cases was Ar:CO_2=93:7,

as foreseen at Atlas.
No loss in gas gain was observed for tubes operated without gas recirculation, up to an accumulated charge equivalent to approximately 4 years of LHC operation. This reconfirmed Ar:CO_2=93:7 as an intrinsically ageing-free gas mixture well suited for use in high background environments as the one found at LHC. The materials and components making up an MDT (endplugs, O-rings, aluminium tube) were also revalidated.
For tubes connected to gas recirculation on the other hand a massive loss in pulse height close to the gas inlet side of the MDTs was observed, starting from as little as 20 mC/cm accumulated charge. Scanning electron microscopy revealed needle-like deposits on the anode wire surface as being responsible for this effect. The needles were identified by energy dispersive X-ray analysis as a form of silicon oxide. Since silicon is a chemical element not part of any of the operating gas components, this immediately lead to the conclusion that the observed ageing must be due to a contaminant in the system. Several valves containing a silicone rubber as sealant were finally identified by IR-spectroscopy as the origin of the pollutant. The valves had been recuperated from the Aleph TPC setup, where they did not cause any problems during many years of LEP operation; the absence of ageing in a low background environment is therefore no guarantee for a component's suitability for use at the LHC.
The visual and spectroscopic examination of the various components in the gas recirculation system also gave evidence for improper cleaning and assembly procedures. Traces of a hydrocarbon grease were found in several locations. More work is therefore clearly needed in establishing an effective quality assurance scheme before starting the construction of the final Atlas system.

Appendix A

MDT response and transfer functions

A.1 Abstract description of electrical systems

When designing electrical systems one is often only interested in the functionality of certain building blocks, but not in their actual implementation. In this case an electric circuit can be treated as a 'black box' to which a signal A is input from one side; a second signal A' is obtained as output. All that is needed is a rule to calculate A' for a given input A.

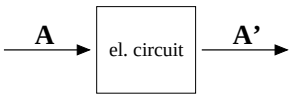

We will limit ourselves to linear components, i.e. circuits for which $A \longrightarrow A'$, $B \longrightarrow B'$ implies $(A+B) \longrightarrow (A'+B')$. In this case it is sufficient to know the output $g_\delta(t)$ ('response function') associated with an input signal which has the shape of a Dirac δ-function, $\delta(t)$. An arbitrary signal $A(t)$ will then result in an output which is the convolution of A and g_δ [56]:

$$A(t) \longrightarrow A'(t) = \int_0^t A(t') \cdot g_\delta(t-t')dt' \tag{A.1}$$

Often it is advantageous to use the Laplace transform

$$\tilde{A}(p) = \mathcal{L}(A(t)) = \int_0^\infty A(t) \cdot e^{-pt}dt \tag{A.2}$$

of a signal $A(t)$ rather than A itself. In the Laplace domain equation (A.1) becomes

$$\tilde{A}(p) \longrightarrow \tilde{A}'(p) = T(p) \cdot \tilde{A}(p) \tag{A.3}$$

where $T(p)$ is known as the system transfer function. $T(p)$ and $g_\delta(t)$ are connected by the important relation

$$g_\delta(t) = \mathcal{L}^{-1}(T(p))\,. \tag{A.4}$$

The main advantage of the Laplace domain approach is that the transfer functions of consecutive circuits multiply, i.e. $\tilde{A} \xrightarrow{T_1} \tilde{A}' \xrightarrow{T_2} \tilde{A}''$ is equivalent to $\tilde{A} \xrightarrow{T_1 \cdot T_2} \tilde{A}''$.

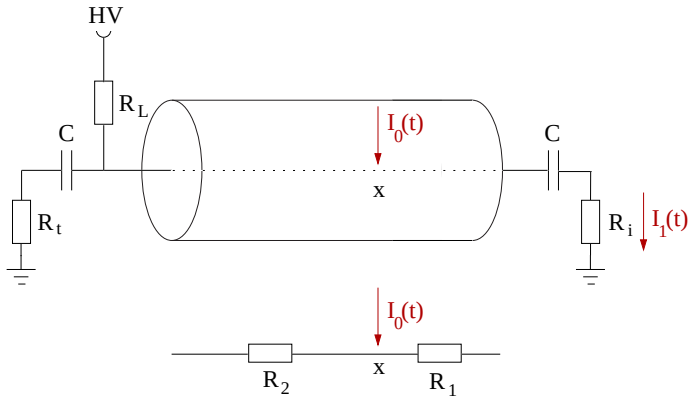

Figure A.1: Electric circuit diagram of an MDT: $R_t = 380\,\Omega$, $R_l = 1\,M\Omega$, C=470 pF, $R_i = 10 + 120\,\Omega$, $R_1 = 44\,\Omega/m \cdot x$, $R_2 = 44\,\Omega/m \cdot (l - x)$, l = tube length

A.2 Transfer function for a drift tube

Figure A.1 shows the equivalent electric circuit for a drift tube[1]. It is assumed that the tube is terminated at its HV side with a resistor R_t equal to the characteristic wave impedance to suppress signal reflexions. High voltage is supplied to the anode wire via the current limiting resistor R_l. R_i is the input impedance of the front end electronics, i.e. the pre-amplifier.
The transfer function for the shown circuit diagram was derived in [62] as

$$T_{mdt}(p) = \frac{\tilde{I}_1(p)}{\tilde{I}_0(p)} = \frac{p \cdot (b + a\,p)}{e + d\,p + c\,p^2} \quad \text{with} \tag{A.5}$$

$$\begin{aligned} a &= R_l \cdot (R_2 + R_t) + R_2 \cdot R_t & d &= 1/C \cdot (2R_l + R_t + R_1 + R_i + R_2) \\ b &= 1/C \cdot (R_2 + R_t) & e &= 1/C^2 \\ c &= R_l \cdot (R_l + R_i + R_2 + R_t) + R_1 \cdot R_t + R_i \cdot R_r + R_2 \cdot R_t\,. \end{aligned}$$

The corresponding response function g_δ has the form

$$g_\delta(t) = c_1 \cdot e^{-\alpha t} + c_2 \cdot e^{-\beta t} + k_2 \cdot \delta(t) \tag{A.6}$$

with parameters

$$k_1 = \frac{b}{c} - \frac{d\,a}{c^2},\; k_2 = \frac{a}{c},\; k_3 = \frac{e\,a}{c^2},\; \alpha = \frac{d}{2c} - \sqrt{\frac{d^2}{4c^2} - \frac{e}{c}},$$

$$\beta = \frac{d}{2c} + \sqrt{\frac{d^2}{4c^2} - \frac{e}{c}},\; c_1 = \frac{k_1\,\alpha + k_3}{\alpha - \beta},\; c_2 = -\frac{k_1\,\alpha + k_3}{\alpha - \beta}.$$

Equations (A.5) and (A.6) are the basis for understanding the relation between measured pulse heights and the muon hit position x in wire direction and thus for the results presented in section 6.4.

[1] assuming a purely ohmic resistance for signal propagation along the wire, which is not totally correct. For a strict analysis the tube-wire combination has to be treated as a coaxial transmission line with a frequency dependent impedance. This has been done in [38]; the results there show that the simple model shown above is adequate.

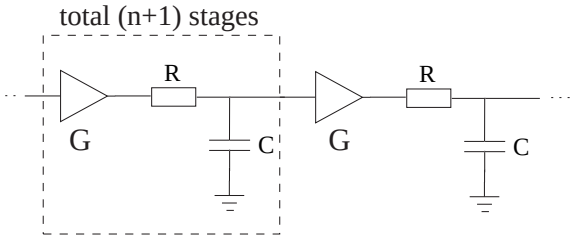

Figure A.2: Ideal amplifier with (n+1) integration stages

A.3 Front end electronics: Amplification and pulse shaping

The analogue part of the active MDT front end electronics (ASD) comprises a pseudo-differential pre-amplifier, several differential gain stages, circuits for pulse shaping and finally a discriminator with programmable threshold, as described in section 3.6.2. The prototype ASD-lite used for the studies presented in this thesis differs from the final version in the implemented shaping scheme. Pulses at the discriminator input are unipolar (with a large undershoot) for the ASD-lite and bipolar for the final ASD[2].
The simplest circuit with unipolar characteristic is shown in figure A.2. For a total number of (n+1) integration stages one finds the transfer function

$$T(p) = \left(\frac{1}{\tau p + 1}\right)^{n+1} \cdot G^{n+1} \quad \tau = R \cdot C \tag{A.7}$$

and the response function

$$g_\delta(t) = \frac{G^{n+1}}{n!\,\tau} \cdot \left(\frac{t}{\tau}\right)^n \cdot e^{-t/\tau}\,, \tag{A.8}$$

which is shown in figure A.3. The peaking time for a δ-like input is $t_p = n \cdot \tau$.

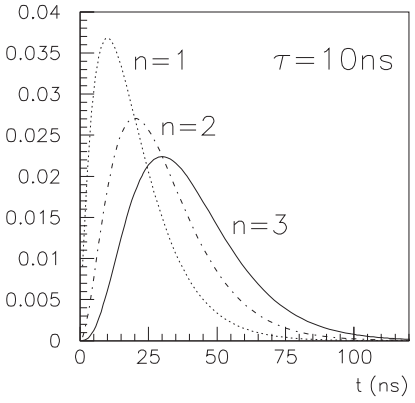

Figure A.3:
Response function for an ideal amplifier with (n+1) integration stages for different n.

[2]Please refer to [63] for a discussion of the different shaping schemes and their respective advantages.

A.4 Front end electronics: Tail cancellation

In section 2.2.5 it was shown that the current signal induced in the anode wire of a drift tube by a single ion cluster has the form

$$I(t) = -\frac{q}{2 \cdot \ln(b/a)} \cdot \frac{1}{t + t_0}\,. \tag{2.17}$$

(2.17) is characterized by a long tail towards large t, which is unwanted in high rate conditions since it leads to pile-up and an effective shift of the signal baseline. A pole-zero filter as shown in figure A.4 can be used for tail cancellation. The transfer and response functions for such a circuit are

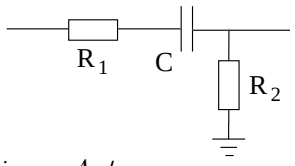

Figure A.4: Pole-zero filter network

$$T(p) = \frac{p + \frac{1}{\tau_1}}{p + \frac{1}{\tau_2}} \quad \text{and} \tag{A.9}$$

$$g_\delta(t) = (\frac{1}{\tau_1} - \frac{1}{\tau_2}) \cdot e^{-t/\tau_2} + \delta(t) \tag{A.10}$$

with $\tau_1 = R_1 \cdot C$ and $\tau_2 = \frac{R_1 \cdot R_2 \cdot C}{R_1 + R_2}$. A Pole-zero filter transforms an exponential e^{-t/τ_1} into e^{-t/τ_2} with $\tau_2 < \tau_1$. Drift tube signals following (2.17) can be approximated by a sum of exponentials; several pole-zero networks are then used to obtain optimal tail cancellation.

A.5 Response function for the MDT ASD-lite

The voltage response for the amplifier-shaper combination of the MDT prototype electronics was simulated with the program PSPICE[3]; it is shown in figure A.5. The numerically obtained function can be parametrized as

$$g_\delta(t) = p_1 \cdot \left(\frac{t}{\tau}\right)^3 \cdot e^{-t/\tau} + e^{\,(p_2 - p_3 \cdot t)} + e^{\,(p_4 - p_5 \cdot t)} \quad \text{with} \tag{A.11}$$

[3]PSPICE simulation courtesy of C. Posch, Boston University

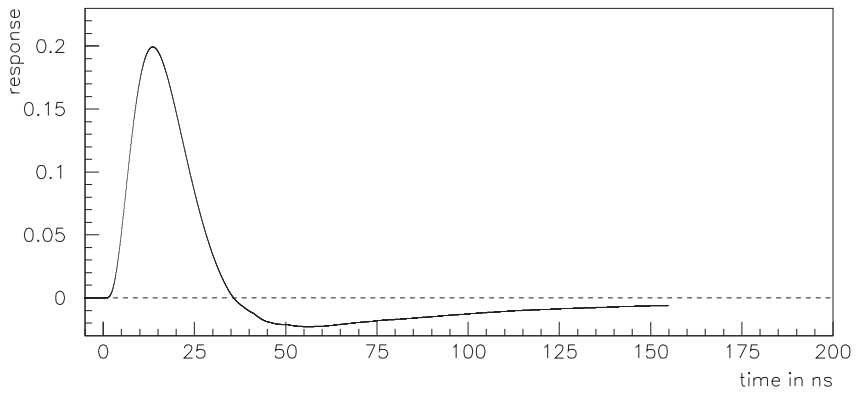

Figure A.5: ASD-lite voltage response to a δ-like current input pulse (PSPICE simulation).

$$\begin{array}{lllllllll} p_1 & = & 0.1685 & & p_2 & = & -2.9135 & & p_4 & = & -2.8664 \\ \tau & = & 4.55\,\text{ns} & & p_3 & = & 12.67\,\text{ns} & & p_5 & = & 70.18\,\text{ns}\,. \end{array}$$

(A.11) was found by assuming the ASD as an ideal amplifier in combination with a 2-stage tail cancellation filter. The parameters $p_1 \ldots p_5$ and τ were then obtained by a least square fit to the simulation result.

Appendix B

Hodoscope calibration and track reconstruction

While the primary purpose of the scintillator hodoscope during cosmics data taking was to provide a hardware trigger signal – which was used both as start signal for the drift time measurement and to generate the ADC gate – the hodoscope was also utilized to obtain the angle of a muon track with respect to the wire direction of the BIS chamber and to reconstruct the track position along the MDT tube axis. These quantities were needed in the pulse height analysis presented in chapter 6; the methods applied to arrive at them are therefore summarized in this section.

B.1 Track reconstruction in each hodoscope double layer

A muon trajectory in the hodoscope is fully defined by the two points in which the track intersects with the scintillator double layers. These points can be specified as (x_i, z_i), $i = 1, 2$ in local hodoscope coordinates (section 3.8). In the following it is assumed that a 'good' muon track has exactly one hit in each of the 4 scintillator planes, with hits in each of the double layers belonging to overlapping scintillators.

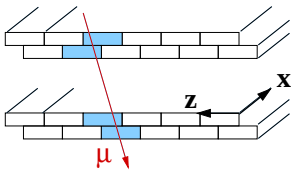

For each of the double layers, z_i is directly available from checking which scintillators were hit. The position resolution in z-direction is $\pm 5\,\mathrm{cm}$. The track coordinate in x-direction, x_i, can be calculated from the TDC time measurements Δt_1 and Δt_2 of the overlapping pair of scintillators. Since these are read out to opposite sides (fig. 3.4), one finds

$$\delta t := \Delta t_1 - \Delta t_2 = (a_1 - a_2) + (2x - l)/c' =: a_{12} + b_{12} \cdot x\,. \tag{B.1}$$

c' is the speed of light in the scintillator material, $l = 105\,\mathrm{cm}$ is the length in which the pair of scintillators overlaps; a_1, a_2 are constants taking into account the photo multiplier conversion time, cable delays, etc.
In order to solve (B.1) for the coordinate x, the calibration constants a_{12}, b_{12}, of which there are in total 44 for the full hodoscope, must be known. They can be obtained in the following way: If only one of the hodoscope double layers is used to generate the trigger signal instead of the standard coincidence of all 4 scintillator layers[1], histogramming δt for overlapping scintillators in this layer gives a rectangular distribution with center c_0 and width w (fig. B.1); the edges of the distribution are smeared due to the limited timing

[1] Otherwise geometrical acceptance effects must be taken into account.

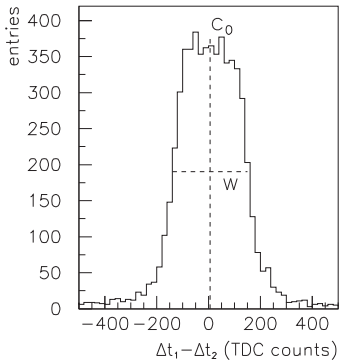

Figure B.1:
Hodoscope double layer calibration. Histogramming the TDC time difference $\Delta t_1 - \Delta t_2$ for a pair of overlapping scintillators read out to opposite sides gives a rectangular distribution. The center c_0 and width w of the distribution can be used to calculate the calibration constants needed for track reconstruction.

resolution. The parameters c_0 and w, which are obtained by fitting two Fermi functions to the rising and falling edge of the histogram, are then related to a_{12} and b_{12} by

$$w = \delta t(x = l) - \delta t(x = 0) = b_{12} \cdot l \quad \text{and} \quad c_0 = \delta t(x = l/2) = a_{12} + b_{12} \cdot l/2\,. \tag{B.2}$$

B.2 Reconstruction of the track angle φ

Once the muon track position (x_i,z_i) in each of the two hodoscope double layers has been calculated according to the procedure described above for a given event, it is straight forward to obtain the track angle φ with respect to the MDT wire direction. For this the local coordinates $(x_i, 0, z_i)$, $i = 1, 2$ are transformed into global coordinates $(\tilde{x}_i, \tilde{y}_i, \tilde{z}_i)$, $i = 1, 2$; φ is then given by

$$\cos\varphi = \frac{\vec{x}_{track} \cdot \vec{x}_{wire}}{|\vec{x}_{track}| \cdot |\vec{x}_{wire}|} \tag{B.3}$$

with $\vec{x}_{track} := \vec{\tilde{x}}_2 - \vec{\tilde{x}}_1$ and $\vec{x}_{wire}$ pointing in direction of the MDT tube axis.
Figure B.2 shows the angular distribution of muon tracks for ageing periods 'Age1' and 'Age2'. The distribution is wider for the second period due to the smaller distance between the hodoscope double layers in comparison to the setup during the phase 'Age1'.

B.3 Reconstruction of the track position in MDT wire direction

From the hodoscope data it is possible to reconstruct the position of a muon track in MDT wire direction and its distance from the BIS chamber readout side. For this the

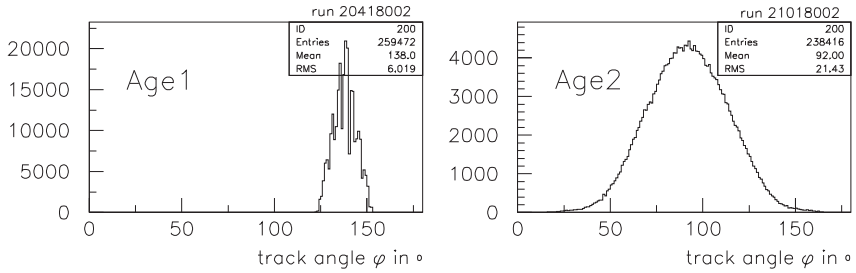

Figure B.2: Track angle distribution with respect to the MDT wire direction, as reconstructed from the hodoscope data. Left: Ageing period 'Age1', right: Ageing period 'Age2'.

muon trajectory is expressed as (coordinates in the following refer to the global coordinate system)

$$g: \quad \vec{x} = \vec{x}_1 + t \cdot (\vec{x}_2 - \vec{x}_1), \; t \epsilon \mathrm{R}; \tag{B.4}$$

each BIS multilayer is geometrically treated as a plane with the representation

$$P: \quad (\vec{x} - \vec{x}_0) \cdot \vec{n} = 0 \tag{B.5}$$

where $\vec{x}_0$ is an arbitrary point in the plane, usually chosen as the origin of the local BIS coordinate system, and $\vec{n}$ is a unit vector perpendicular to the plane.
The intersect $g \cap P$ of the muon track with the plane (BIS chamber) is then calculated according to

$$\vec{x}_{g \cap P} = \vec{x}_1 + \frac{(\vec{x}_0 - \vec{x}_1) \cdot \vec{n}}{(\vec{x}_2 - \vec{x}_1) \cdot \vec{n}} \cdot (\vec{x}_2 - \vec{x}_1)\,. \tag{B.6}$$

Transforming $\vec{x}_{g \cap P}$ into local BIS multilayer coordinates and taking the x-component immediately yields the distance of the track from the readout side of the chamber.
Figure B.3 shows hit distributions for the two ageing periods 'Age1' and 'Age2'; one can clearly see that in both cases not the full chamber was covered by the hodoscope trigger acceptance.

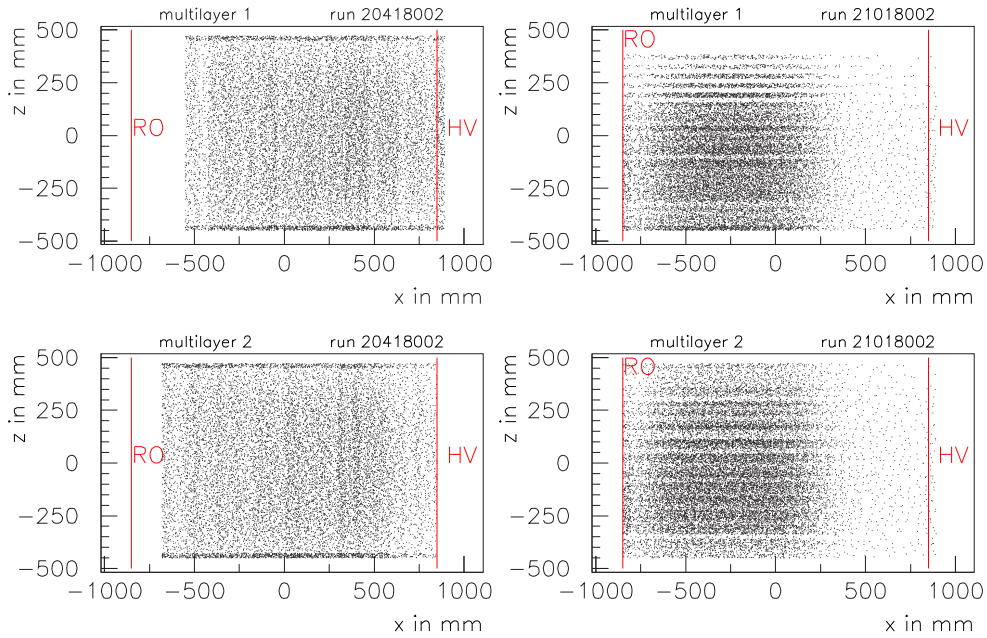

Figure B.3: Muon track distribution in the BIS chamber. Left: Ageing period 'Age1', right: Ageing period 'Age2'. x-coordinates are in wire direction, z-coordinates perpendicular to the tube axis. The red lines denote the geometrical dimensions of the BIS chamber; one can clearly see that in period 'Age1' the first ≈30 cm measured from the chamber readout side were outside of the trigger acceptance, while during phase 'Age2' only the range -85 cm≤ x ≤+20 cm was covered by the hodoscope.

Appendix C

Gas system components

The tables below list the components in the off-chamber gas system. Numbers correspond to figure 3.17. Care was taken to select components which are by design lubricant-free; all valves newly purchased for the recirculation prototype were either membrane or metal bellows valves. The three ball valves (14,15,36) recuperated from Aleph are believed to be responsible for the observed chamber ageing described in chapter 6.

No	Function	Manufacturer	Type
1	Mass flow controller	Bronkhorst HI-TEC, Ruurlo, NL	F-201C-RA-33-E
2	Rotameter	Voegtlin Instruments, Aesch, CH	V100-140.14 for O_2 use
3	Pressure controller	Bronkhorst HI-TEC, Ruurlo, NL	P-702C-RA-33V
4	Mass flow controller	Bronkhorst HI-TEC, Ruurlo, NL	F201C-FA-22V
5	Mass flow controller	Bronkhorst HI-TEC, Ruurlo, NL	F201C-FA-22V
6	Mass flow controller, low Δp	Bronkhorst HI-TEC, Ruurlo, NL	F201C-FAC-22V
7	Flow meter	Systec Controls, Puchheim, D	Deltaflow Staudrucksonde DF10MG-F-DW-ME-PN16
8	Pressure gauge	WIKA, Klingenberg, D	614.11
9	Pressure gauge	WIKA, Klingenberg, D	614.11
10	Pressure controller	MKS Instruments, Andover, US	Baratron 690A with valve 0248A-02000RV
11	Pressure controller	MKS Instruments, Andover, US	Baratron 690A with valve 0248A-02000RV
12	Pressure transducer	Bourdon-Haenni, Jegenstorf, CH	ED 510/414
13	Pressure transducer	Bourdon-Haenni, Jegenstorf, CH	ED 510/414
14	Ball valve (manual)	Recuperated from Aleph TPC	—
15	Ball valve (manual)	Recuperated from Aleph TPC	—
17	Pneumatic shutoff valve	Parker Instrumentation, Huntsville, US	M6A-P4K-SSV-PP
18	Manual shutoff valve	Parker Instrumentation, Huntsville, US	Nova B 441T Veriflo, brass
19	Manual shutoff valve	Legris, Rennes, F	Quarter-turn valve
20	Manual shutoff valve	Hoke Spartanburg, US	Needle valve
21	Manual shutoff valve	Hoke, Spartanburg, US	Needle valve

No	Function	Manufacturer	Type
22	Manual shutoff valve	Parker Instrumentation, Huntsville, US	Nova B 441T Veriflo, brass
23	Safety relief valve	Circle Seals, Corona, US	51598-4MP-140
24	Manual shutoff valve	Parker Instrumentation, Huntsville, US	Nova B 441T Veriflo, brass
25	Manual shutoff valve	Parker Instrumentation, Huntsville, US	Nova B 441T Veriflo, brass
26	Manual shutoff valve	Parker Instrumentation, Huntsville, US	Nova B 441T Veriflo, brass
27	Manual shutoff valve	Parker Instrumentation, Huntsville, US	Nova B 441T Veriflo, brass
28	Manual shutoff valve	Parker Instrumentation, Huntsville, US	Nova B 441T Veriflo, brass
29	Pressure reducer	Carbagas, Gümligen, CH	—
30	Mass flow meter	Bronkhorst HI-TEC, Ruurlo, NL	F-201C-FA-22
31	Manual shutoff valve	Parker Instrumentation, Huntsville, US	Nova B 441T Veriflo, brass
32	Manual shutoff valve	Parker Instrumentation, Huntsville, US	Nova B 441T Veriflo, brass
33	Manual shutoff valve	Parker Instrumentation, Huntsville, US	Nova B 441T Veriflo, brass
34	Safety relief valve	Circle Seals, Corona, US	51598-4MP-140
35	Safety relief valve	Circle Seals, Corona, US	51598-4MP-140
36	Ball valve (manual)	Recuperated from Aleph TPC	—
37	Mass flow meter	Brooks Instruments, Hatfield, US	5813/A1A1A3D04
38	Manual shutoff valve	Hoke, Spartanburg, US	Needle valve
40	Manual shutoff valve	Parker Instrumentation, Huntsville, US	M6A-P4K-SSV-PP
42	Pneumatic shutoff valve	Parker Instrumentation, Huntsville, US	Nova AOP-1-B-44TT-MH US
43	Safety relief valve	Circle Seals, Corona, US	51598-4MP-140
44	Pressure reducer	Air liquide	—
F	Particle filter	Ultrafilter, Zurich, CH	220000 V-SM 15/30 VE 5 μm Ultramesh (stainless steel)

Appendix D

DAQ data format

D.1 Event block structure

All data acquired from the MDTs, hodoscope and pulse height ADCs is stored in binary format as 32-bit words. A number of events is accumulated into an **Event Block** (with a maximum size of 1024 words) before being released to disk. Each event block is preceded by a 11 word block header.

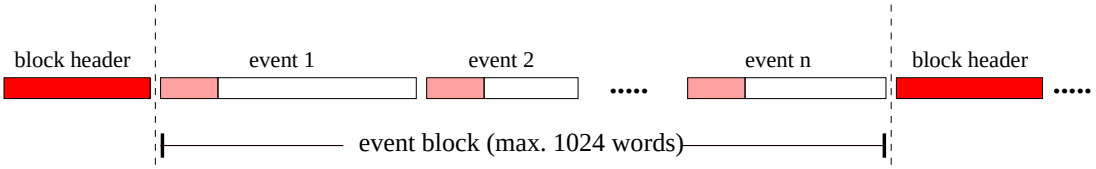

The block header contains the following information:

word 0: total number of words in block, including itself,
word 1: run number,
word 2: block number, incremented with each new block,
word 3: reserved 1,
word 4: reserved 2,
word 5: number of events contained in this block,
word 6: number of words in block, excluding block header,
word 7: timestamp, see below,
word 8: not used,
word 9: not used,
word 10: total number of words to follow, including itself.

A timestamp is used to correlate DAQ data with environmental parameters recorded by the slowcontrol. The format of word 7 is

Bit:

31				27				23				19				15				11				7				3			0

0	S	year	month	day	hour	min	sec

Example: 22/9/2001 15:01:01, DST

0	1	0	0	0	1	1	0	0	1	1	0	1	1	0	0	1	1	1	1	0	0	0	0	0	1	0	0	0	0	0	1

S denotes if daylight saving time was active (1) or not (0). The year is specified relative to the year 2000.

D.2 Event data

The first word in each event is an **Event Header**, which contains the word count of the event to follow (excluding itself), the event ID and a flag if an integrity error was detected during readout of the event or if the event was forced after a DAQ hang up was detected. The event header is followed by data read out from the MDTs (via the CSM-0), the hodoscope and the ADCs.

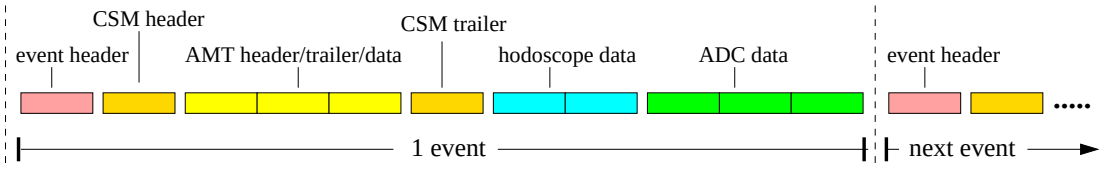

Event header format:

Bit:

31				27				23				19				15				11				7				3			0

Event header for 'good' events

0	0	0	0	0	0	0	0	EVID	WC

Example EVID 0x223, WC 0x04a

0	0	0	0	0	0	0	0	0	0	1	0	0	0	1	0	0	0	1	1	0	0	0	0	0	1	0	0	1	0	1	0

Event header for forced events

0	0	0	1	0	0	*	1	EVID	WC

Event header if a hodoscope integrity error occurred

0	0	0	1	0	0	1	*	EVID	WC

Event header if an ADC integrity error occurred

0	0	0	1	0	1	*	*	EVID	WC

CSM-0 data format:

MDT data is written to file by the DAQ exactly as it is received from the CSM-0 [37]. Tubes are identified by the mezzanine card (AMT) they are connected to and the AMT channel.

Bit:

31				27				23				19				15				11				7				3			0

CSM header

0	1	0	1	1	0	0	1	EVID	BCID

CSM trailer

0	1	0	1	1	0	1	1	EVID	WC

CSM trailer for events flagged as abnormal by the CSM-0

0	1	0	1	1	1	0	1	EVID	WC

CSM error word

0	1	0	1	0	0	0	0	0	0	0	0	0	0	flags for abn. TDC

Bit:

31				27				23				19				15				11				7				3			0

AMT header

1	0	1	0	AMT Id	EVID	BCID

AMT trailer

1	1	0	0	AMT Id	EVID	word count for this AMT

AMT leading edge data. E: error flag if data was missed due to an AMT buffer overflow

0	0	1	1	AMT No	AMT channel	0	E	coarse time	fine time

Example: TDC 2, channel 12, coarse time 35, fine time 16 (i.e. $t_{drift} = 35 \cdot 25\,\text{ns} + 16 \cdot 0.78\,\text{ns}$)

0	0	1	1	0	0	1	0	0	1	1	0	0	0	0	0	0	0	0	0	0	0	1	1	0	0	1	1	0	0	0	0

AMT mask word

0	0	1	0	AMT Id	mask flags for individual AMT channels, true if at least one hit was found in the mask window

The AMT Id is a number assigned to each AMT during JTAG programming; the AMT No in the leading edge data is the CSM-0 channel the AMT (more precisely: its mezzanine card) is connected to.

Hodoscope data format:

Data from any of the 24 11-bit LeCroy 2228 TDCs is written to disk only if the TDC is not in overflow.

bit:

31				27				23				19				15				11				7				3			0

Hodoscope TDC data

1	1	1	1	0	0	1	1	module	TDC channel	0	0	0	0	0	TDC data

Example: module=2, TDC Ch. 4, data 0x112

1	1	1	1	0	0	1	1	0	0	1	0	0	1	0	0	0	0	0	0	0	0	0	1	0	0	0	1	0	0	1	0

Hodoscope error word if TDC conversion did not finish

1	1	1	1	0	0	1	1	module	TDC channel	1	1	1	1	0	0	0	0	0	0	0	0	0	0	0	0

ADC data format:

bit:

31				27				23				19				15				11				7				3			0

ADC data

1	1	1	1	0	1	0	0	module	ADC channel	0	0	0	0	0	ADC data

Example: module=2, ADC Ch. 4, data 0x112

1	1	1	1	0	1	0	0	0	0	1	0	0	1	0	0	0	0	0	0	0	0	0	1	0	0	0	1	0	0	1	0

ADC error word if conversion did not finish

1	1	1	1	0	1	0	0	module	ADC channel	1	1	1	1	1	1	1	1	1	1	1	1	1	1	1	1

List of Figures

References

[1] S. Agosteo et al.: *A facility for the test of large area muon chambers at high rates*, Nucl. Instr. and Meth. A 452 (2000) 94-104

[2] S. Ahlen et al.: *Measurement of Atlas MDT Neutron Sensitivity and Development of a Simulation Model*, Atlas Internal Note ATL-MUON-98-236, Geneva (1998)

[3] T. Akesson et al.: *Aging studies for the Atlas Transition Radiation Tracker (TRT)*, Nucl. Instr. and Meth. A 515 (2003) 166-179

[4] M. Aleksa et al.: *MDT Performance in a High Rate Background Environment*, Atlas Internal Note ATL-MUON-98-258, Geneva (1998)

[5] M. Aleksa: *Performance of the ATLAS Muon Spectrometer*, PhD-thesis, Technische Universität Wien (1999)

[6] G.D. Alkhazov: *Statistics of electron avalanches and ultimate resolution of proportional counters*, Nucl. Instr. and Meth. 89 (1970) 155-165

[7] Y. Arai: *Requirements and Specifications of the TDC for the ATLAS Precision Muon Tracker*, Atlas Internal Note ATL-MUON-97-179, Geneva (1997)

[8] Y. Arai: *AMT-1 User's Manual*, KEK, Japan (2000)

[9] Atlas Collaboration: *Technical Proposal for a General-Purpose pp Experiment at the Large Hadron Collider at CERN*, CERN/LHCC/94-43, Geneva (1994)

[10] Atlas Collaboration: *Atlas Calorimeter Performance Technical Design Report*, CERN-LHCC 96-40, Geneva (1996)

[11] Atlas Collaboration: *Atlas Inner Detector Technical Design Report*, CERN-LHCC 97-16 and 97-17, Geneva (1997)

[12] Atlas Collaboration: *Atlas Magnet System Technical Design Report*, CERN-LHCC 97-18, Geneva (1997)

[13] Atlas Collaboration: *Atlas Muon Spectrometer Technical Design Report*, CERN-LHCC 97-22, Geneva (1997)

[14] Atlas Collaboration: *Atlas First-Level Trigger Technical Design Report*, CERN-LHCC 98-14, Geneva (1998)

[15] Atlas Collaboration: *Atlas Detector and Physics Performance Technical Design Report*, CERN-LHCC 99-14 and 99-15, Geneva (1999)

[16] Atlas Muon Collaboration: *Assembled Drift Tube*, Internal Drawing ATLMMACA0031, Geneva (1999)

[17] Atlas Radiation Background Task Force: *Predicted radiation levels in Atlas*, GCALOR simulation results for the shielding geometry as of Jan. 2003, Geneva (2003)

[18] A. d'Auria et al.: *Engineering Layout for the ATLAS MUON Gas System Modules*, Atlas Internal Document ATC-TG-EP-002, Geneva (2002)

[19] G. Avolio et al.: *First results of the 2001 MDT chambers beam test*, Atlas Internal Note ATL-MUON-2003-001, Geneva (2001)

[20] Y. Baconnier et al.: *LHC: the Large Hadron Collider accelerator project*, CERN Internal report CERN-AC-93-03-LHC, Geneva (1993)

[21] P. Bagnaia et al.: *Calib: a package for MDT calibration studies - User Manual*, Atlas Internal Note, ATL-COM-MUON-2002-004, Geneva (2002)

[22] R. Ball, J. Chapman, J. Hollar, J. Kuah: *Atlas MiniDAQ Reference Guide*, University of Michigan, Ann Arbor (2000)

[23] S. Baranov, Y. Gornushkin, Z. Krumstein: *Study of the δ-electron influence on the muon track measurement in the HPDT option of the ATLAS muon system*, Atlas Internal Note ATL-MUON-93-019, Geneva (1993)

[24] S. Baranov, I.R. Boyko, G.A/ Chelkov, M.A. Ignatenko: *Gamma Sensitivity of Pressurised Drift Tubes*, Atlas Internal Note ATL-MUON-94-036, Geneva (1994)

[25] S.F. Biagi: *A Multiterm Boltzmann analysis of drift velocity, diffusion, gain and magnetic-field effects in argon-methane-water-vapour mixtures*, Nucl. Instr. and Meth. A 283 (1989) 716-722

[26] S.F. Biagi: *MAGBOLTZ: Transport of electrons in gas mixtures*, CERN Program Library, Geneva (2000)

[27] W. Blum, L. Rolandi: *Particle Detection with Drift Chambers*, Springer-Verlag, Berlin (1993)

[28] R. Börnstein, H.H. Landolt: *Landolt-Börnstein. Zahlenwerte und Funktionen aus Physik, Chemie, Astronomie, Geophysik und Technik*, 6. Aufl., Bd. 4, Teil 3, Springer-Verlag, Berlin (1957)

[29] S. Borzakov et al.: *Response of the MDT filled with Ar+5% CO_2+3% CH_4 to thermal neutrons*, Atlas Internal Note ATL-MUON-96-116, Geneva (1996)

[30] M. Capeans: *Recent Aging Studies for the ATLAS Transition Radiation Tracker* , presentation given at the Detector Ageing Workshop, IEEE Nuclear Science Symposium 2003, Portland

[31] M. Capeans: *Aging and materials: lessons learned for detectors and gas systems*, Nucl. Instr. and Meth. A 515 (2003) 73-88

[32] CERN: *AC division image server*, picture CERN_AC_HE110, Geneva (1995)

[33] CERN: *AC division image server*, picture CERN_AC_HF205_V2/2/1998, Geneva (1998)

[34] CERN: *AC division image server*, picture CERN_AC_HE107A_V02/02/98, Geneva (1998)

[35] C. Cernoch, S. Zimmermann: *First experience with the prototype Atlas MDT gas circulation system at GIF*, Atlas Internal Note ATL-COM-MUON-2002-023, Geneva (2002)

[36] C. Cernoch: *Performance of ATLAS Muon Precision Drift Chambers in a High Radiation Environment*, PhD-thesis, Technische Universität Wien (2003)

[37] J. Chapman, B. Ball, J. Kuah, J. Mann, J. Hollar: *CSM Design and CSM-0 Production*, University of Michigan document UMHE-99-01, Ann Arbor (2000)

[38] M. Deile, J. Dubbert, N.P. Hessey: *Charge Division and Intrinsic Pulse Shaping in Drift Tubes*, Atlas Internal Note ATL-MUON-96-105, Geneva (1996)

[39] M. Deile, N.p, Hessey: *Obtaining the Space-Time Relationship of Drift Tubes from the Drift-Time Spectrum*, Atlas Internal Note, ATL-MUON-99-002, Geneva (1999)

[40] W. Diethorn: *A methane proportional counter system for natural radiocarbon measurements*, USAEC Report NY06628 and doctoral dissertation, Carnegie (1956)

[41] M. Dold et al.: *Fast Gases for the ATLAS Monitored Drift Tubes*, Atlas Internal Note ATL-MUON-94-043, Geneva (1994)

[42] Geant Team: *GEANT - Detector Description and Simulation Tool*, CERN Program Library Writeup W5013, Geneva

[43] H. Genz: *Single electron detection in proportional gas counters*, Nucl. Instr. and Meth. 112 (1973) 83-90

[44] W. Haberichter, H. Spinka: *Wire chamber degradation at the Argonne ZGS*, Proceedings of the 'Workshop on Radiation Damage to Wire Chambers', LBL-21170, Berkely (1986)

[45] F. Hahn, S. Palestini: *The MDT Gas System, a Design Report*, Atlas Internal Document, Geneva June 2002

[46] M. Huk, P. Igo-Kemenes, A. Wagner: *Electron attachment to oxygen, water and methanol in various drift chamber gas mixtures*, Nucl. Instr. and Meth. A 267 (1988) 107-119

[47] J.A. Kadyk: *Wire chamber aging*, Nucl. Instr. and Meth. A 300 (1991) 436-479

[48] S. Kircher: *Parameter des Alterungsprozesses und der Reanimation von Driftröhren*, PhD-thesis, Albert-Ludwig Universität Freiburg (2001)

[49] M. Kollefrath et al.: *Ageing Studies for the ATLAS Monitored Drift Tubes*, Nucl. Instr. and Meth. A 419 (1998), 351-356

[50] M. Kollefrath: *Entwicklung, Aufbau und Durchführung von Alterungsuntersuchungen an Driftröhren für das ATLAS-Myon-Spektrometer*, PhD-thesis, Albert-Ludwig Universität Freiburg (1999)

[51] W.R. Leo: *Techniques for Nuclear and Particle Physics Experiments*, Springer-Verlag, New York (1994)

[52] L. Malter: *Thin Film Field Emission*, Phys. Rev. 50 (1936) 48-58

[53] J.E. Moyal: *Theory of ionization fluctuations*, Phil. Mag. 46 (1955) 263

[54] National Institute of Standards and Technology: *ESTAR: Stopping-Power and Range Tables for Electrons*, online database, http://physics.nist.gov/PhysRefData/Star/Text/ESTAR.html, (2003)

[55] P. Nevski et al.: *Evaluation of ionization produced by fast neutrons in Atlas muon detectors*, private report (2001)

[56] P.W. Nicholson: *Nuclear Electronics*, John Wiley & Sons, London (1974)

[57] R. Openshaw et al.: *Etching of anode wire deposits with CF_4/isobutane (80:20) avalanches*, Nucl. Instr. and Meth. A 307 (1991) 298-308

[58] Particle Data Group: *Review of Particle Physics*, Phys. Rev. D 66, 010001 (2002)

[59] V. Paschhoff: *Gasstudien für die Myonkammern des ATLAS Detektors*, diploma thesis, Albert-Ludwig Universität Freiburg (1994)

[60] V. Paschhoff: *Studies on Ageing and Reanimation of Drift Tubes for the Atlas Muon Spectrometer*, PhD-thesis, Albert-Ludwig Universität Freiburg (1999)

[61] C. Posch, E. Hazen, J. Oliver: *MDT-ASD, CMOS front-end for ATLAS MDT*, Atlas Internal Note ATL-MUON-2002-003, Geneva (2002)

[62] W. Riegler: *Limits to Drift Chamber Resolution*, PhD thesis, Technische Universität Wien (1997)

[63] W. Riegler, M. Aleksa: *Bipolar versus unipolar shaping of MDT signals*, Atlas Internal Note ATL-MUON 99-03, Geneva (1999)

[64] A. Romaniouk: *Choice of materials for the construction of the TRT*, Atlas Internal Note ATL-INDENT-98-211, Geneva (1998)

[65] D. Sampsonides: *Construction of the BIS MDT Chamber Module 0*, Atlas Internal Note ATL-COM-MUON-2001-006, Geneva (2001)

[66] G. Scherberger et al.: *High Rate Performance of Drift Tubes*, Atlas Internal Note ATL-MUON-98-262, Geneva (1998)

[67] I. Smirnov: *HEED: User Guide*, software reference manual version 1.01, CERN Program Library W5060, Geneva (1997)

[68] E. Solfaroli: *Lo spettrometro per muoni dell'esperimento ATLAS a LHC: studio delle caratteristiche e delle prestazioni con simulazione dettagliata dei rivelatori e analisi dei dati di test*, student thesis, Universita di Roma "La Sapienza", Rome (2002)

[69] M. Spegel: *On the lifetime of proportional counters*, PhD-thesis, Technische Universität Wien (1998)

[70] J. Va'vra: *Review of wire chamber aging*, Nucl. Instr. and Meth. A 252 (1986) 547-563

[71] R. Veenhof: *GARFIELD: User Guide*, software reference manual version 7.04, CERN Program Library W5050, Geneva (2001)

[72] H. Yasuda: *New insights into aging phenomena from plasma chemistry*, Nucl. Instr. and Meth. A 515 (2003) 15-30

[73] T. Zhao, L. He: *A Study of gas mixtures for ATLAS MDT*, Atlas Internal Note ATL-MUON-95-102, Geneva (1995)

Nach §6 Absatz 5 der Promotionsordnung der Universität Freiburg für die Fakultät für Mathematik und Physik aufzulistende bereits veröffentlichte oder zur Veröffentlichung eingereichte Arbeiten, die den Gegenstand der Dissertation berühren:

C. Adorisio, C. Cernoch, M. Cirilli, A. Di Girolamo, S. König, A. Kramer, S. Palestini, P. Valente, S. Zimmermann: *Recent and ongoing Ageing studies for the Atlas muon spectrometer drift tubes*, submitted to Nucl. Instr. and Meth. A, Proceedings of the 10th Vienna Conference on Instrumentation, Feb. 2004

Acknowledgements

The work presented in this thesis would not have been possible without the input and contribution from many colleagues; to all of them I express my sincere gratitude.
Special thanks go to my supervisor Gregor Herten for giving me the opportunity of doing a large part of my thesis at CERN and for his support; further to Claus Cernoch who suffered with me through many set-backs in building and running the test system at GIF. The CERN Atlas muon group welcomed me in their middle and had always an open ear for questions and problems; William Andreazza was indispensable in the mechanical design and assembly of all our setups – I am sure the continuously changing geometry drove him crazy more than once! Bernhard Pfeifer and Jürgen Tobias were a great help in getting the on-chamber gas system installed, and provided lots of other good advice. I am further indebted to my colleagues at the University of Athens, National Technical University of Athens and Aristotle University Thessaloniki for building the BIS chamber that got 'slaughtered' during our test, and to Vladimir Goriatchev for teaching me all about (Russian) scintillators.
The project could not have been done without the help of the CERN EP-TA1 gas experts, especially Ferdinand Hahn and Jean-Daniel Capt; definitely worth mentioning is also Ivan Lehraus from whose decade-long experience I benefitted a lot. Jean-Michel Dali, CERN-EST-SM, performed all the scanning electron microscopy and EDX analyses for us while Cedric Petitjean of the same group did most of the remaining chemical tests. A big 'thank you' to both of them. Thanks also to Jay Chapman, Jeff Gregory, Piedro Binchi and Greg Novak for the common effort in getting the MDT front end electronics to work – I will never forget the way we puzzled over the behaviour of the CSM-0 and the mezzanine cards during my visit to Ann Arbor in summer 2001!
The test beam would have been far less fun without Katharina Mair, Manuela Cirilli, Antonio di Domenico and Claudio Lucci, who all participated in shifts. With respect to software I am very grateful to the developers of the CALIB package, and in particular to Domicia Orestano and Mauro Iodice for their splendid introduction to the code during my stay at the Universita di Roma Tre in spring 2002.
Special thanks also go to Paolo Branchini for the tough fights on how to correctly calculate track fit extrapolation errors, and to Sandro Palestini, Ludovico Pontecorvo, Wolfgang Mohr and Ulrich Landgraf for the numerous discussions on the high rate analysis. To Ulrich I am furthermore indebted for helping me solve quite a few computer problems. Last, but not least, thanks to everybody I may have forgotten in the above list, and to my family and friends for putting up with those periods of time in which I was incredibly busy with my work and neglected them.